DEFORMATION AND MODULUS CHANGES OF NUCLEAR GRAPHITE DUE TO HYDROSTATIC PRESSURE LOADING

A THESIS SUBMITTED TO THE UNIVERSITY OF MANCHESTER FOR THE DEGREE OF DOCTOR OF PHILOSOPHY IN THE FACULTY OF ENGINEERING AND PHYSICAL SCIENCES

2012

Adetokunboh Temitope Bakenne

School of Mechanical, Aerospace and Civil Engineering

Abstract

Graphite is used within a reactor as a moderator and a reflector material. During fast neutron irradiation, the physical properties and dimensions of nuclear graphite are changed significantly. Graphite shrinkage could lead to disengagement of individual component and loss of core geometry; differential shrinkage in the graphite component could lead to the generation of internal stresses and component failure by cracking. The latter behaviour is complicated by the irradiation induced changes in Young's modulus and strength.

These dimensional and modulus change have been associated with the irradiation-induced closure of many thousands of micro-cracks associated with the graphite crystallites due to crystal dimensional change. Closure of microcracks in nuclear graphite was simulated by external pressure (hydrostatic loading, deviatory stress and dynamic loading) and not by irradiation, whilst Young's modulus was measured to check if there was any correlation between the two mechanisms.

A study of the deformation behaviour of polycrystalline graphite hydrostatically loaded up to 200MPa are reported. Gilsocarbon specimens (isotropic) and Pile Grade A (PGA) specimens are (anisotropic in nature) were investigated. Strain measurements were made in the axial and circumferential directions of cylindrical samples by using strain gauges. Dynamic Young's modulus was also investigated from the propagation velocity of an ultrasonic wave. Porosity measurements are made to determine the change in the porosity before and after deformation and also their contribution towards the compression and dilatation of graphite under pressure. Graphite crystal orientation during loading was also investigated by using XRD (X-ray diffraction) pole figures. Effective medium models were also investigated to describe the effect of porosity on graphite elastic modulus.

All the graphite specimens investigated exhibited non-linear pressure- volumetric strain behaviour in both direction (axial and circumferencial). In most of the experiments, the deformation was closing porosity despite new porosity being generated. Under hydrostatic loading, PGA graphite initially stiff then it became less stiff after a few percent of volume strain and then after about ~20% volumetric strain they stiffen up again, whist Gilsocarbon showed similar behaviour at lower volumetric strain (~10-13%). Gilsocarbon was stiff than PGA; this behaviour is due to the fact that Gilsocarbon has higher density and lower porosity than PGA. During unloading, a large hysteresis was formed. The stressed grains are relieved; the initial closed pores began to reopen. It is suggested that during this stage, the volume of pore re-

opening superseded the volume of pores closing, the graphite sample volume almost fully recovered.

In the axial compression test, PGA perpendicular to the extrusion direction (PGA-AG) was less stiff than PGA parallel to the extrusion direction (PGA-WG); in the hydrostatic compaction test, the PGA-WG sample deformed more because it had to undergo a less complicated shape change. This is because the symmetry of their anisotropy is parallel to the symmetry of the sample.

The Pole figures showed an evidence of slight crystal reorientation after hydrostatic loaded up to 200MPa. The effective medium model revealed the importance of porosity interaction in graphite during loading.

Acknowledgement

The research reported in this thesis could not have been completed without the help and support of many people. First, I wish to express my profound gratitude to my supervisors **Prof. Barry Marsden, Dr. Abbie Jones, Dr. Graham Hall, Dr. Julian Mecklenburgh and Prof. Paul Mummery** who were immensely helpful to me from the beginning to the end of my research in more ways than I can't possibly explain, God bless you guys. I would also like to thank my colleagues and friends from the University of Manchester Nuclear Graphite Research Group and Rock Deformation Laboratory for always been there and never make me feel lonely.

I will also like to thank EPSRC, KNOO and DTA for kindly funding my PhD, which enabled me to focus on my research instead of worrying about how to survive. I also wish to thank Oyindamola Esuruoso, Dr. Roland Ukor, Seun Awoga, Tope Akinloye, Michael Adenuga, Blessing Ugbi, Saran Toure, Titi Lucas, Dr. Ankur, Dr Oluwadamilola Awoye, Dr. Emanuel Adegbite, Dr. Bolaji Esuruoso, Dr. Eze Nwachukwu, Farouq Dosunmu, Oluwabankole Johnson, all the Agsoba's 98 and so many others friends for their love and care and friendship.

Thanks to my father and mother in the lord, **Pastor Abimbola** and **Folu Komolafe**, thanks a zillion for all the prayers, care and support, as well as for being very understanding during the times when the pressures of writing up meant that I was not as available as I should have been.

I also wish to appreciate to the technicians (Steve, Bill, Mark, Andy, Gary, Judith) for the research community exposure I received as a result of working with their individual workshop. I am extremely grateful to my family; to my parents who never abandoned me, but kept praying for me and supporting me in every way possible; and to my 5 siblings Abayomi, Omolara, Damola, Iyabo and Oyinkansola, who have been extremely wonderful to me even when I did not get in touch for extended periods of time. I also wish to thank Uncles and family friends Odunbaku's, and Olokode's. Thank you so much for your love, I am forever indebted to you all. Above all, I am grateful to God.

To my nephew and nieces (King-David, Favour and Victoria), I love you guys and I cannot wait to see you guys during my holiday.

A special thanks to my wife to be, for her consistent support and word of encouragement, even when I almost lost it

Adetokunboh Temitope Bakenne
December 2012.

Dedication

I dedicated this to my loving mother (**Marian Adunni Bakenne**) and my wonderful father (**Prince Adebayo Semiu Bakenne**). Above all to God, for without him I am nobody.

The author

Adetokunboh is a final year Nuclear Engineering PhD student at the University of Manchester. He is a tutor at the University of Manchester residential hall. He is currently undertaking a six month PhD internship at KPMG's corporate tax department in Manchester as a Research and Development Tax assistant, this involves writing technical reports for Tax Relief Claims for client such as Magnox limited, Sellafield, EDF etc. During his undergraduate degree, he worked as a Research and Development Trainee at Arcelor Mittal in Belgium. At Arcelor Mittal, he was assigned to work on a five months project which involved communicating coatings such as Piezoelectric and colour coatings on steel sheet and its applications. During this internship, he recommended capex purchase of machine for improving mixing of powders in preparing coatings which led to greater coating coverage and good product finish. His undergraduate degree was in Material Science and Engineering from the Queen Mary University of London where he was awarded the best final year undergraduate project.

Declaration and Copyright statement

No portion of the work presented in the thesis has been submitted in support of an application for another degree or qualification of this or any other university or other institute of learning.

The author of this thesis (including any appendices and/ or schedules to this thesis) owns certain copyright related rights in it (the "copyright" and s/he has given the University of Manchester certain rights to use such copyright including for administrative proposes.

Copies of this thesis, wither in full or in extracts and whether in hard or electronic copy, may be made only in accordance with the copyright, Designs and Patents Act 1988 (as amended) and regulations issued under it or, where appropriate, in accordance with licensing agreements which the university has from time to time. This page must form part of any such copies made.

The ownership of certain Copyright, patents, designs, trademarks and other intellectual property (the "intellectual property") and any reproduction of copy right works in the thesis, for example graphs and tables ("Reproductions"), which may be described in this thesis, may not be owned by the author and may be owned by third parties. Such intellectual Property and Reproductions cannot and must not be made available to use without the prior written permission of the owner(s) of the relevant Intellectual Property and/ or Reproductions.

Further information on the conditions under which disclosure, publication and commercialisation of this thesis, the copyright and intellectual property and/ or Reproductions described in it may take place is available in the University IP Policy (see https://documnets.manchester.ac.uk/DocuInfo.aspx?DocID=487), in any relevant thesis restriction declarations deposited in the University Library, The University Library's regulations (see http://www.manchester.ac.uk/library/aboutus/regulations) and in The University's policy on Presentation of Theses

Contents

List of Figures

List of Tables

List of Abbreviations

AG	Against grain
AGR	Advanced gas-cooled reactor
CCD	Charge coupled device
CT	Computed tomography
CTE	Coefficient of thermal expansion
DHP	Digital helium porosimeter
DYM	Dynamic Young's moduli
EM	Effective medium
Gilso	Gilsocarbon graphite
HS	Hashin-Shtrikman
KT	Kuster and Toksoz
LPO	Lattice preferred orientation
LVDT	Linear variable differential transformer
ODF	Orientation distribution function
PGA	Pile Grade A graphite
PGA-AG	Pile Grade A against grain
PGA-WG	Pile Grade A with grain
TEM	Transmission electron microscopy
VRH	Voigt-Reuss-Hill
WG	With grain
XRD	X-ray diffraction
CPV	Closed pore volume
OPV	Open pore volume

List of Symbols

M_v	Effective elastic modulus of Voigt bounds
M_R	Effective elastic modulus of Reuss bounds
μ_1, μ_2	The shear moduli of individual phases
E	Young's modulus
G	Shear modulus
M	P-wave modulus
υ	Poisson's ratio
K	Bulk modulus
CH_2	Methylene
C_2H_6	Ethane
H_2S	Hydrogen sulphide
H_2	Hydrogen
CH_3SH	Methyl mercaptan
A	Elastic compliance
σ	Stress
B	Material constant that characterises the plastic deformation.
ε	Total strain
E	Elastic modulus
P	Porosity
E_0	Young's Moduli of non-porous solid
$\emptyset$	Porosity
K_s	The bulk modulus of solid
K_{air}	The bulk modulus of air (void)
$\mu^{HS\pm}$	Effective shear moduli of Hashin Shtrikman bounds
K^*_{KT}	Effective bulk moduli of Kuster and Toksoz bounds

μ_{KT}^{*}	Effective shear moduli Kuster and Toksoz bounds
μ	Absorption coefficient
λ	Wavelength of electromagnetic radiation to the diffraction angle
d	the lattice spacing of the lattice plane
n	Integer
θ	Incident angle
$\varphi_1, \Phi, \varphi_2$	Euler angles
ψ	Pole distance
I_{α}^{corr}	Corrected intensity
I_{α}^{rand}	Intensity from the random sample
I_{α}	Measured intensity from the texture sample
r	The pore radius
V_L	Compressional wave velocity
V_T	Transverse wave velocity
R	The universal gas constant
T	Temperature
n	Number of moles
V	Volume of the gas
P	Pressure of the system
V_g	Grain volume
V_b	Bulk volume
V_T	Theoretical volume
V_C	Volume of the crystal
V_s	Volumetric stress
F	The frictional element
K_a	Squashing spring
K_b	The poroelasticity of the large pores

φ	Effective porosity percentage
ε_v	Volumetric strain
σ_1	Maximum compression direction

CHAPTER 1

1 Introduction

Artificially produced graphite as used in nuclear reactors is a porous (~20% porosity) polycrystalline material. It can be classified as an engineering material with several advanced applications, some examples of its use are:

- in the steel industry, it is used an electrode material for arc furnace applications, the anisotropy of graphites is one of the desired properties because it provides electrode with adequate flexural strength along its length [1, 2].
- the high electrical conductivity of graphite makes it desirable for use as electrodes and brushes in electric motors as well as in solar energy applications [1]
- while diamond is one of the hardest substance known, graphite is one of the softest. Graphite can also be used for pencil and as a lubricant or coating to reduce friction and corrosion [3].
- graphite is suitable for use in rocket nozzles, due to its excellent thermal shock resistance and,
- in the nuclear industry, high purity graphite (nuclear graphite) is used within a reactor as a moderator and reflector material, due to its low neutron absorption, and it is also an excellent high temperature material [4].

It is the latter application, in particular the simulation of changes due to fast neutron irradiation that the thesis is concerned.

Graphite bricks shrink when irradiated; pores and cracks are forced to close up to accommodate the crystal expansion, and take up thermal expansion on the c-axis of the basal plane [5]. These physical changes result in higher elastic modulus and strength of the material [6, 7]. Graphite shrinkage could lead to disengagement of individual component and loss of core geometry. Differential shrinkage in the graphite component can lead to the generation of internal stresses and component failure by cracking. The latter behaviour is complicated by irradiation induced changes in Young's modulus and strength.

These dimensional and modulus change have been associated with the irradiation-induced closure of many thousands of micro-cracks associated with the graphite crystallites due to crystal dimensional change [8].

The **aim** of this work is to simulate the effects of closure of microcracks in nuclear graphite not by irradiation but by external pressure, whilst measuring Young's modulus, and to see if there are

any synergies between the changes in properties due to the two mechanisms (Hydrostatic compaction and irradiation).

The harsh nuclear reactor environmental conditions (e.g. fast neutron fluence, radiolytic oxidation and high temperatures) need to be accounted for when considering the structural design and safety of core graphite structures. Safe design of graphite components requires full understanding of the mechanical properties such as Young's modulus, shear modulus and Poisson's ratio [7, 9].

The Young's modulus of a nuclear graphite can be measured using two different methods i.e.

- From the slope of the stress-strain curve close to the origin (tangent/secant/average modulus)
- The propagation velocity of an ultrasonic wave and the resonance frequency (dynamic modulus).

The value of Young's modulus calculated using these methods are not identical and there is limited information on the relationship between the moduli obtained using these methods [7]. Extensive studies have been made in order to establish an understanding of the behaviour of nuclear graphite under a variety of conditions, as well as to understand the structure-property relationships governing the behaviour of artificially produced polycrystalline graphite [8, 10, 11].

Since irradiation changes are related to opening and closure of porosity and reorientation of the crystallites in polycrystalline graphite, it is considered that an indication to the nature of these changes may be gleamed by loading graphite under high hydrostatic pressure (up to 200MPa) as a method of simulating crack closure. In the work reported here the effect of high pressure (hydrostatic loading, differential stress and dynamic loading) on the static and dynamic moduli of the nuclear graphite has been analysed and compared with each other. Mercury and helium pycnometers have been used to measure the open porosity in each graphite sample before and after hydrostatic loading. During testing the modulus was determined by monitoring the loading and by using strain gauges and in some cases directly by ultrasonic measurement, in order to investigate the effect of porosity distribution on static and dynamic modulus. In addition the porosity of the samples has been examined before and after hydrostatic deformation using X -ray micrography and is compared with the effective porosity distribution obtained using the mercury pycnometry.

The relationship between experimental dynamic modulus and porosity change is compared with literature data [12, 13] on the change in Young's modulus of irradiated reactor graphite (Magnox

PGA and AGR Gilsocarbon graphite), in order to investigate relationship between the hydrostatic compressed virgin samples and irradiated samples.

The research reported here combines measurement of mechanical properties of graphite under high pressure and compares the experimental results with predictions made using various effective medium models (Voigt, Reuss, Hill, Kuster and Toksoz, and Hashin-Shtrikman bounds) previously developed to explain and verify the pressure/property relationships in other materials (i.e. rocks and other porous materials). The effect of basal dislocation, surface energy, porosity closure and heat lost during hydrostatic deformation were also considered. Helium and mercury pycnometry was used to determine the porosity in loaded and unloaded samples. The behaviour of graphite under the different loading conditions mentioned above was also analysed and compared with each other.

This advantage of this approach to the investigation of crack closure in graphite is

- the author did not have the expenses and difficulties associated with irradiating specimens in a reactor or dealing with active material.
- in this approach, the whole volume of graphite is altered during loading, and one can examine the bulk property change, unlike in ion-irradiation where the irradiated volume is minute, leading to difficulties in property measurement.
- change in Young's modulus can be measured in real time whilst the cracks are closing.
- the experimental time scale is very short compared with irradiating samples.
- differential stress can be applied at different initial hydrostatic pressures and hence crack closure states.
- From a scientific point of view graphite is an unusual material with extremely interesting material properties; graphite properties and behaviour under loading is worthy of investigation in its own right. Therefore this work is not only of interest to the nuclear industry but it is an interest to science community as a whole

The design and safety assessment of nuclear graphite components is often based on empirical rules derived from material irradiation data, but the accumulation of operational experience have proven such empirical rules to be inadequate in some cases, therefore more understanding of the relationship between change in microstructures and bulk mechanical properties is required [14].

The changes in graphite properties in a reactor are driven predominantly by fast neutron irradiation (and radiolytic oxidation). Understanding graphite microstructural changes during

hydrostatic loading may help to reveal how the dimensional and property changes in graphite are influenced as the internal porosity is closed by irradiation-induced crystal dimensional change

CHAPTER 2

2 Theory and literature review

2.1 Importance of nuclear graphite in a nuclear reactor

During operation, graphite in a nuclear reactor undergoes significant property changes due to the nuclear reactor environmental conditions (i.e. fluence, radiolytic oxidation, high temperature). These effects change the crystal properties and microstructure of nuclear graphite in a complex manner. These property changes have been studied over many years [5]. Bulk graphite mechanical property changes influence the reactor core lifetime integrity. In order to understand the irradiation behaviour of bulk graphite, it is very important to understanding the behaviour of graphite crystallites. Graphite shrinkage may lead to disengagement of individual component and loss of core geometry; graphite expansion could lead to large forces between structures (component generation of high stresses i.e. higher Young's modulus) and component failure by cracking. Two of the most important considerations in designing a graphite moderator that will have a long life are designing for component integrity and design that will ensuring that changes in graphite core geometry are acceptable. Both these design issues are affected by irradiation induced dimensional change and changes to the thermal and mechanical properties [15]. Of particular interest are irradiation induced to changes to Young's modulus, which is also affected by radiolytic weight loss.

2.2 Manufacture of nuclear graphite; PGA & Gilsocarbon

An understanding of graphite microstructure which is determined by the manufacturing process is required, because this influence the quality and behaviour of graphite. In general graphite is an allotrope of carbon [16] and has many applications varying from pencil lead to electrodes. Nuclear graphite is used within a reactor as a moderator and reflector material (sustaining the nuclear fission chain reaction). For this purpose high purity graphite (free from neutron absorption material e.g. boron) is required. Nuclear graphite is also used for other features related to reactor cores, such as fuel sleeves, spacer rings, and shield-wall protection. Graphite was also chosen for use in a nuclear reactor due to its high thermal conductance and its high strength at temperature [17]. Anisotropic extruded pure petroleum coke graphite called Pile Grade A (PGA) was used in the construction of the early United Kingdom nuclear power

reactors (Magnox) while a much improved graphite called Gilsocarbon, a near isotropic moulded graphite manufactured from Gilsonite coke (natural asphalt mined in Utah, USA) was used as a moderator in the Advanced Gas-cooled Reactor [18].

2.2.1 Crystal and bulk physical properties of PGA and Gilsocarbon

The graphite crystal structure (as shown in the Figure 2.1) was first proposed in 1924 by John Desmond Bernal [19]. Graphite consists of layered planes of carbon atoms, the layers are stacked above one another in a staggered manner. The spacing between layers is approximately 2.3 times the distance between the adjacent carbon atoms in a layer.

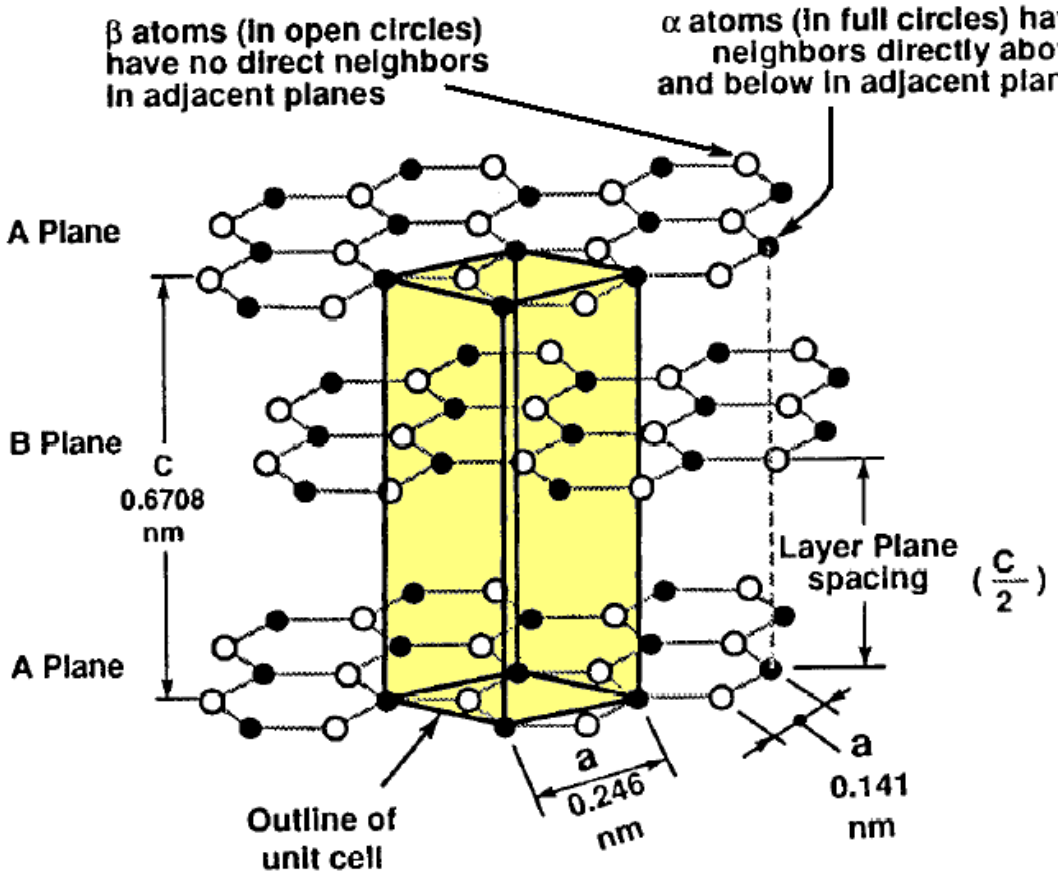

Figure 2.1 Crystal structure of Graphite showing ABAB stacking sequence and unit cell in Yellow (adapted from [16])

The crystal lattice has two main axes: the three directions along the basal plane (*a*-axes) and the direction perpendicular to the basal plane (*c*-axis). In each layer plane, the carbon atom is bonded to three other neighboring carbons to form continuous hexagons. The covalent bonding between two carbons is very strong (524 kJ/mol) and short in length (0.141 nm). The bonding

between layer planes is longer (0.335 nm) and weaker (7 kJ/mol) and is attributed to van der Waals forces [5, 16].

Table 2.1 Material properties of a graphite crystal at room temperature[20]

Property	Units	Value	
		***a*-axis**	***c*-axis**
Density	g/cm^3	2.267	
Interlayer spacing	10^{-12} m	335	
Mosaic spread	°	0.15	
Electrical resistivity	ohm-cm	40×10^{-6}	0.01 to 1.0
Thermal conductivity	watts/cm K	2 to 5	0.4 to 0.8
Thermal expansion	K^{-1} (20-100°C)	-1.5×10^{-6}	27×10^{-6}
Thermoelectric power	□ V/K	-5	not available
Magnetic susceptibility	emu/g	-0.3×10^{-6}	-21×10^{-6}

Table 2.2 Graphite crystal elastic tensor. All values are in GPa [21]

C_{11}	C_{12}	C_{13}	C_{33}	C_{44}	C_{66}	Bulk moduli
1109	139	0	38.7	5	485	36

Table 2.1 gives the materials properties of graphite crystals at room temperature. Stacking of graphite layer planes could possibly occur in two different orientations: rhombohedra (beta) and hexagonal (alpha) as shown in the Figure 2.2. According to Bosak et al. [21], the graphite single elastic tensor is shown in Table 2.2. The bulk moduli was estimated as 36 GPa [21].

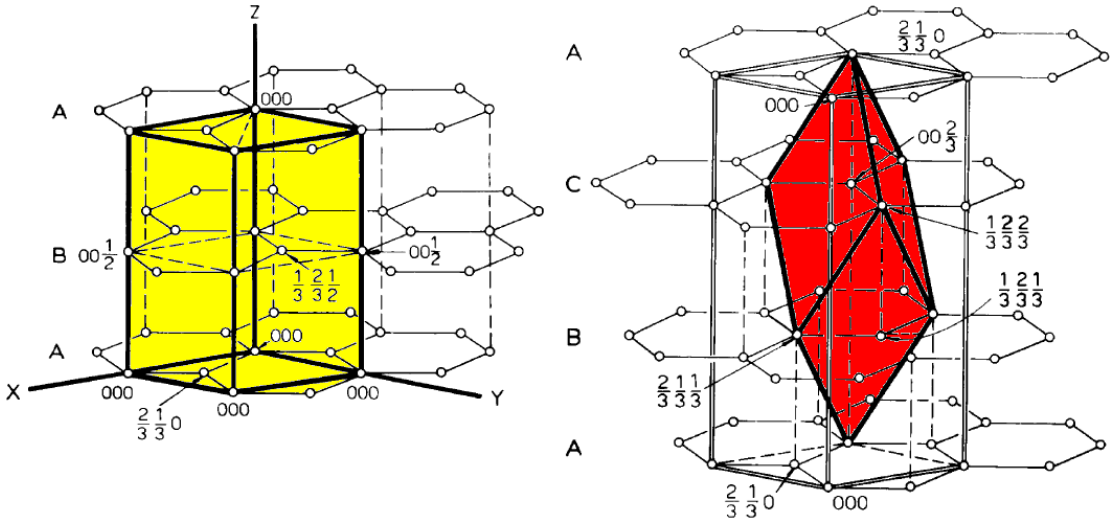

(A) **(B)**

Figure 2.2 Schematic of (A) Hexagonal and (B) Rhombohedral lattice of graphite crystal [22, 23]

The most common arrangement is hexagonal [24], the stacking of layer planes in the hexagonal structure is AB. The theoretically feasible Rhombohedral structure has a stacking order of ABC [25] but has never be found in pure form, as it is a thermodynamically unstable form of graphite that can be annealed out above 1300 °C [16]. Graphite is considered to be one of the purest forms of carbon [16], its purity is needed in nuclear applications to avoid absorption of low-energy neutrons and to reduce the production of undesirable radioactive species from impurities. Graphite used in a nuclear reactor is produced artificially; the basic manufacturing processes are shown in the Figure 2.2. The manufacturing is a "batch" process and it varies depending on the desired properties and application of the finished product (graphite). The basic raw materials for the production of graphite are a petroleum or pitch coke and a pitch binder [26].

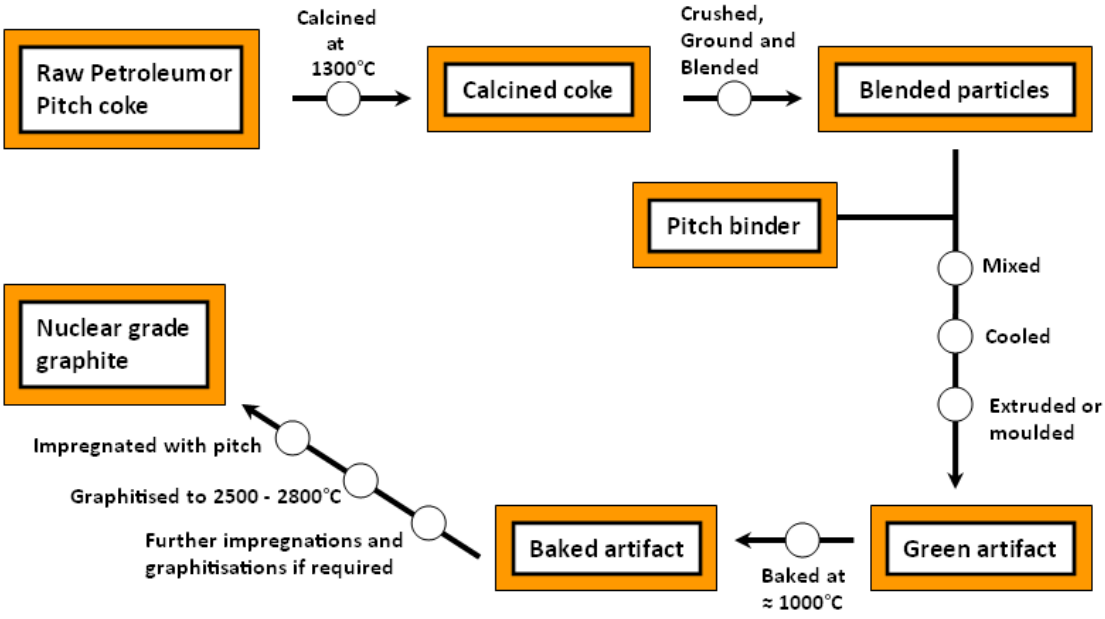

Figure 2.3: The manufacturing process for nuclear graphite (adapted from previous work [20, 25, 27])

The essential steps in the manufacturing process are: coke calcination, mixing, forming into green shapes, baking and impregnation, and graphitising. In addition in some cases a final purification step is required. The steps are outlined as follows:

- **Coke calcination:** Petroleum coke is a by-product from the processing of crude oil while pitch coke is manufactured from coal tar pitch or naturally occurring pitch. Petroleum coke has a poor crystalline structure which can be improved through heating; pitch coke structure is less ordered than petroleum coke. Coke is calcined prior to being processed into graphite [25]. It is heated to 1300 ^{0}C during calcination in order to remove any residual volatile hydrocarbons i.e. (methylene (CH_2), ethane (C_2H_6), hydrogen sulphide (H_2S), hydrogen (H_2) and methyl mercaptan (CH_3SH) [28], resulting in a materials volume reduction. The coke crystallinity is improved at the same time during heating. In PGA and Gilsocarbon, the coke is produced from petroleum and Gilsonite pitch respectively [29]. The calcined coke is crushed, ground and blended to obtain the required filler particle distribution before mixing.

- **Mixing (the binder):** Binder pitch is mixed with blended calcined coke. The binder is either a petroleum or coal-tar pitch. Coal tar is a thermoplastic material; it is solid at room temperature and it becomes viscous when heated. It is suitable as a binder for graphite manufacture because of its high viscosity at high temperature, high carbon content, high specific gravity, and because it is relatively cheap.

- **Forming into green shapes:** After mixing, the aggregate is then allowed to cool before being extruded or moulded into an artefact. The artefacts are of different sizes and shapes, depending on the initial type of coke used and are termed the "green artefact" although the article colour is not green. In PGA, the mixture is carefully extruded at constant pressure and rate, resulting in a general alignment of the filler particles, which are needle shaped, parallel to the direction of extrusion. The extrusion process gives rise to an anisotropic bulk material, In Gilsocarbon, the mixture is moulded resulting in a much smaller degree of directionality (alignment) of the filler particles. The degree of anisotropy is also influenced by the size of the particle (i.e. 0.5 - 1 mm) and source of the coke [25].

- **Baking and impregnation:** The green artefact is baked at 1000 ^{0}C, where the remaining volatile ash in the green artefact is removed and the pitch binder is carbonised. After baking, the density of the green artefact is usually between 1.65 g/cm^3 and 1.70 g/cm^3. The baked artefact is impregnated with pitch in order to increase the density and improve the final material properties. A higher density can be achieved by repeating the impregnation with a suitable pitch and then re-baking. The baking process leads to a distribution of gas evolution pores in the structure of the final material [27, 28]

- **Graphitisation:** Graphitisation involves a displacement and rearrangement of layer planes and smaller groups of planes to achieve a three-dimensional ordering. Carbon can be graphitised when heated at a temperature greater than 2500 ^{0}C in a furnace packed with coke dust and silicon sand to prevent thermal oxidation. An high degree of crystallinity is reached as the structure approaching a perfect crystal, resulting in changes to the material properties. Graphitisation takes 3-4 days [20, 28].

Historically, the manufactured nuclear graphite's density was 1.6-1.80 g/cm^3. The density of pure graphite crystal is 2.26 g/cm^3 compared with the density of PGA (1.74 g/cm^3) and Gilsocarbon (1.81 g/cm^3) [18, 30]. This suggested that both nuclear grades have ~20% porosity. The lower density of PGA compared to Gilsocarbon is due to the differences in porosity between the two nuclear graphite grades, which will be discussed later in this report.

2.3 Microstructural characterisation of nuclear graphite; PGA and Gilsocarbon

The graphite article produced during graphitization consists of inter-connected filler grains and a binder phase. This article is called polycrystalline graphite, due to the array of small submicroscopic graphite crystallites making up the filler and the binder phases. Crystalline size varies from 20-50 nanometer to a few microns in polycrystalline material [23, 31], their orientations depend on the manufacturing process.

Polycrystalline graphite structure includes graphite crystal lattice, grain size and shape, the degree of ordering within the tiny crystallites present in the polycrystalline phases, different pore size distribution, and shape. Coke particle size varies between 25-300 μm [25, 32], the particle size below 10 μm size are called flour [25]. In polycrystalline graphite, binder and filler are sometimes indistinguishable. The nature of the binder-filler boundary, their shape and size is not well understood. Filler particles consist of aligned crystallites and provide high strength to the material [33, 34]. PGA nuclear graphite has distinguishable alignment of the filler particles.

PGA was manufactured for early gas-cooled reactors and the filler particles are derived from the petroleum industries. PGA has an oval or needle-like shaped filler particle which is preferentially aligned with the extrusion axis. The bulk material had anisotropic material properties since the crystallites within the filler particle were preferentially aligned [10].

Gilsocarbon was manufactured for advanced gas-cooled reactors (AGRs) and the filler was obtained from Gilsonite (naturally occurring asphalt mined in the USA). It has spherical, onion shaped filler particles which have no preferential alignment during manufacturing process. The bulk material had near-isotropic material properties, as the crystallites within the filler particle tends to align circumferentially [10].

The filler particles in each graphite grade were highlighted with red mark as shown in the Figure 2.4. The black regions in the tomography are the porosity while the grey regions comprise the graphite block.

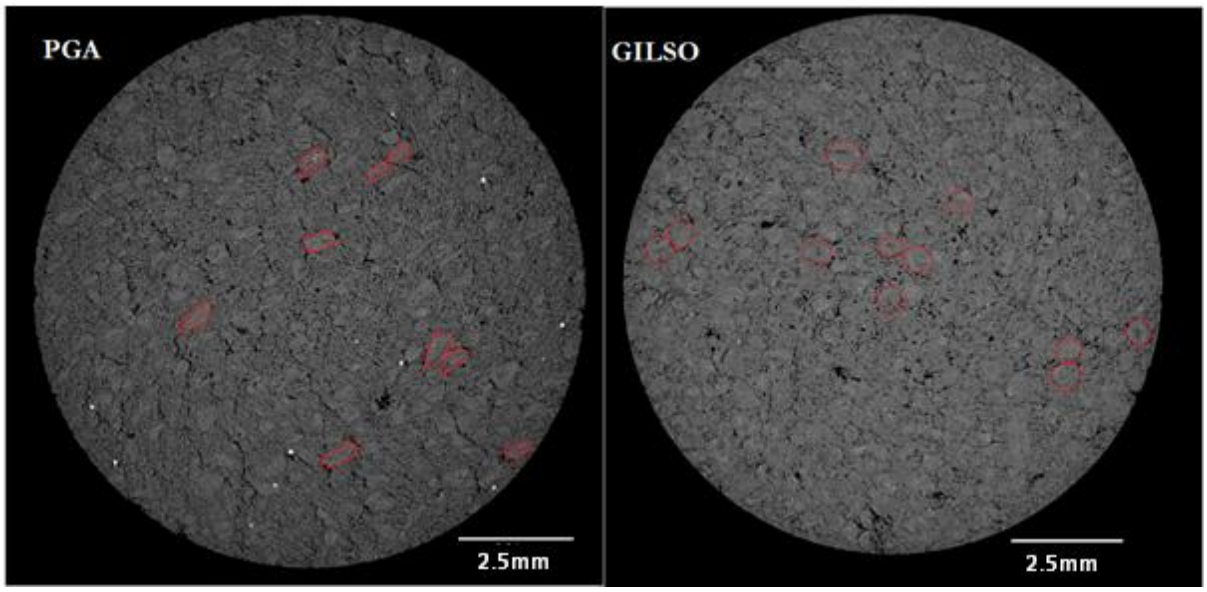

Figure 2.4 Tomography images of PGA sample (J12) and Gilso (Gilsocarbon (I8)). The filler particles in each micrograph were marked in red

The binder and impregnated crystallites in both graphite grades are randomly oriented with no preferential alignment. Extensive networks of interconnected pores, leading from the surface to the core are also a common feature; these are referred to as 'open pores' as they are accessible to gas or fluid. Isolated pores are referred to as 'closed pores' [35]. The manufacturing process described above gives rise to a population of porosity and crystallite orientations in nuclear graphite. Pore structures develop in the binder during the baking process. Binder can be characterised by '*domains'*, which are regions of common basal plane alignment extending over linear dimensions greater than 100 μm and '*mosaics'* which are regions of crystallite disorderliness with linear dimensions of common basal plane orientation of less than 10 μm [36].

2.3.1 Porosity in Polycrystalline Graphite

Previous work [4] investigated the porosity distribution in nuclear graphite and wide range spectrum of pores was observed as shown in the Figure 2.5. Pores can be classified into three families according to their size namely:

(a) micropores (very fine pores) < 2 nm,

(b) mesopores (fine pores) in the range of 2 nm - 50 nm and

(c) macropores (large pore) > 50 nm [37, 38].

The porosity populations can include gas evolution pores (micrometers in size), calcination cracks (micrometers in width and tens of micrometer in length), and Mrozowski cracks (nanometers wide and micrometers in length).

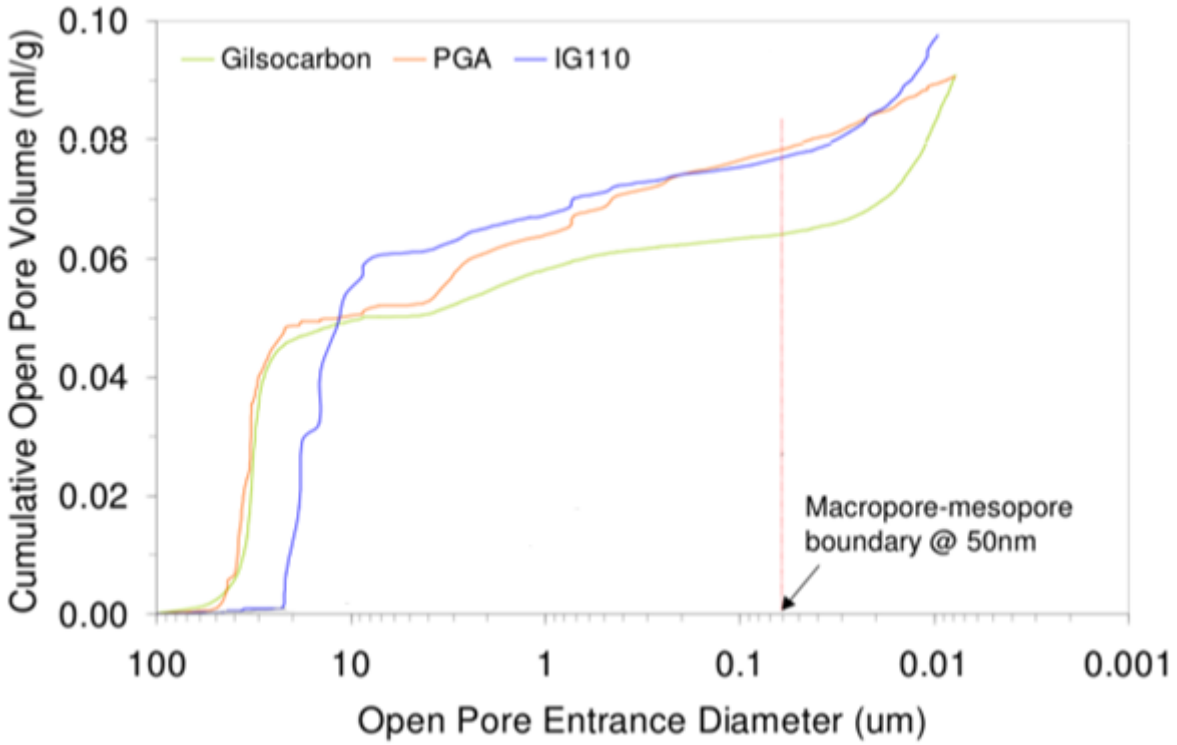

Figure 2.5 Mercury pycnometry result of pore size distribution in the nuclear graphite materials (adapted from Saheed [4])

- **Gas evolution pore:** During the baking of the green artefact, gases and hydrocarbons are driven off, resulting in cylindrical aspect ratio pores otherwise known as gas evolution pores [39] They are sometimes referred to as open porosity, as they provide the route for gases to penetrate into bulk structure.
- **Calcination crack:** Calcination cracks formed during the coking process. They are large cracks (few micrometers in length and width) and there are two types of this crack; lenticular cracks which are aligned around the filler particle and non-lenticular cracks from that crack through the layers. These crack populations are found in both nuclear graphites, which will be discussed later in this thesis.

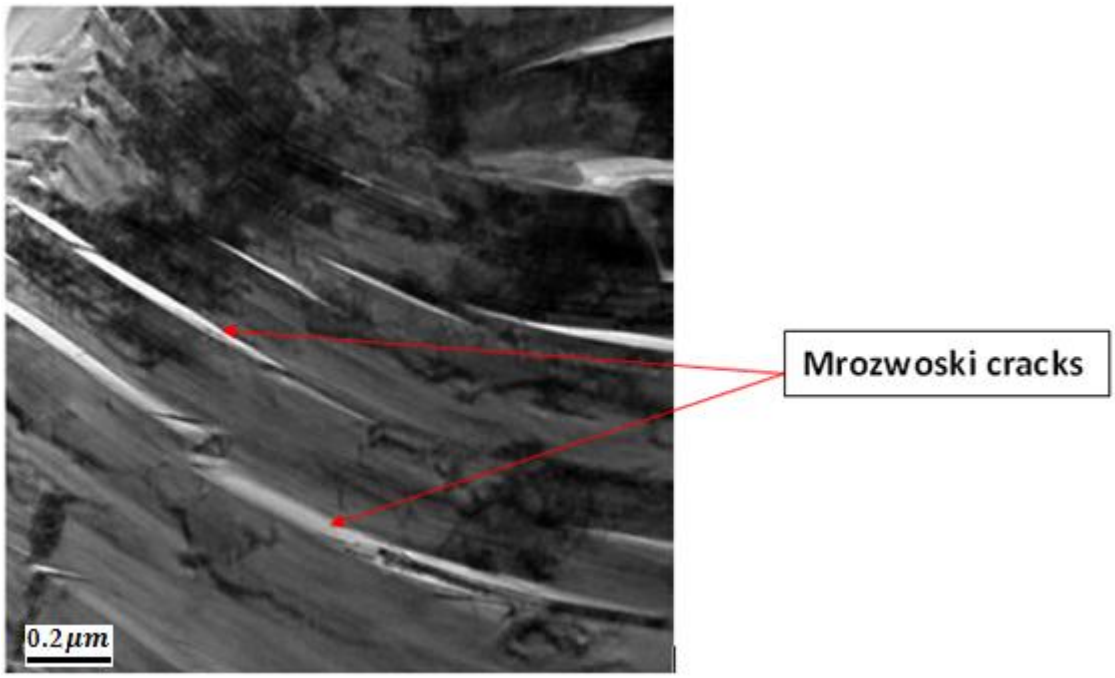

Figure 2.6 Transmission electron microscopy (TEM) image of nuclear graphite showing Mrozowski cracks (from Jones's work [2])

- **Mrozowski cracks:** These narrow cracks lie between the basal planes and arise from the anisotropic shrinkage of the crystallites during cooling from graphitisation temperatures. They are named after the author who first described their occurrence (Mrozowski) [40]. Typical Mrozowski cracks within Gilsocarbon graphite are shown in Figure 2.6. These are important features in bulk graphite as during irradiation the crystals swell and result in a closure of these cracks which affects to the bulk mechanical properties and cause dimensional changes. Moreover their formation can also be linked with internal stresses generated during cooling after graphitization.

At graphitisation temperatures above 2800 ^{O}C the thermal energy breaks the atomic bonds in the structure and reform during cool down until the structure shocked. The high c-axis coefficient of thermal expansion (CTE) results in local stresses with the structure. If there is a high local stress, the structure has to accommodate for this and microcracks form. These align parallel to the crystal c-axis [34, 39]. Mrozwoski cracks are present in the filler particle and binder. Mrozowski cracks range from 10 nm in width and few nanometers to over 1 μm in length (example of Mrozwoski crack show in Figure 2.7 [41].

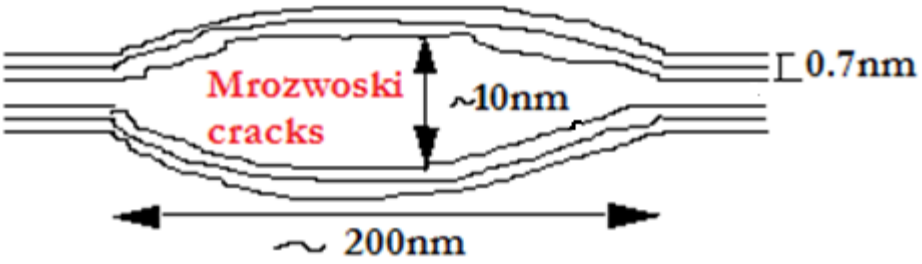

Figure 2.7 crystal lattice showing Mrozowski crack

2.4 Mechanical properties and hydrostatic deformation of polycrystalline graphite; bulk modulus, non-linearity and hysteresis behaviour - elastic properties

Graphite is a weak and brittle solid material; compressive strengths are 3-4 times higher than the tensile strengths [42]. The stress-strain behaviour is known for its non-linearity with load and a hysteresis loop forms during cyclic loading, with permanent deformation on removal of applied load. The uniaxial unconfined compression stress-strain relationships in polycrystalline graphite have been widely studied in the past. Seldin [42] and Jenkins [43, 44] showed a non-linear stress-strain curves similar to those shown in the Figure 2.7

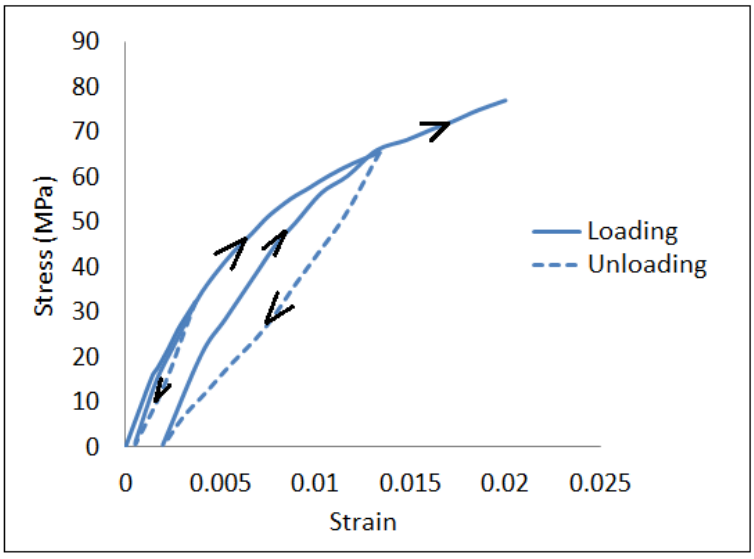

2.8 ATJ graphite specimen stressed in compression (adapted from Seldin's [42])

In uniaxial compression, the loading curve is convex upward while the unloading curve is always concave downward with permanent sets formed at zero stress. The permanent set increases

when the previous maximum loading stress increases. Greenstreet et al. [1] also investigated size effects and stress gradient upon the graphite material behaviour under flexural and uniaxial tests. The size effects (volume and cross sectional area) were reported to be small or non-existent within the size range investigated. Jenkins [45] relates graphite microstructural aspect to bulk material behaviour by deducing a mechanical analogy for use in predicting stress-strain behaviour in tension and compression. Elastic restraintt from the carbon network controls the extent of plastic deformation experienced by the grain. The higher the stress, the less the restraint of this network and more grains deform plastically. This carbon network allows non-linear deformation even at very low strain. According to Jenkin's model, the initial loading is described by

$$\varepsilon = A\sigma + B\sigma^2 \qquad \textbf{(2.1)}$$

Where,

ε = total strain

A = Elastic compliance,

σ = Stress,

B = Material constant that characterises the plastic deformation.

The first part of the Equation 2.1 represents the elastic strain and the second part represents the plastic strain. This general parabolic law fits the stress-strain curve fairly accurately at low stress and strain rate [45]. At high stresses, Jenkin's model deviates from the actual behaviour, probably due to a reduction in apparent modulus, caused by an increased in microcrack density.

The properties of the polycrystalline materials are affected by porosity since 10-20 % of the total volume is occupied by pores. There have been attempts to model the porous solid by relating their bulk modulus to volume fraction of porosity. Spriggs [46] and Hasselman-Hashin [47, 48] investigated the relationship between elastic Young's modulus, *E* and porosity, *P*. The following expressions were obtained respectively

$$E = E_0 e^{-cP} \qquad \textbf{(2.2)}$$

$$K = K_0((1-P)/(1-bP)) \qquad \textbf{(2.3)}$$

Where K_0 and E_0 are the moduli of non-porous solid at a given stress (i.e. $P = 0$), b and c are the empirical constants. Equation 2.3 was obtained for porous materials by Hasselman [47] from the approximate expressions for bulk modulus (*K*) of heterogenous media derived by Hashin [48]. Hashin's treatment is for closed pores while Spriggs equation is for total porosity in a volume of solid. Boey and Bacon [49] assumed that *K* for coated (Jacketed specimen) and uncoated

(unjacketed specimen) graphite is determined by the closed and total porosity respectively. According to Boey, the two equations above can only be applied to graphite, if it was further assumed that the empirical form of Equation 2.2 may be applicable to *K*, that Equation 2.3 applies to anisotropic solids and that the constants *b* and *c* do not depend on the nature of the porosity.

Brocklehurst et al. [50] investigated the effect of radiolytic oxidation on the properties of PGA and isotropic reactor graphites for weight loss up to 35%. It was concluded that properties such as thermal conductivity, Young's modulus and strength were reported to decrease with weight loss associated with increasing porosity (formation of microcracks).

Jenkins [51], Slagle [52], Oku and Eto [53] studied the formation or growth of cracks (increase in porosity) in nuclear graphite during loading (bending, compression) and it was concluded that there was an evidence for a buildup in crack density as original crack stabilized at pores and new ones formed. Oku and Eto [53] suggested that crack growth becomes more evident around 60 % of the compressive failure stress. It was also reported that the effect of pre-stressing shown a decrease in Young's modulus. The closer the stress approaches a critical value, the greater the probability of localised crack formed, hence the greater the decrease in Young's modulus. Hall [11] noted that the fall in Young's modulus value at low pre stress level is due to an increase in dislocation density which would recover completely following thermal annealing treatment.

2.5 Hydrostatic deformation investigation

Since the aim of this work is to develop an investigation of graphite response to hydrostatic loading, previous work by Paterson and Edmond [54], Boey and Bacon [49], Kmetko et al. [55] and Yoda [56] were investigated to other to establish the facts and assumption about graphite microstructural changes and there relevance to the authors research.

2.5.1 Paterson and Edmond's work

Paterson and Edmond [54] studied large uniaxially symmetric deformation of porous polycrystalline graphite (electrographite grade EY9) at high pressure. The specimen is enclosed during the test in a dilatometer which fits inside pressure vessel and permits simultaneous determination of volume change and stress/strain characteristics. This genius method is the pioneer of its kind. High hydrostatic pressure applied prior to differential stress suppressed deformation by growth of dilatant and microcracks. According to Paterson and Edmond, the large deformation might help in understanding the mechanisms of deformation of graphite. High

pressure experiments showed that the compression stress-strain curve of a polycrystalline graphite depended upon the applied confining pressure (1-8 kbar) [54]. In the work of Paterson and Edmond, volume changes occur during deformation as well as during application of pressure. There is almost complete recovery of length and volume during the release of pressure after 20% strain.

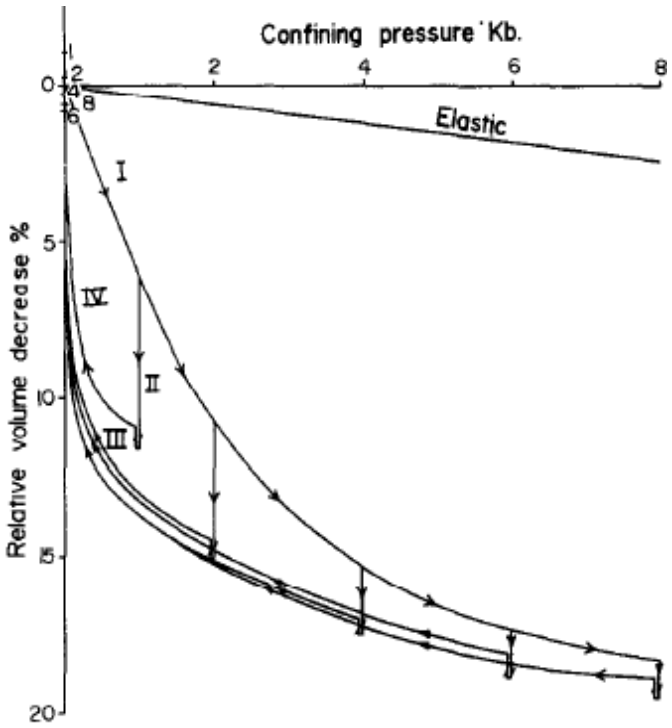

Figure 2.9 Total history of volume change during multiple high hydrostatic pressure cycling (Paterson and Edmond [54]). The elastic line represents the behaviour expected from single crystal compressibility modulus. The high pressure deformation apparatus used consists of a pressure vessel containing a fluid medium into which piston was introduced to apply a superimposed axial load to the specimen

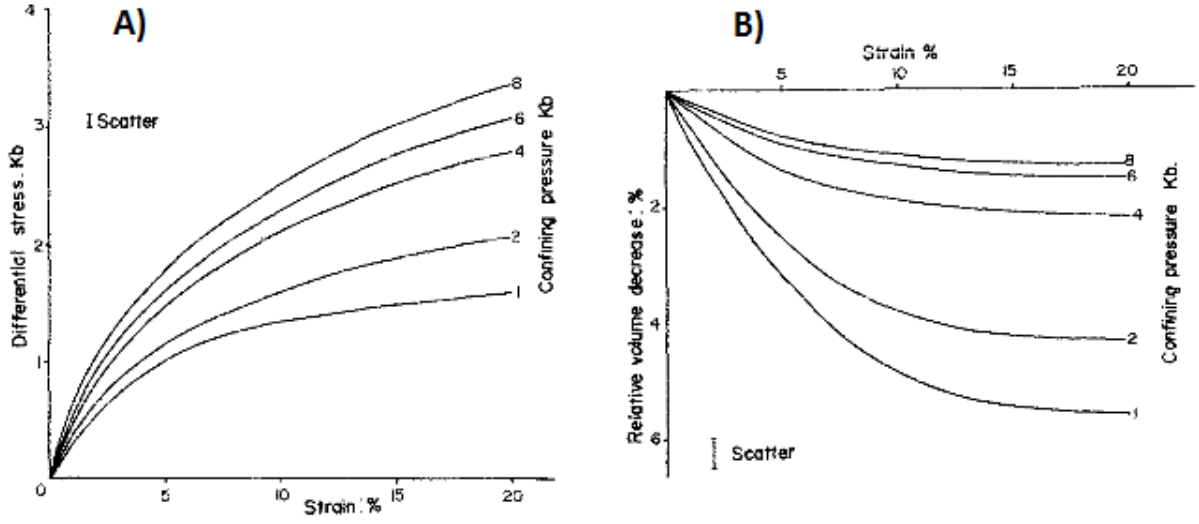

Figure 2.10 A) Compression stress-strain curves and B) Volume change during deformation at confining pressures from 1 – 8kb. The scatter represents the error bar

In the Figure 2.9, the volume of the graphite changes at various pressures. Each stage of the volume change was described as follows.

- Volume decrease as confining pressure increases.
- During the 20 % straining, volume decreases further at fixed confining pressure.
- Slight increase in volume on removing the differential stress (same confining pressure) as shown in Figure 2.10B.
- Large increase in volume during release of confining pressure, this recovers almost the initial volume, mainly below 0.5 kb

Above 1 kb, there is also length recovery, final length of the specimen is 1-2 % shorter than initial length. Paterson concluded that

- The stress strain curves (shown in Figure 2.10A) show strong dependence on pressure.
- Assumes that the deformation is due to sliding of granular particles against the resistance of macroscopic friction.
- When the high pressure is released the internal stresses are relived resulting in high strain recovery.
- The deformation may also accompanied by 'flexure of platelets' which could also introduces the internal stresses responsible for recovery effects.
- Opening of new cracks and pores during pressure release may also contribute to the recovery effects, including giving rise to additional volume recovery

2.5.2 Boey and Bacon work

According to Boey and Bacon [49], polycrystalline nuclear graphite density is less than that due to graphite crystals alone due to the presence of porosity which has implications for the bulk compressibility. The work of Boey and Bacon [49] was to investigate on unirradiated and irradiated deformation behaviour of several graphites under a gas pressure up to 4.14 MPa (600 psi) and the effect of increasing the closed porosity on hydrostatic deformation of graphite.

Boey and Bacon [49] hydrostatically deformed various uncoated and coated virgin Gilsocarbon, PGA moderator graphites and pitchcoke (fuel sleeve graphite). The results are shown in Figures 2.11 and 2.12, (the symbol (l) represents a sample cut in the longitudinal direction while (c) represents samples cut in the circumferential direction). Both virgin coated and uncoated graphite samples exhibit linear pressure strain relationship. There was reduction in strain in the uncoated specimen for a comparable pressure compare to coated sample, Boey and Bacon concluded that the coated specimens are stiffer that uncoated specimens [49].

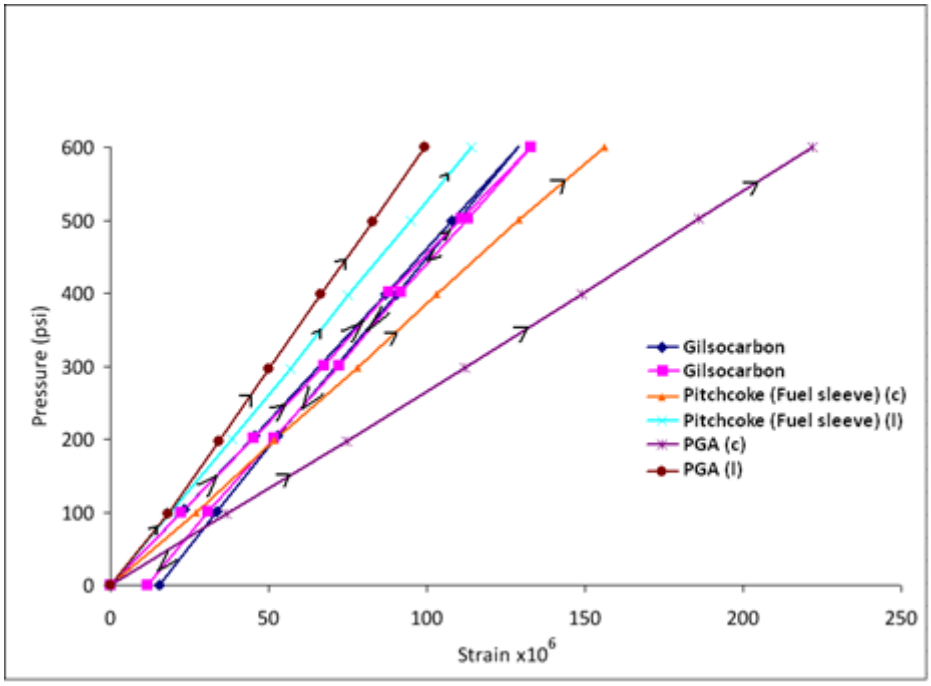

Figure 2.11 Pressure versus strain for uncoated specimens of virgin graphite (adapted from Boey and Bacon [49])

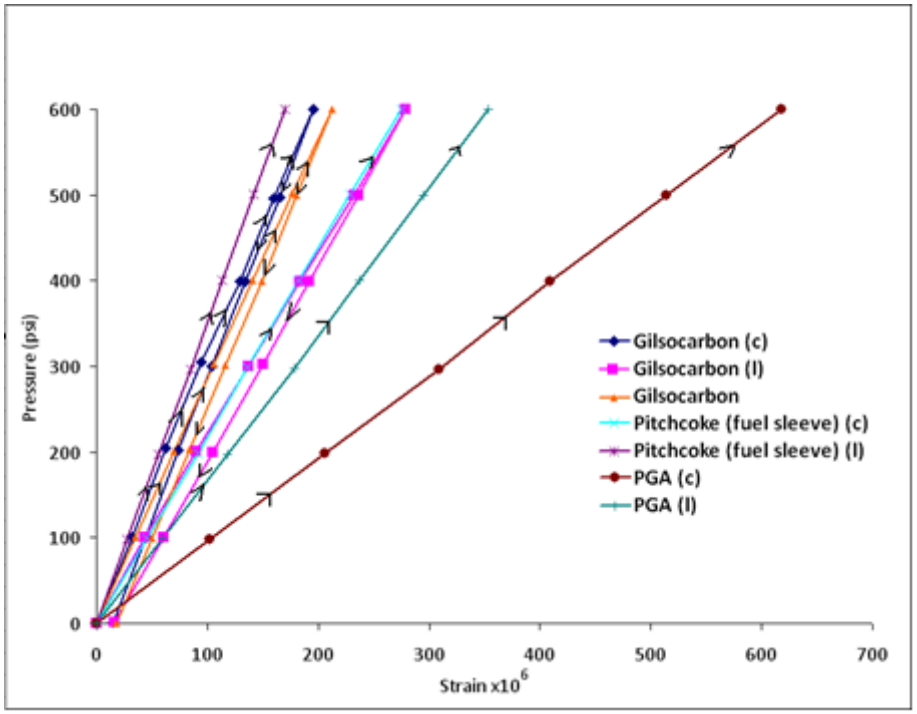

Figure 2.12 Pressure versus strain for coated specimens of virgin graphite (adapted from Boey and Bacon [49])

The result for the hydrostatic deformation of uncoated irradiated fuel sleeve graphite is shown in the Figure 2.13. These irradiated uncoated specimens exhibit a non-linear pressure/strain relationship and large hysteresis looping behaviour is exhibited.

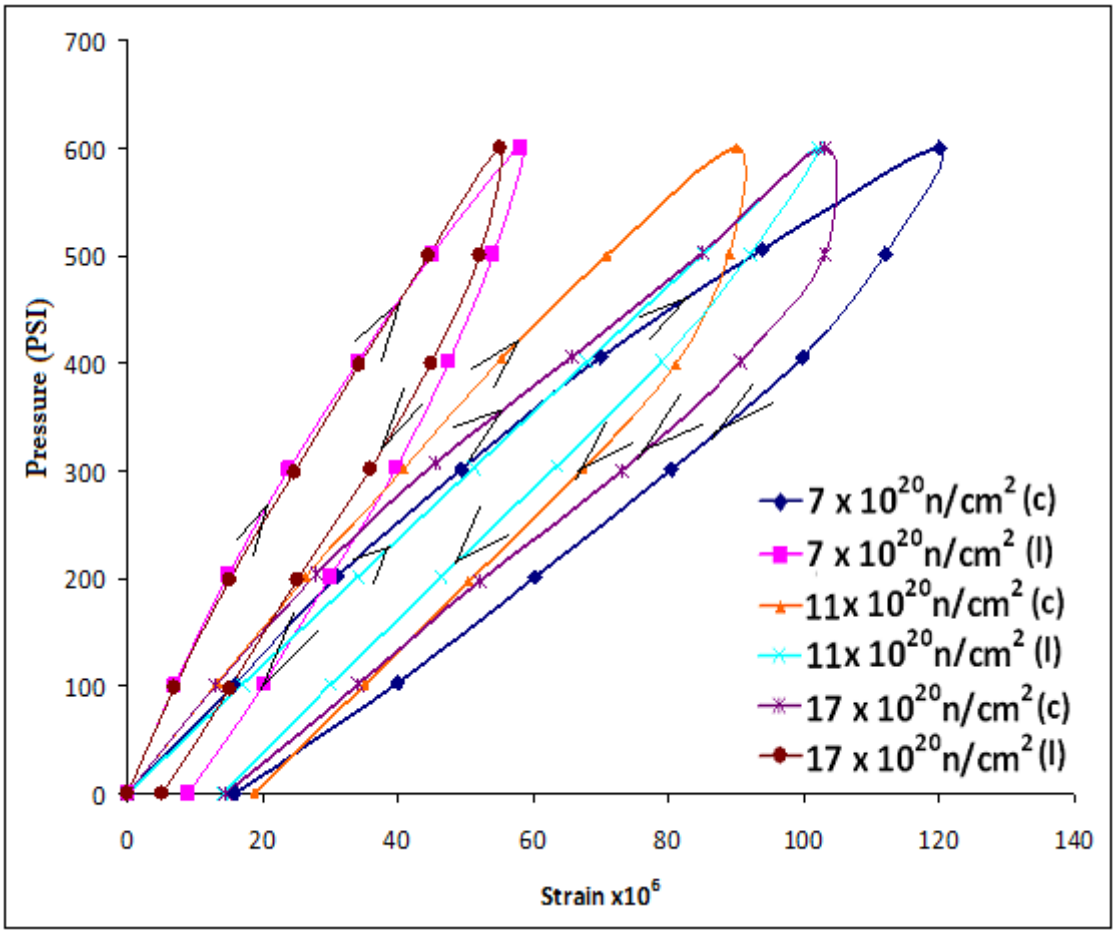

Figure 2.13 Pressure versus strain for uncoated specimens of graphite irradiated to a neutron dose of 7, 11, and 17x10^{20}n/cm^2 in circumferential (c) and longitudinal strain (l) directions (adapted from Boey and Bacon [49]).

It was noted that the circumferential loops were generally larger than those observed in the longitudinal direction, but in Graphite irradiated to neutron dose 11x1020n/cm2, the longitudinal strains was slightly larger due to the fact that the specimens were machined in the circumferential from the sleeve material.

In the irradiated samples there is a reduction in strain for a comparable pressure compared to unirradiated samples, implying that the irradiated graphite is stiffer than unirradiated graphite.

Table 2.3 Summary of Boey and Bacon results [49]; unirradiated graphite samples and Sleeve C (Irradiated sample)

Graphite sample	K (Uncoated) GPa	K (Coated) GPa	Close-pore volume fraction	Open-pore volume fraction	Uniaxial test E (GPa)	Poission ratio (ν)	$K = E/3(1-2\nu)$
Gilso A	10.7	6.1	0.09	0.11	7.9	0.17	4.0
Gilso B	10.0	7.3	0.10	0.09	7.9	0.13	3.6
Sleeve C	9.3	6.2	0.09	0.09	12.3*	0.15*	-
PGA D	7.3	2.5	0.04	0.22	7.8*	0.12*	-
Sleeve C (irrad)	14.0	7.8	0.11	0.09	-	-	-

(*denote longitudinal loading)

A summary of Boey and Bacon [49] values for Young's modulus E and Poisson's ratio υ obtained from static uniaxial tests are given in the Table 2.3. There is considerable variation in bulk modulus K between graphites. The value for sealed graphite is reduced significantly. The bulk modulus (K) for irradiated sample is higher than for the virgin samples as shown in the Table 2.3. Boey and Bacon suggested that the elastic changes were due to the changes that took place in the graphite microstructure, which contains spectrum of pores inherited in the raw material or arise from the graphite manufacturing process. Boey and Bacon concluded that

- K is reduced when graphite sample is sealed.
- Under uniaxial loads, all pores can assist in accommodating normal and shear deformation thereby contribute to E and υ, which correspondingly reduced.
- Under fluid pressure, deformation in open porosity is restricted because of its accessibility to fluid, closed micropores shrink, K decreases.
- Microcracks present in the grains reduce the restraint on plastic deformation that crystallites experience due to their neighbours while macropores within the binder phase can accommodate the shear deformation of individual particles.

2.5.3 Study of Kmetko et al. [55]

Kmetko et al. [55] studied the hydrostatic compression of synthetic polycrystalline graphite (AUC graphite) and the effect of pore structure accessibility. The sample was studied under two conditions:

- sealed in a 2-3 mm thick copper jacket to prevent confining fluid (pentane) penetration into the graphite pores
- not jacketed, to allow fluid penetration.

The length change was measured with dilatometer located inside the pressure vessel, the result from the two conditions are significantly different to each other as shown in the Figure 2.14. The displacement observed in the jacketed sample is non-linear and has a larger magnitude compared with the unjacketed sample. In the unjacketed sample, the compressive stress was applied to individual crystallites comprising rigid cross-linked of solid. In the jacketed sample, the hydrostatic stress was applied to the outside boundary of the graphite therefore the whole microstructural (crystallite network including porosity) was compressed, leading to large strain of jacketed sample as shown in the Figure 2.14.

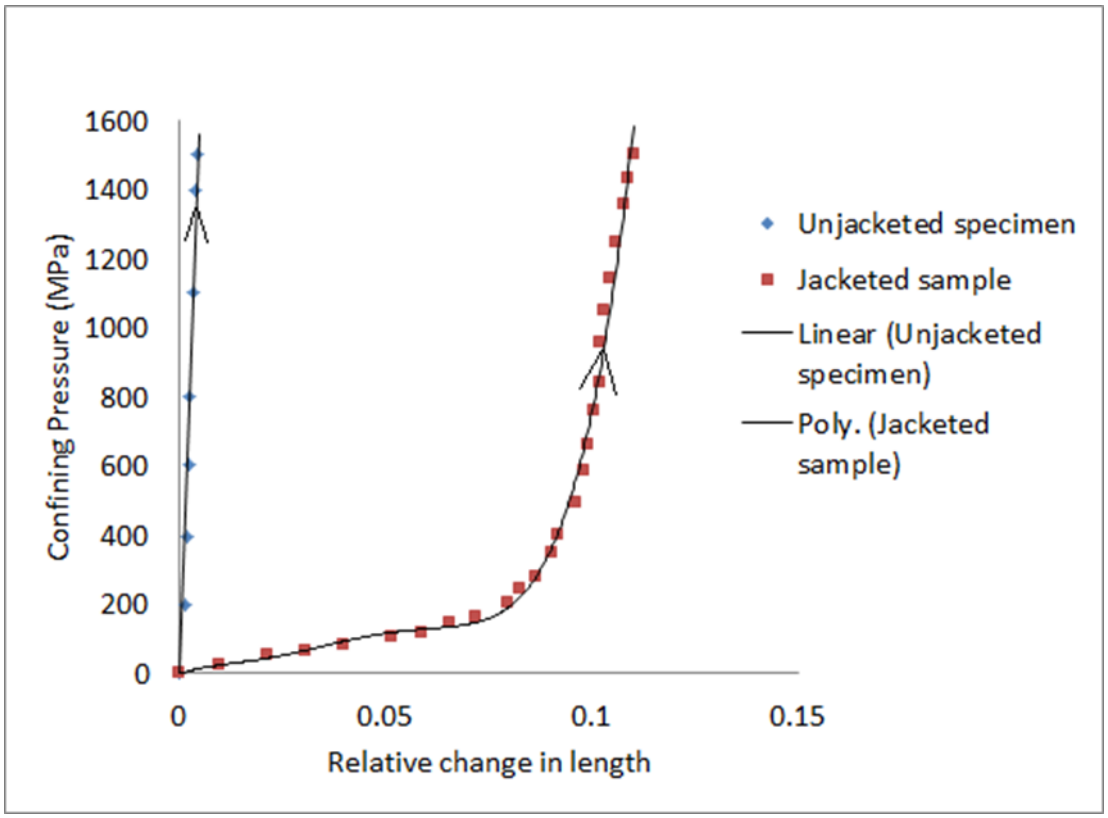

Figure 2.14 Displacement of AUC graphite along the extrusion direction during hydrostatic compression (adapted from Kmetko el al. work [55])

Kmetko et al. concluded that:

- The difference in behaviour is attributed to the effect of porosity of the AUC graphite.

- Graphite experienced slight deformation when unjacketed but grossly deformed when jacketed and subjected to pressure.
- It was estimated that the total volume decrease of 30 % below 600 MPa suggested that virtually all of the porosity has been closed.
- The coefficient of thermal expansion (CTE) is estimated to be ~0.4 greater perpendicular than parallel to its direction of extrusion [55, 57].
- The compressibility of unjacketed graphite sample is 0.35 times that of the jacketed materials in its densified state above ~600MPa. This value is approximately the fraction of the volume CTE for AUC graphite to that of the single crystal which is in agreement with the assumption that the structural sensitivities of thermal expansion to that of compressibility are similar.
- Hydrostatic deformation changes polycrystalline graphite's macroscopic dimensions in a similar manner to the thermal contraction of the aggregate

2.5.4 Work from Yoda et al. 1984

The aim of the Yoda et al. [56] work was to understand the characteristics of ISO-20 and IG-11 polycrystalline graphite under hydrostatic stress. These are fine-grained isotropic graphites manufactured by Toyo Tanso limited. The samples were hydrostatically loaded in a piston-cylinder type pressure apparatus up to a maximum confining pressure (fluid medium) of 600 MPa. ISO-20 was subjected to 2 cycles while IG-11 was subjected to 3 cycles, and the change in observed axial elongation as the pressure increases are shown in the Figure 2.15. During the first cycles the total deformations at the unloading and reloading points increased with increased cycle number, indicating that there was a slight increase in the apparent density during cycling.

ISO-20 seems to be stiffer than IG-11, Yoda et al. suggested that this behaviour might be due to the high density and unconfined compressive strength (1.90 g/cm^3, 140 MPa respectively) of ISO-20 compared to that of IG-11(1.75 g/cm^3, 80MPa respectively).

The relationship between the axial strain and volumetric strain for large strain deformation of an isotropic solid was considered. The large strain (ε) is ~ 0.05, the quadratic elongation (λ) could be written as $(1+\varepsilon)^2$ or $(\varepsilon)^2$. The volumetric strain was calculated as 0.156 using the quadratic elongation equations. For small strains (where $\varepsilon^2 \ll \varepsilon$) the volumetric strain is calculated as 0.15 by adding $\varepsilon_1, \varepsilon_2 \; and \; \varepsilon_3$. The difference between the two calculated volumetric strains is small (0.006).

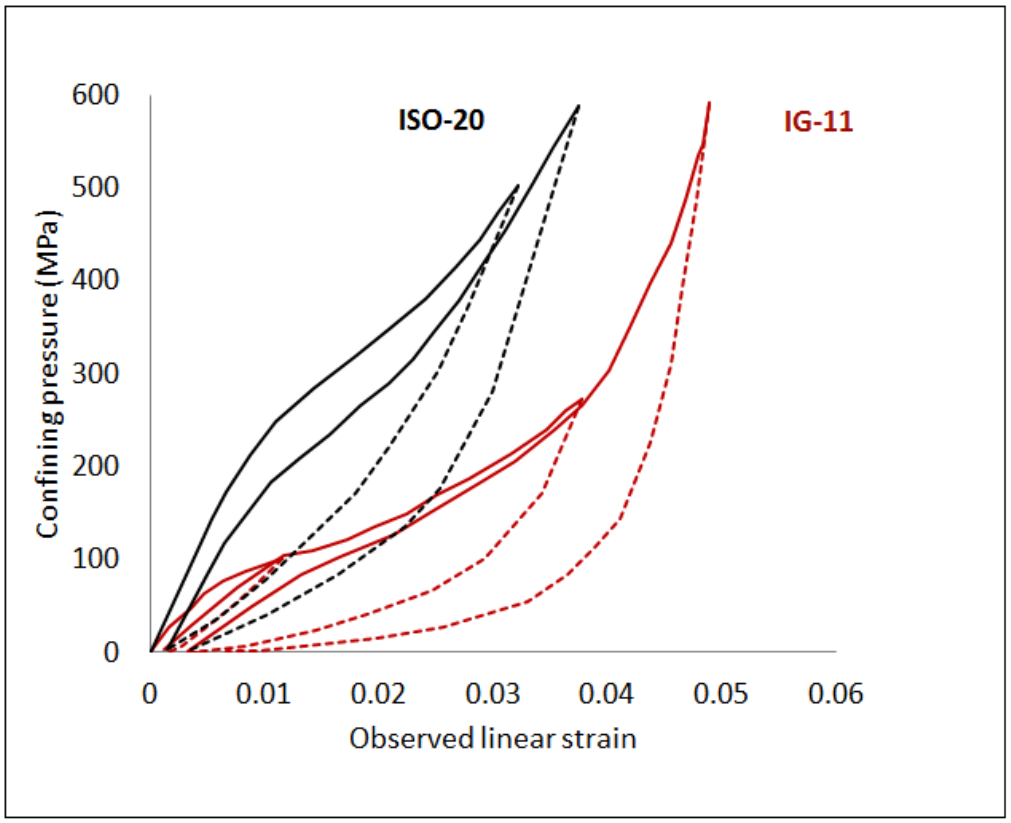

Figure 2.15 Hydrostatic pressure versus observed strain curves showing deformation behaviour of IG-11 and ISO-20 (adapted from previous work [56])

Yoda et al. [56] concluded that

- The concave shape of the curve at higher pressure would be identified by the shrinking of pores in the graphites caused by the pressure [56].
- At high pressure, the graphite is expected to behave as a hypothetical graphite without pores.

2.5.5 Basis of the author's work

Although all the previous work suggested that closure and opening of cracks play a major role in the non-linear and hysteresis loop behaviour of graphite under hydrostatic loading, none of the previous work analyses the contribution of porosity sizes to the graphite behaviour. Even though Boey and Bacon [49] analysed the total porosity change before and after deformation but the effect of porosity sizes were unknown which made it difficult to understand which porosity size scales (micopores or macropores) have the major effect on graphite behaviour under load. It is considered by the author that the knowledge of pore size distribution will help to reveal the dominant features in the graphite microstructure, whether the **binder** which has high concentration of both micropores and macropores or the **filler particles** that have high

concentrations of microcracks. Moreover the internal microstructural changes before and after hydrostatic deformations were not examined by previous work. In the present study, highlights regions of interest in the graphite micrograph before and after deformation are highlighted. The effect of hydrostatic pressure on crystallites is also examined.

2.6 Effect of irradiation on elastic property changes in nuclear graphite

Carbon and graphite have been widely used as structural materials for the high temperature environment (furnace, nuclear reactors and aerospace), due to their superior toughness at high temperature. The elastic modulus and strength of nuclear graphite increase with temperature [12, 58], the elastic modulus shows maximum value at 1800 ^{O}C, while the tensile strength reaches maximum around 2500 ^{O}C above [59]. Characterisation of the mechanical properties (i.e. elastic moduli) of graphite is fundamental to determining the induced and applied stresses on the graphite components in a reactor. Determining the resulting stress within and around the graphite component from the exposure to a reactor environment is necessary to estimate the ability of graphite to withstand the imposed loads and continued service conditions. Therefore it is paramount to develop a database of the properties for a given graphite grades (i.e. PGA and Gilsocarbon).

2.6.1 Fast neutron effect

Fast neutrons produced by the fission process in a reactor collide with the nuclei of carbon atoms (primary atoms) in the graphite moderator and transfer energy to them. If the bonding energy of the carbon atom in the lattice (≈ 5 eV ≈ 500 KJ/mol) is less than the energy of energetic neutron, primary atoms will be knocked out from the lattice and collide with another atom causing further displacements and projectiles in a cascade effect through the crystal as shown in Figure 2.16 [58].

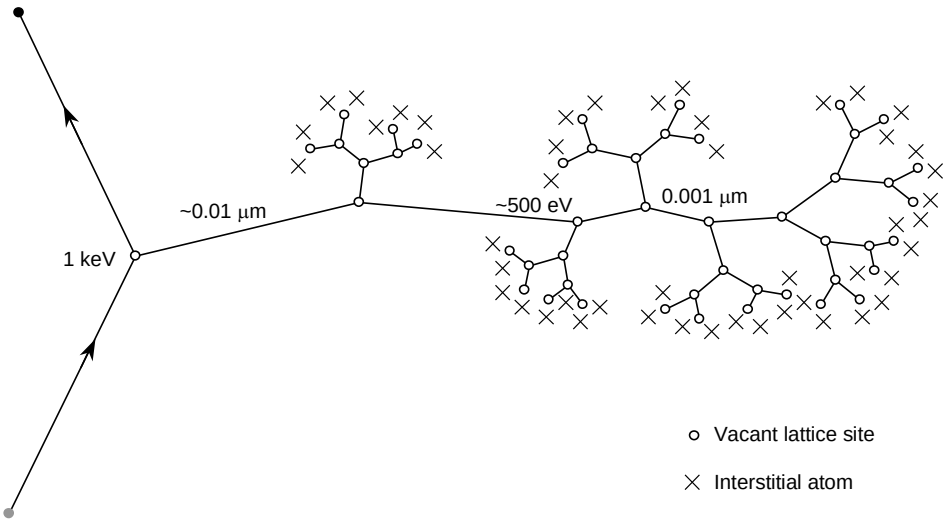

Figure 2.16 Schematic of displacement cascade in graphite crystal (adapted from [20, 58])

The initial collision between a carbon atom and a neutron produces a large number of displacements in the form of either interstitial carbon atoms and/or vacant lattice defects. Interstitial defects may form when an atom occupies a position between normal lattice positions, and vacancy defects occur where atoms have been removed from its lattice position. Previous works [5, 60] have proposed damage mechanisms of neutron irradiation in graphite crystals.

It was suggested [5] that the vacant lattice sites can be considered to be stable while the interstitial atoms move in between the basal planes. Violent thermodynamically stable concentration of thermal produced defect, it was previously proposed that large numbers of the mobile interstitial atoms might recombine with the vacant lattice sites (annihilation) [5] while some of them combine with one another to form small interstitial groups or clusters with a stable size of 4 ± 2 atoms. The interstitial groups may collapse under further neutron irradiation. The size and number of these interstitial groups that can be formed is a function of temperature, speed of transport through the graphite crystal and time. As the temperature is increased, the groups can potentially form bigger clusters and the group quantity is reduced. Moreover it was suggested that vacancies can be filled without interstitial annihilation resulting in increased lattice strain [58]. This lattice strain damage mechanism causes significant structural (i.e. dimensional changes) and property changes (i.e. elastic moduli) to graphite [61]. These damage mechanism above is postulated to cause crystal growth perpendicular to the basal plane (c-axis direction) whereas shrinkage parallel to the layer planes (a-axis direction) is said to be due to vacancy formation, Poisson's ratio effect and c-axis expansion [39, 60, 62]. Since the polycrystalline graphite consists of random orientations of filler particles and crystallite cracks and porosity,

polycrystalline graphite dimensional changes are governed by the irradiation - induced changes in the crystallites and interaction of porosity with the crystallites [61].

In polycrystalline graphite, there is initial expansion in the crystallographic *c*- direction due to interstitial defect formation and shrinkage in the *a*- direction due to coalescence of vacancies, hence graphite net volume shrinkage is observed [61]. During neutron irradiation, the cracks and pores start to close up in order to accommodate crystal expansion in the *c*-axis. These physical changes are postulated to result in higher elastic modulus and strength of the material [61]. The Young's modulus of irradiated graphite may be increased by three times its value before neutron irradiation as shown in Figure 2.17. Accumulation of new pores at high dose is thought to reduce the strength and modulus [61]. In Figure 2.17, increasing the temperature to 600 ^{O}C increases the rates of the second increase and of the decrease, but the maximum Young's modulus reduces slightly. It was also noted that the dose at which the Young's modulus decreases also reduces with increasing temperature [34]. Graphite strains by localized slipping of the basal plane. At lower dose, the pinning of dislocations suppresses anelastic behaviour causes an increase in Young's modulus. This is otherwise known as irradiation stiffness. The effect on Young's modulus is known as "pinning". Further increase in Young's modulus after irradiation stiffness due to pinning is attributed to structural tightening due to crystal swelling or crystalline deformations. This behaviour is referred to as a structural effect. Eventually, the DYM falls with further increase in dose due to generation of cracks within the microstructure associated with weight loss caused by radiolytic oxidation

Other work [5, 6, 60] on irradiation behaviour of nuclear graphite concluded that volumetric changes were similar to the changes mentioned above (initial densification followed by a rapid expansion). As the neutron flux increase, this densification increases until all the pores were exhausted and the c-axis expansion of the crystallites was able to be transmitted to the bulk material. This signified the beginning of the expansion phase where a large porosity formed between the filler particles at high doses and accounted for the large volume expansion of the graphite.

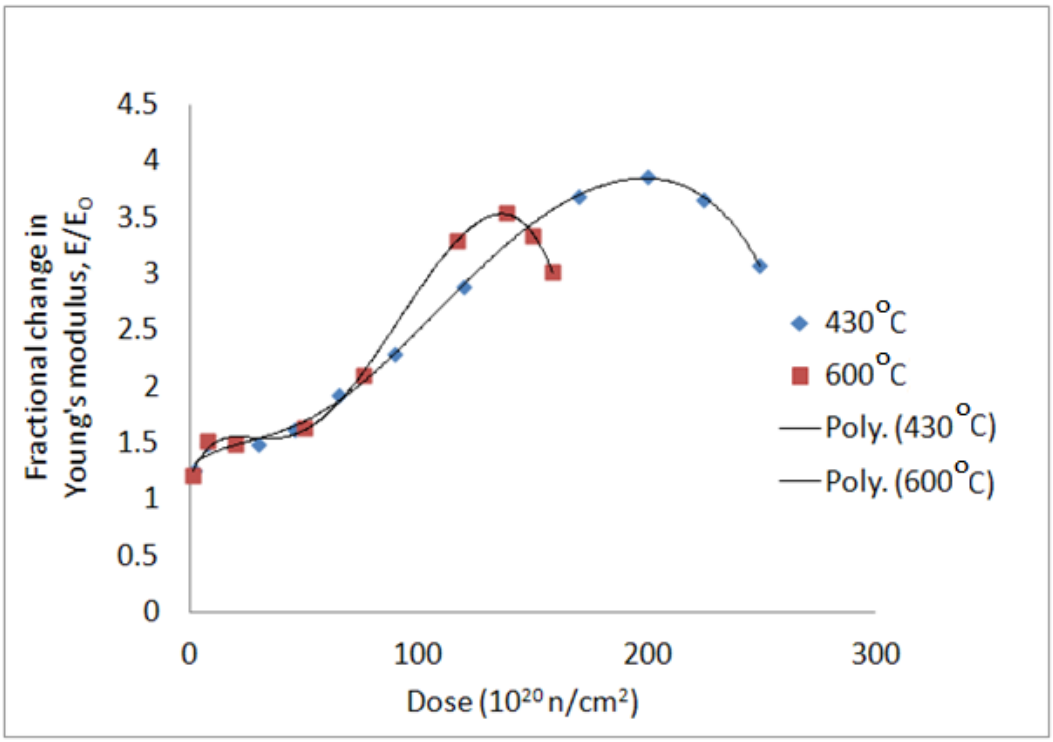

Figure 2.17 The effect of fast neutrons on the Gilsocarbon Young's modulus (adapted from [34])

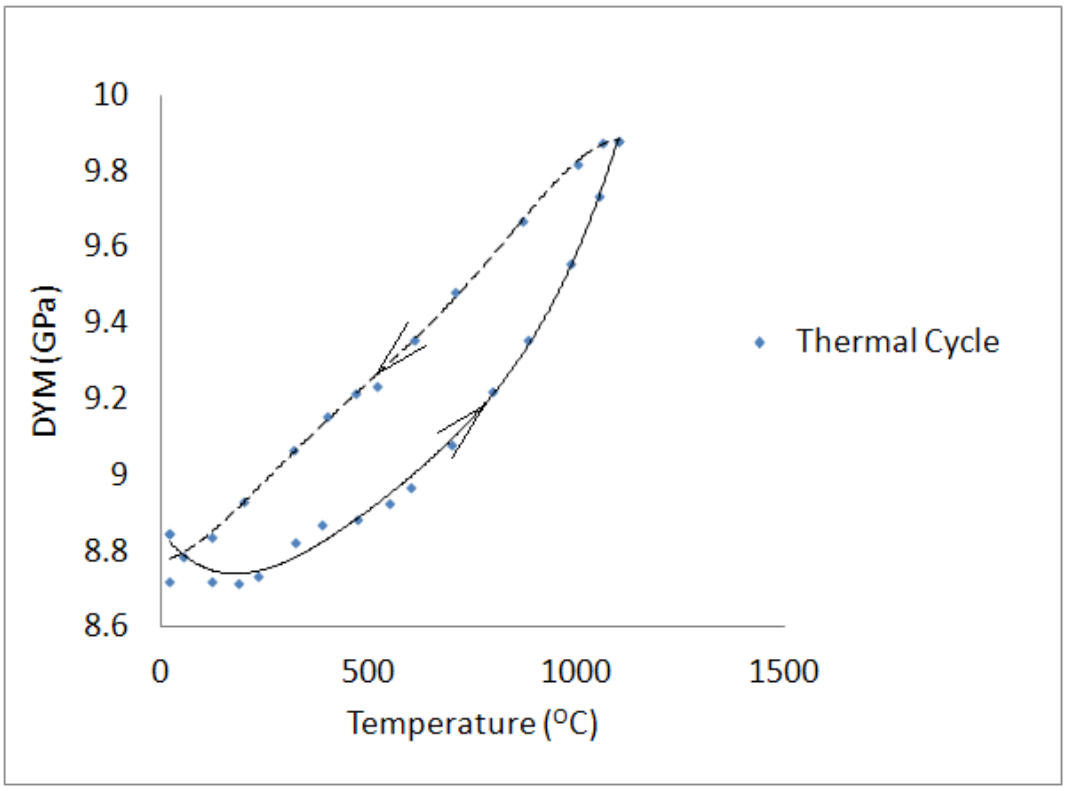

Figure 2.18 The effect of thermal cycling (between ambient temperature and 1100°C) on the DYM of Gilsocarbon (transfers direction). The solid line represents heating while broken line represents cooling (adapted from [63])

A well known characteristic of polycrystalline graphite is that the elastic modulus rises with an increase in temperature, for temperatures well above room temperature (i.e. 250-300 ^{O}C) [64]. As the temperature increases further (>~250 ^{O}C), the modulus increases up to 10 %. This might be associated with tightening of the graphite structure and closure of porosity. Thermal cycling showed that after heating up to 1100 ^{O}C and cooling to ambient temperature, the modulus decreased slightly by 1 %.

The changes in Figures 2.17 and 2.18 have been related with mechanisms such as crystallite swelling, formation and closure of porosity, pinning (pinned dislocations in the basal planes) in the case of irradiation and tightening of the graphite structure [20].

2.6.2 Oxidation effects

Several studies have been made of the relationship between the graphite pore structure and their oxidation characteristics [34, 50, 65-67]. In graphite moderated reactor cooled by carbondioxide (CO_2), some degree of graphite oxidation will occur. The gas contained in the open pores of the graphite material absorbs radiation energy (gamma radiation), causing CO_2 to breakdown into active species (CO_2*) which attack the graphite material (pore surface) as shown in the Equation 2.4. This process is called radiolytic oxidation. It adversely affects the physical properties of graphite and results in the enlargement of existing pores. The knocked-out carbon atoms in graphite leave vacancies, which can then be enlarged by reacting with the carbon atoms in the gaseous phase. According to previous work [50, 65] the most noticeable effect of oxidation on graphite microstructure is the enlargement of the pores caused by reaction of carbon atoms of the solid material with the oxygen molecules of the gas phase.

$$CO_2 + \text{Radiation} \rightarrow CO_2^* + \text{C(graphite)} \rightarrow 2\text{CO} \qquad (2.4)$$

The density of oxidized graphite is altered by enlargement of existing pores, new pores generation, and development of micro failure. Radiolytic oxidation occurs uniformly throughout the specimen and this removal of materials from the internal surfaces affect the physical properties of the graphite [50].

Radiolytic corrosion can be controlled by the addition of methane inhibitor to the CO_2 coolant. Methane protects graphite by forming a carbonaceous film on the surface of the pore, corrosion becomes increasingly inhibited to low surface area pores. In the recent AGRs, the use of improved near-isotropic Gilsocarbon as the moderator readily controlled the corrosion to an

acceptably low rate, due to low open porosity volume (~0.10 cm^3/cm^3) compared with PGA in the Magnox station which has higher open pore volume (~0.21 cm^3/cm^3) [50].

Kelly et al. [6, 68] report on thermal annealing of irradiated graphite shows that it is possible to remove the effect of the small interstitial and vacancy groups to the extent that Young's modulus is covered to the unirradiated (original) value. However the annealing does not return graphite microstructure to its original state but changes the configuration of the defects (interstitial, vacancy etc.) so that they no longer influence the physical properties of Young's modulus. Kelly et al. [69] reported the mechanical property (Young's modulus) changes for irradiated Gilsocarbon after neutron irradiation damage annealing by heat treatment. Spriggs' [46] and Knudsen's [14, 70] equations were expressed in term of changes in Young's modulus E, and it was reported as follows

$$E = E_0 e^{-3.6x} \quad \textbf{(2.5)}$$

Modulus of non-porous solid is represented with E_0, the effect of radiolytic oxidation on nuclear graphite was simulated by Brocklehurst and Adams [12], this was achieved by drilling different arrangement of holes in the graphite samples. These samples were tested to determine their mechanical properties for weight losses ranging from 0 to 50%. The effect of increasing simulated oxidation on Young's modulus was reported as:

$$E = E_0 e^{-2.7x} \quad \textbf{(2.6)}$$

The changes in the Young's modulus were lower in the drilled specimen than the Young's modulus of real radiolytic oxidised graphite by a factor of 1.3 [12, 13]. The difference between these two Equations (2.5 and 2.6) is shown in Figure 2.19

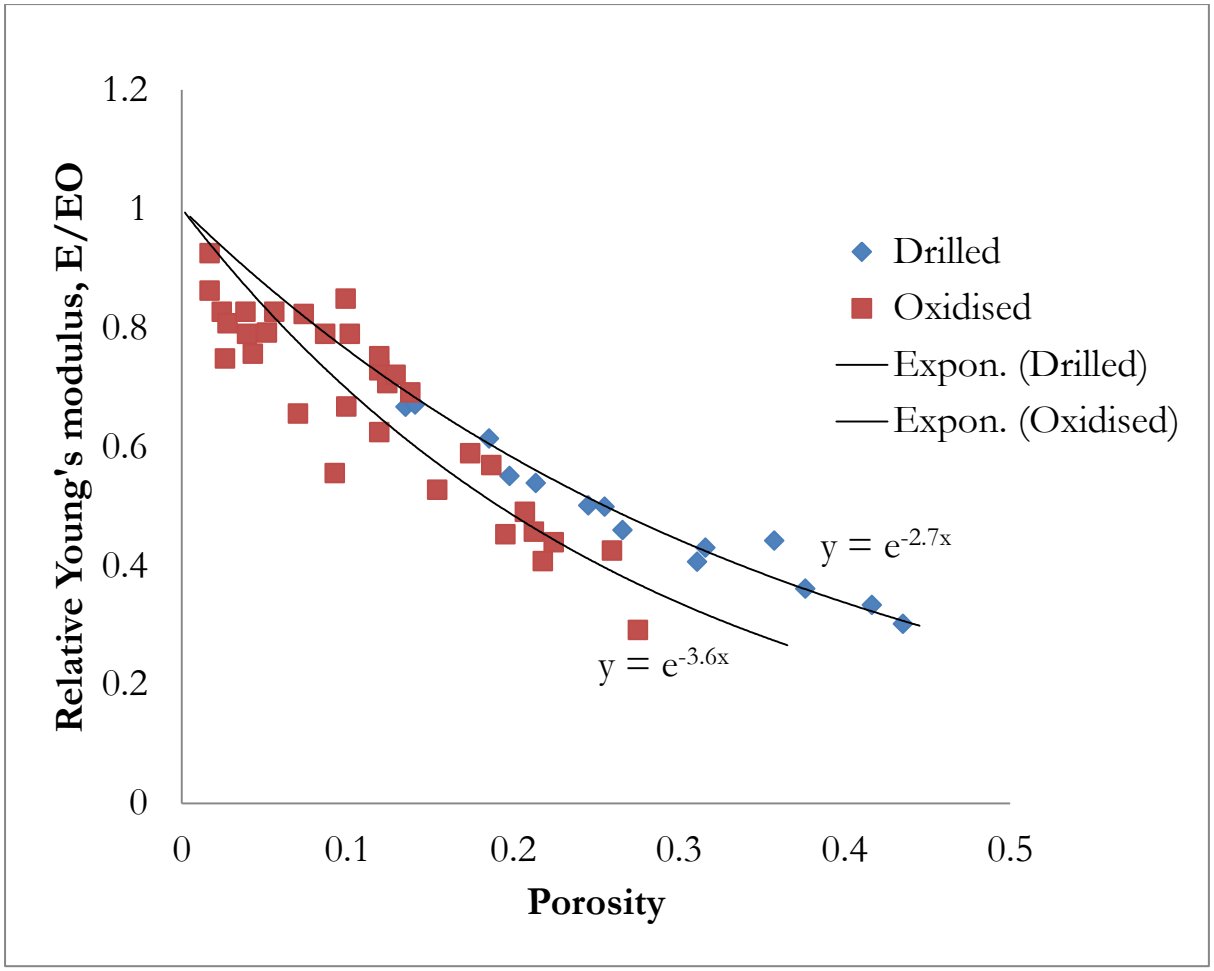

Figure 2.19 Change in Young's modulus associated with weight loss (adapted from [12, 13])

The complex physical and mechanical properties changes seen in neutron induced radiolytic oxidised graphite are not fully understood. Since the mechanism of porosity closure and formation and crystal growth have been associated with the irradiated graphite property change, these mechanistic behaviours of irradiated graphite can be simulated by deforming virgin graphite hydrostatically using a high pressure rig. Studying the changes in virgin graphite microstructure as a result of different loading modes might help to gain an understanding of complex physical and mechanical properties of irradiated graphite.

2.7 Deformation of graphite under high hydrostatic pressure

According to Seldon [42], the effect of externally applied stresses within the crystallites can lead to a combination of elastic deformation, irreversible shear and plastic deformation, internal stress relief and local stresses which can produce microcracks. The elastic and plastic deformation

effects are used to describe the stress against strain behaviour of graphite while the other effects mentioned are used to describe the stress against strain curve in different directions.

The hydrostatic deformation behaviour of nuclear graphite is in a way different to uniaxial compression. Both open and closed pores presences in graphite microstructure have different effects on the way the graphite deforms under different modes of loading (i.e. uniaxial and hydrostatic loading). In order to understand the effect of these loadings on the graphite microstructural changes, it is necessary to understand the microstructures of the polycrystalline aggregate consisting of a few particles as shown in Figure 2.20 (graphite microstructure optical image) and schematically in Figure 2.21.

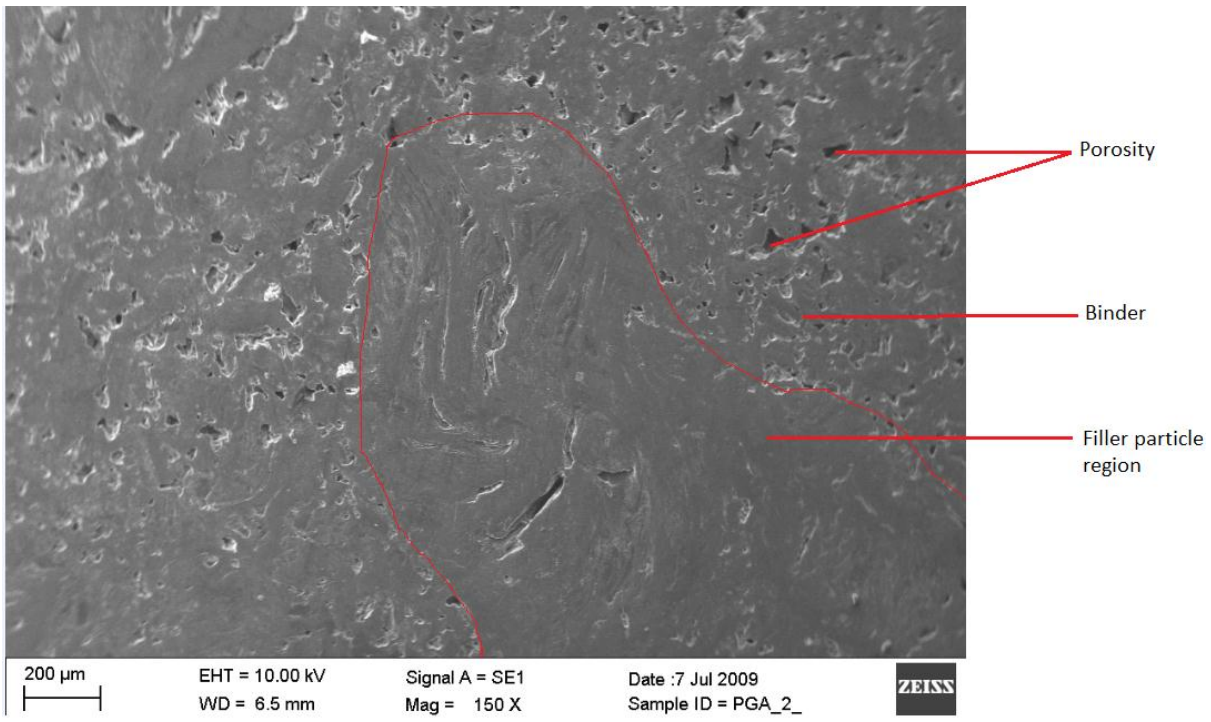

Figure 2.20 Optical image of PGA graphite

During baking, the coke particles support each other until the binder is solidified (filler particles are supported by binder matix); therefore the particles are always in close contact with each other, linked by bridges of coke binder. The shrinking binder does not provide a high density shell around each particle, hence the binder layer is full of microcracks perpendicular to the surface of the particles.

Macropores appear in between the particles and also spread throughout the binder phase. The crystallites within the coke are all nearly parallel. They are microcracks formed within the

crystallites due to differential thermal contraction and disorientation of these crystallites. It can be concluded that the coke grains are full of pores and cracks.

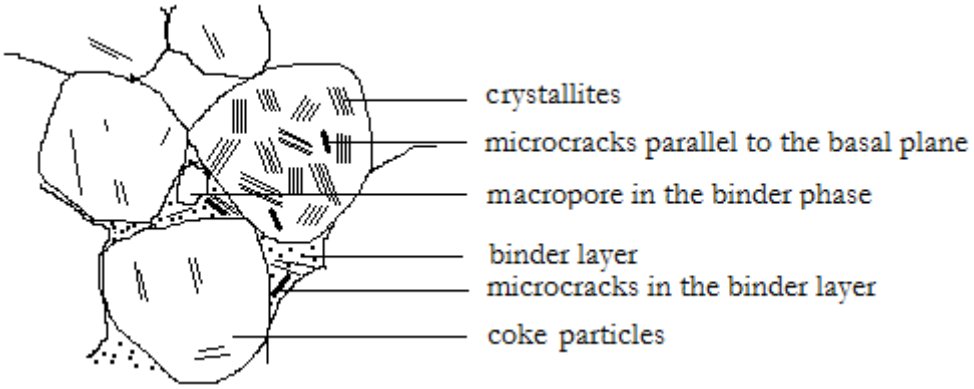

Figure 2.21 Typical detailed microstructure of graphite (adapted from [71])

Under uniaxial loading both open and closed porosity behave in the same manner, the porosity provide space for accommodating shear deformation of the coke particles, contributing to the overall deformation of the porous aggregate [42, 49]. The strain observed during uniaxial deformation should be higher than the strain observed during hydrostatic deformation due to the presence of major shearing of the coke particles into the open porosity.

Under hydrostatic loading of graphite, porosity allows crystallites to deform by shear motion of the layer planes, producing shear stresses which can induce plastic flow [49]. Individual particles are suspected to be accessible by pressure fluid, due to the existence of open pores in the binder phase as well as several cracks in the binder layer surrounding the coke particles. During compression, the coke particles compressed and shear also occurs at the same time. The confining pressure compressed the grains into each other resulting to dilatation of individual particles/grains. This is demonstrated in the Figure 2.22 by the same particles shown schematically in Figure 2.21.

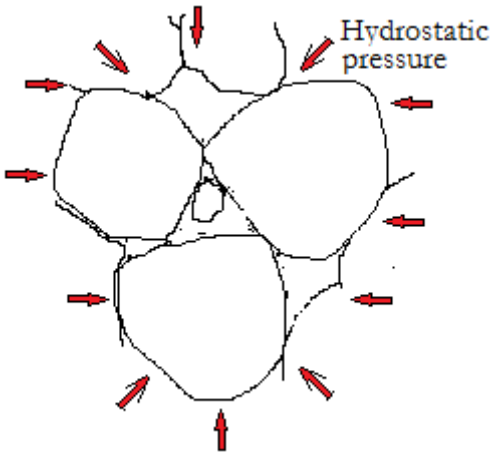

Figure 2.22 Schematic diagram of applied hydrostatic pressure

In polycrystalline graphites, the population of the mobile plane dislocations is greater than in the single crystals due to large population of twin and tilt boundaries between and within crystallites [72]. According to Boey and Bacon [49], the shear deformation of the coke particles into the surrounding pores is responsible for the apparent low value of Poisson's ratio for the polycrystalline materials. The closed pores between the particles can contribute to the hydrostatic deformation of the graphite by accommodating the internal strains in the particle.

2.8 Using theoretical models to estimate effective medium moduli

Effective medium theories have been developed in the previous work [73-77] to estimate the effective medium moduli of polycrystalline solids (i.e. rock, graphite etc.) in terms of the properties of various constituent minerals and pore fluids. To achieve this, the following must me incorporated

- The individual elastic moduli of the constituents
- The volume fractions of the constituents
- Geometric details of how the constituents are arranged

Since the geometric details of the constituents of a polycrystalline solid are quite challenging to measure, boundary methods have been adapted to estimate the effective moduli of the polycrystalline solid by estimating the upper and lower bounds on the moduli. The bounds models are one of the types of theoretical models that are relatively free of assumptions about the material microstructure and give rigorous upper and lower limits on the moduli, given the composition. The theoretical models used in this work are Voigt-Reuss-Hill bounds (VRH), Hashin-Shtrikman bounds (HS), and Kuster and Toksoz models (KT).

2.8.1 Voigt-Reuss-Hill bounds (VRH)

The Voigt and Reuss averages are interpreted as the ratio of average stress and average strain within composites [74]. The upper bound (Voigt) and lower bound (Reuss) are found assuming that there are uniformity in strain and stress respectively throughout the whole composite. The Voigt upper bound and Reuss lower bound of the effective elastic, modulus, *Mv*, of *N* phases are

$$M_V = \sum_{i=1}^{N} f_i M_i = (1 - \emptyset)K_s + \emptyset K_{air} \quad (2.7)$$

$$M_R = \sum_{i=1}^{N} \frac{f_i}{M_i} = \frac{(1 - \emptyset)}{K_s} + \frac{\emptyset}{K_{air}} \quad (2.8)$$

Where f_i is the volume fraction of the ith phase,

M_i is the elastic modulus of the ith phase and

M_v and M_R are the effective elastic modulus of Voigt and Reuss bounds respectively

$\emptyset$ represents fraction

K_s and K_{air} are the bulk modulus of solid and air (void)

The Voigt-Reuss-Hill average is the average of Voigt upper bound and the Reuss lower bound as shown in Equation 2.9

$$M_{VRH} = \frac{M_V + M_R}{2} \quad (2.9)$$

This method assumes that each constituent is isotropic, linear, and elastic. It is commonly used in estimating rock elastic properties.

2.8.2 Hashin-Shtrikman bounds

The Voigt-Reuss bounds are wider than Hashin-Shtrikman (HS) bounds. This bound is the narrowest possible bound on moduli that can be estimated for an isotropic material, knowing the volume fractions of the constituents. When there are only two constituents, the bounds are written as;

$$K^{HS\pm} = K_1 + \frac{f_2}{(K_2 - K_1)^{-1} + f_1\left(K_1 + \frac{4}{3}\mu_1\right)^{-1}} \quad (2.10)$$

$$\mu^{HS\pm} = \mu_1 + \frac{f_2}{(\mu_2 - \mu_1)^{-1} + \frac{2f_1(K_1 + 2\mu_1)}{5\mu_1\left(K_1 + \frac{4}{3}\mu_1\right)}} \qquad (2.11)$$

Where K_1 and K_2 are the bulk moduli of individual phases; μ_1 and μ_2 are the shear moduli of individual phases; and f_1 and f_2 are the volume fractions of individual phases. The upper (HS+) and lower (HS-) bounds are computed by interchanging which material is termed 1 and which is termed 2. When the stiffest material is termed 1, the expressions yield the upper bound and the lower bound when the softest material is termed 1. Like the VRH model, this method also assumes that each consistent is isotropic, linear, and elastic. It is used in estimating rock elastic properties.

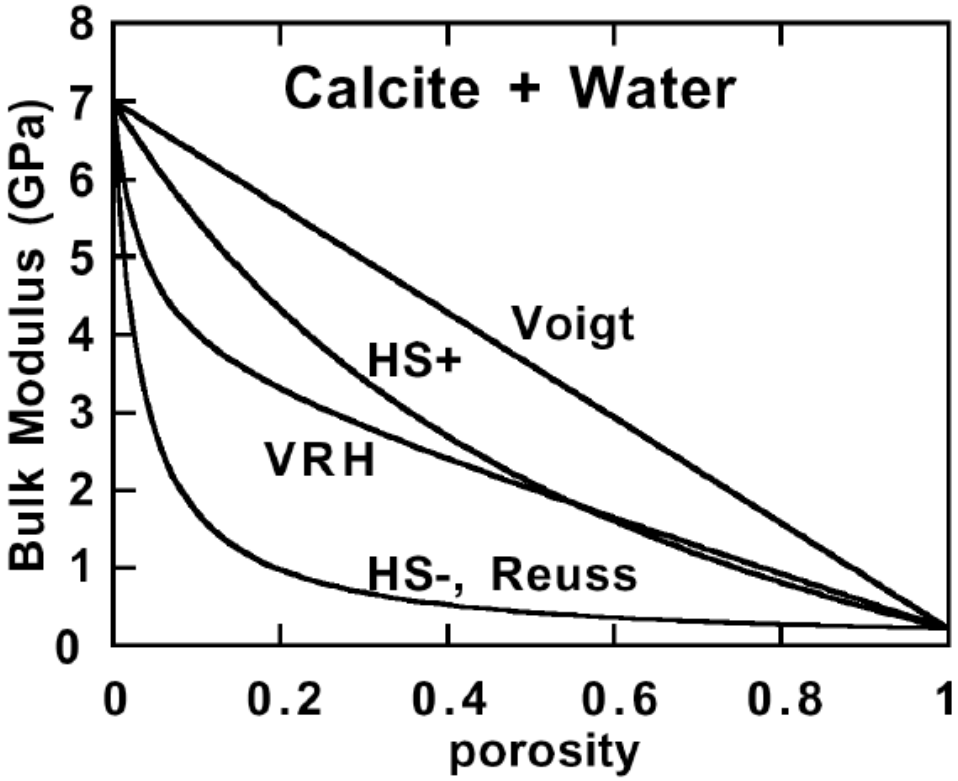

Figure 2.23 Bulk modulus curves for Calcite rock with water using effective medium theories (adapted from[78])

Distance between upper and lower bounds depends on difference between the end member constituents. Bulk moduli of Calcite and water are 7 GPa and 2.2 GPa respectively as shown in the Figure 2.23, the mixture of Calcite and water gives widely spaced bounds. The HS- and Reuss bounds are identical. The Voigt bound is more stiff than other bounds.

2.8.3 Kuster and Toksoz models (KT)

Kuster and Toksoz [73] derived expressions for P- and S-wave velocities by using a long-wavelength first-order scattering theory. Their formulation can be used to calculate effective moduli for randomly distributed inclusions [73, 77]. A generalization of the expressions for the effective bulk moduli and shear moduli can be written as

$$(K_{KT}^{*} - K_m)\,\frac{\left(K_m + \frac{4}{3}\mu_m\right)}{\left(K_{KT}^{*} + \frac{4}{3}\mu_m\right)} = \sum_{i=1}^{N} X_i\,(K_i - K_m)P^{mi} \qquad \textbf{(2.12)}$$

$$(\mu_{KT}^{*} - \mu_m)\,\frac{(\mu_m + \zeta_m)}{(\mu_{KT}^{*} + \zeta_m)} = \sum_{i=1}^{N} X_i\,(\mu_i - \mu_m)Q^{mi} \qquad \textbf{(2.13)}$$

$$\zeta = \frac{\mu}{6}\left(\frac{9K + 8\mu}{K + 2\mu}\right) \qquad \textbf{(2.14)}$$

Where the K_{KT}^{*}, μ_{KT}^{*} are the effective bulk and shear moduli respectively for a variety of inclusion shapes. The coefficients P^{mi} and Q^{mi} describe the effect of an inclusion of material, *i* in a background medium, *m*, while X_i is the volume concentration of the inclusion, ζ is the fraction of effective bulk and shear moduli. Inclusion shapes include spheres, needles, disks and penny cracks.

According to previous work [74], for spherical inclusions, the KT expression for bulk modulus are identical to the HS upper bound, even though the KT expressions are formally limited to low porosity. KT formulation assume

- isotropic, linear, and elastic media;
- limitation due to dilute concentrations of the inclusions; and
- idealized ellipsoidal inclusion shapes.

Since Gilsocarbon is near-isotropic graphite, it was suggested that these theoretical models (VRH, HS+, HS-, and KT) can be used to validate the experimental results (behaviour of Gilsocarbon under hydrostatic pressure) by comparing the effect of porosity on effective bulk moduli. The comparison between experimental curves and the theoretical models is discussed further in Chapter 5.

2.9 Conclusion

The deformation behaviour of polycrystalline graphite differs from that of a single crystal on a macroscopic scale due to the existence of pores and cracks in the graphite microstructure, which effectively reduce the load carrying area of the porous material.

The effect of non-hyhydrostatic deformation on the mechanical and physical properties of polycrystalline graphite materials has been widely studied in past work [42, 53, 79, 80]. According to Seldin [42], the experimental study of uniaxial stress-strain relationships is non-linear in both tension and compression. Under uniaxial loading, polycrystalline graphite deviates from Hooke's law, cyclic loading results in hysteresis loops and residual strain even at smaller applied stresses [53, 79]. A more detailed study of the effect of triaxial stress on Young's modulus of graphite has also been studied by Yoda el al. [56, 81], but little effort has been directed to the understanding of the microstructural changes of graphite during hydrostatic loading.

The hydrostatic deformation behaviour of graphite microstructure (both unirradiated and irradiated) under gas pressure up to 4.14 MPa was investigated Boey and Bacon [49]. Large hysteresis loop, non-linear pressure strain relationship and reduction in strain were observed in irradiated graphite compared to unirradiated graphite [49]. Brocklehurst and Kelly [82] studied the uniaxial dimensional change in graphite under fast neutron irradiation and he suggested that the decrease in the residual strain of irradiated specimen might be primarily due to the decrease in the amount of basal slip in the deformation process within the specimen after irradiation.

The effect of closed porosity on hydrostatic deformation of graphite was investigated by Boey and Bacon [49], who observed reduction in bulk modulus of graphite under fluid pressure, due to restriction in open porosity deformation resulting to shrinkage in closed micropores. Boey and Bacon [49] worked at a lower pressure compared with the pressure used in this work. Paterson and Edmond [54] and Yoda et al. [56, 81] studied the deformation of graphite at high pressure, and it was suggested that the compression stress-strain curve of polycrystalline graphite depends on confining pressure between 100- 600 MPa. There is a large volume recovery during the release of confining pressure. Samples recover almost their initial volume below 50 MPa [54]. Paterson and Edmond [54] suggested that the deformation is due to sliding of granular particles against the resistance of microscopic friction, deformation may also accompanied by flexure of platelets which could also introduces the internal stresses responsible for recovery effects [54]. But there was not enough evidence to support these suggestions by Paterson and Edmond [54].

The hydrostatic deformation of nuclear graphite is caused by the crystallite and their interaction with each other and with the microporosity present in the particle. The presence of micropores in the coke particles has the effect of reducing the restraint on the plastic flow on one crystallite which might be exerted by neighboring crystallites of different orientation. The presence of the macropores in the binder phase provides free surface to accommodate the deformation of individual coke particles

The effect of irradiation on nuclear graphite has been associated with mechanisms such as crystallite swelling, formation and closure of porosity, pinning and tightening of the graphite crystallite. Similar effects have been noticed in the previous work on hydrostatic deformation of graphite, but the relationship between the graphite elastic properties changes due to hydrostatic deformation and study of the irradiated effects has not been compared in the past.

CHAPTER 3

3 Materials and Methods

All experimental work described herein was completed in the Experimental Rock Deformation Laboratory in the school of Earth, Atmosphere and Environmental Sciences of the University of Manchester. This chapter describes the materials, experimental equipment and methods used in this work. The pressure vessels such as large capacity room temperature rig (big rig) and seismic velocity rig were used to perform high pressure tests on nuclear graphite, and all strains (axial, circumferential and volumetric) were measured using post yield strain gauges. Hydrostatic tests and axial deformation tests were conducted using the big rig while the hydrostatic and ultrasonic measurements were conducted in the seismic velocity rig.

3.1 Materials

The Pile Grade A (PGA) and Gilsocarbon nuclear graphites were used in this work. The Gilsocarbon specimens were isotropic in nature and were designated A2, E1-E4 and I1-I11 while the PGA specimens were anisotropic in nature and were designated B2, B4, F1-F7 and J1-J25 as shown in the Table 3.4. The experiments performed with each sample and their elastic property changes before and after deformation will be discussed further in the Chapter 4. The properties of these nuclear graphites are shown in Table 3.1

Table 3.1 Properties of PGA and Gilsocarbon nuclear graphites as reported by [83, 84]

Graphite	Manufacturer	Coke type	Forming process	Grain or cell size	Density (g/cm^3)
PGA	Anglo- Great Lakes Limited	Petroleum coke graphite anisotropic	Extrusion	1 mm (Max.)	1.74
Gilsocarbon	Manufactured by BAEL, UCAR (formerly BAEL), and AGL.	Gilsonite coke graphite Near Isotropic	Moulding	0.5-1 mm (Max.)	1.8

When polycrystalline graphite is manufactured either by extrusion, moulding or iso-moulding there is always some degree of preferred orientation. PGA Graphite, as an extruded material based on "needle" shaped coke, displays substantial anisotropy along the grain/extrusion direction ("with grain" or WG) compared to across that orientation ("against grain" or AG) [20, 85]. The WG and AG definitions of direction are commonly used in the nuclear graphite

community to define the anisotropy of properties such as strength and stiffness. Apart from the inherent anisotropy of graphite, grain sizes, porosity distributions have an effect. These features can contribute considerably to the apparent differences in the material properties measured in different directions [85]. Both extruded and moulded polycrystalline graphites are transversely isotropic. The preferred orientation of the crystals in each figure with a sketch (0001) pole figure is shown in the Figure 3.1

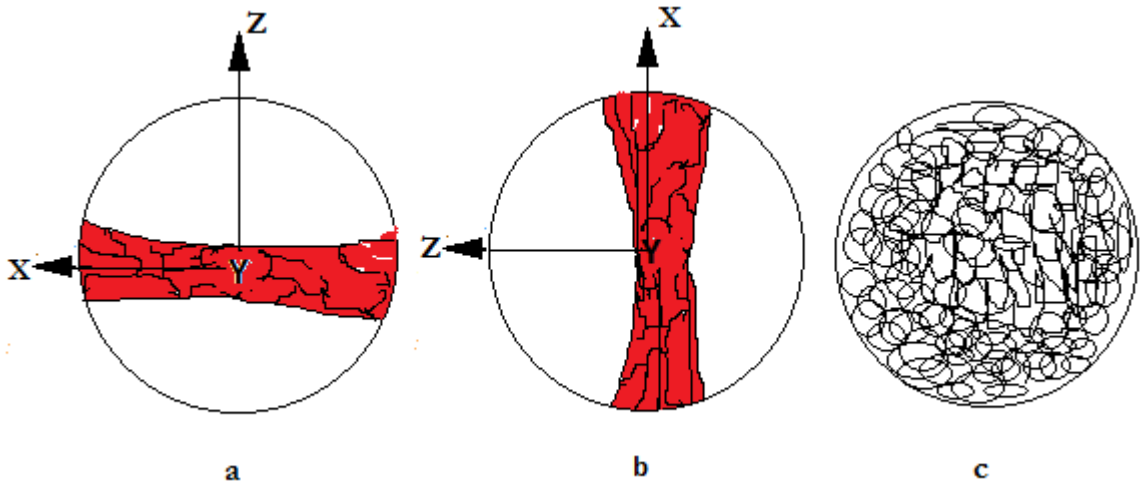

Figure 3.1 Schematics showing poles to the basal plane in extruded graphite a) in which the preferentially alignment of the grains is parallel to the extrusion direction X, b) in which the preferentially alignment of the grains is parallel to the extrusion direction X, c) Moulded Gilsocarbon, with no preferred orientation

PGA graphite brick were produced by an extrusion process, which tends to align the needle-like crystallites with their basal planes parallel to the extrusion direction. PGA specimens were machined from PGA graphite brick in the form of preferred orientated cylindrical shape (AG and WG), this is illustrated in Figure 3.2. Gilsocarbon samples were machined randomly from the Gilsocarbon brick, because the author assumed there is less significant degree of orientation in a particular direction due to moulding forming process.

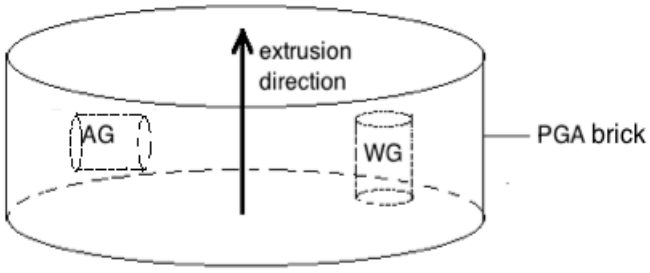

Figure 3.2 Schematic of the orientation of specimens taken from the PGA graphite brick

The directional dependence is a result of the geometry of the filler particles used and the manufacturing process. All graphites have been developed with anisotropic or near isotropic material properties [20, 29, 30, 86]. Both PGA and Gilsocarbon have a maximum grain size of (~1 mm) as shown in Table 3.1

3.2 X- ray Techniques

In order to predict microstructural damage of the graphite grades (PGA and Gilsocarbon), it is necessary fully to understand the microstructure and the effect of high pressure on the microstructure of graphite. Two different X-ray techniques have been used technique to probe the microstructure of the samples

- X- ray Tomography was focused on obtaining high resolution micrograph slices of the porosity structure of both graphites. Post-processing of these data was performed using the Avizo© (3D visualization software).
- The graphite texture and bulk crystallinity was characterized using X-ray texture goniometry and X-ray diffraction (XRD).

The type and distribution of porosity contained in graphite microstructures was characterised using X-ray tomography (a non- destructive technique) and analysed using Matlab and Aviso©. Using this technique the average pore size before and after deformation was measured to ascertain if there were any pore size differences caused by the deformation. Lastly, the microstructure was characterised by observing the graphite crystalline orientation, XRD texture (pole figure, orientation distribution function) was analysed using the Matlab toolbox for quantitative texture analysis called Mtex [87].

3.2.1 X-ray tomography

X- ray tomography equipment is similar to that of medical CT (medical computed tomography). It is a technique used to obtain a 3D images and measurements of microstructural features inside a specimen. X-ray tomography was used to characterise the pore microstructure of virgin PGA

and Gilsocarbon nuclear graphites before and after loading. This is a non-destructive technique for examining the three dimensional (3D) microstructure of a material. It is very sensitive to composition and density [11]. Three-dimensional images can be obtained at different resolutions. The graphite micrograph slices obtained from X-ray tomography have several black features (region with no X-rays absorption) distributed through out the 3D image; these features are graphite pores, while the grey features (region which diffract and absorb X-rays) are the graphite. After image acquisition with x-ray tomography, Avizo© was used to reconstruct and analyse the pore distribution and porosity volume in the graphite micrograph. Porosity was analysed in order to quantify graphite microstructural changes before and after deformation.

The sample is illustrated with a divergent X-ray beam and the transmitted X-rays were recorded by a charge-coupled device (CCD) at a number of angles of rotation of the specimen (usually over a range of either 180º or 360º) about a central axis (Figure 3.3).

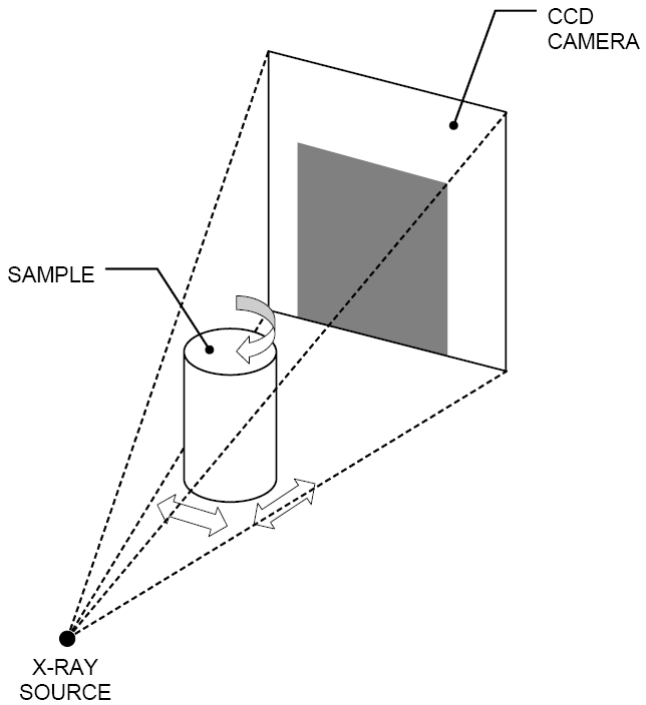

Figure 3.3 Schematic of the X- ray micro- tomography device adapted from Hall et al. [11]

The integrated absorption coefficient (μ) of a material is the ratio of transmitted to incident photons is a function of the density and atomic number of the material [11, 88, 89]. A series of two-dimensional images (projections of the volume) are obtained, from which it is possible to

reconstruct a complete 3D image of the X-ray absorption. The quality of the image mainly depends on the settings i.e. power and intensity of the beam.

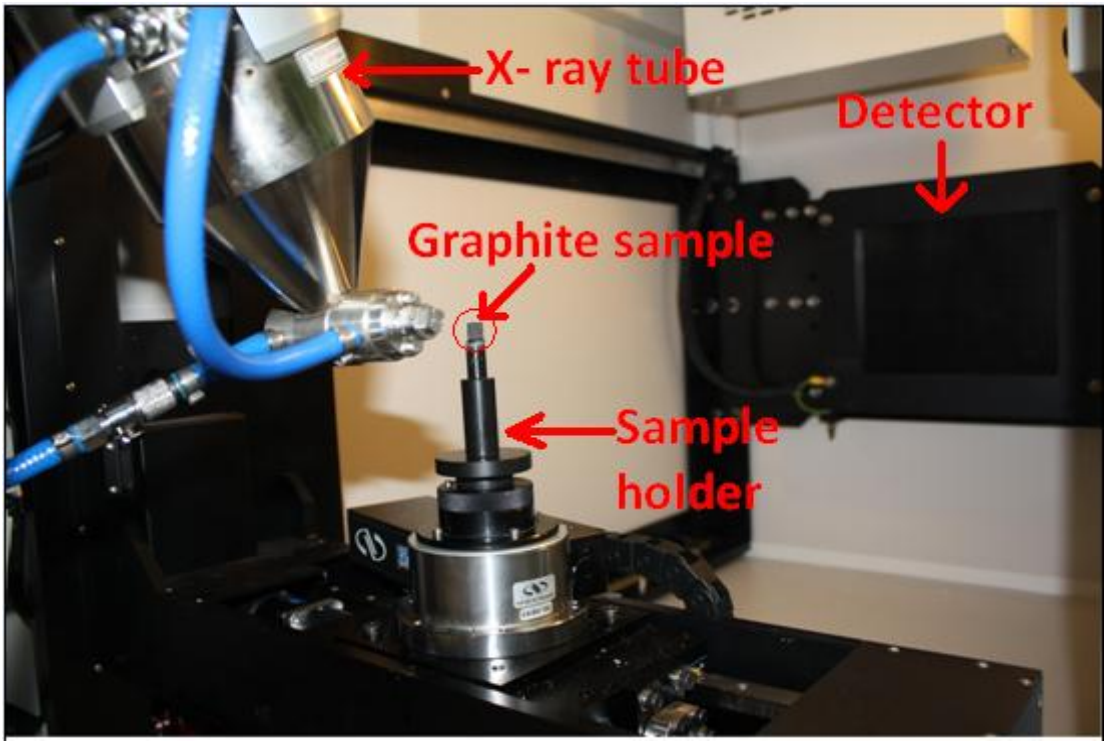

Figure 3.4 X-ray micro- tomography system used (X-Tek HMS- 320kV)

The microstructures of PGA and Gilsocarbon were observed by using a X- Tek HMS- 320kV X-ray tomography machine as shown in Figure 3.4. The experiment requires an X-ray source, a rotating sample holder and a detector (Figure 3.4). Auto-conditioning at 70 kV and 110 μA was performed to expel gas from X-ray tube that might have built up. The equipment X-ray beam was filtered with copper (0.25 mm), this filtering process removes low energy radiation, and reduces the beam hardening (beam hardening is when the outcoming beam contains a high proportion of high-energy or hard X-rays) and to avoiding artifacts [90]. The scan settings are shown in Table 3.2.

Table 3.2 X- ray Tomography scan settings

Voltage (kV)	55
Intensity (μA)	200
Time of exposure (fps)	1.4
Scan range (°)	0 – 180
Angle per step (°)	0.88
Scan duration (s)	2045

The sample is rotated by motorised turntable while scanning. The typical resolution accessible by this equipment is 11.3- 14.6 μm per voxel

One thousand eight hundred radiographs of the sample were taken during each scan. The VG studio package was used to reconstruct the volume of high-resolution images obtained. The sample height used varied from 40 - 50.8 mm. Three-dimensional images of virgin PGA and Gilsocarbon comprised 1900 x 1900 x 1800 voxels. A voxel is a volume element representing a value in 3D space, and it can be coded in 8, 16 and 32 bits, but in this work it was coded in 8bits with a grey scale of 0 - 256 (2^8 values). The high-resolution images obtained from this equipment allow the characterisation of graphite microstructure such as porosity morphology.

3.2.2 X-ray texture goniometry

The preferential crystal orientation in the PGA and Gilsocarbon nuclear graphite prepared by extrusion and moulding respectively were investigated. Young's modulus of a polycrystalline aggregate without porosity was calculated from the orientation distribution function (ODF). A quantitative description of orientation characteristics gave a good interpretation of texture in a given sample. The term 'texture' is a collective term for a non-uniform distribution of crystallographic orientations in a polycrystalline aggregate or is a synonym for preferred crystallographic orientation in the polycrystalline material [91]. Texture analysis is the determination of the preferred orientation of the crystallites in polycrystalline aggregates. It is not possible to measure directly the distribution of crystal orientations in a polycrystalline sample by bulk diffraction techniques. Texture goniometry is only capable of determining the distribution of crystal poles and further analysis is required to extract the orientation distribution from these data. The preferred orientation is usually described in terms of pole figures [91, 92].

X- ray diffraction is a non-destructive analytical technique used for identification and qualitative determination of the various crystalline forms or phases in a material. X-rays are generated by a cathode ray tube, filtered to produce monochromatic radiation, collimated to concentrate, and directed toward the graphite sample [25, 93]. The interaction of the incident rays with lattice planes within the sample produces constructive interference and a diffracted ray when conditions satisfy Bragg's law;

$$n\lambda = 2d\sin\theta \quad (3.1)$$

This law relates the wavelength (λ) of electromagnetic radiation to the diffraction angle and the lattice spacing (d) of the lattice plane that is causing the diffraction, n and θ are integer and incident angle [93]. These diffracted X-rays are then detected and counted. By changing the geometry of the incident rays, all possible diffraction conditions for each grain were explored. In this work, Phillips X'pert 1 goniometry was used to scan the graphite samples.

Table 3.3 XRD scan settings

Angles	Phi (Φ)	Psi (ψ)
Scan range (°)	0 -360	0-85
Step size (°)	0.05	0.05
Time/step (s)	10	10
Scan duration (s)	72000	17000

Texture goniometry measures the intensity of the diffracted X-rays for a specific 2θ (e.g. for a specific lattice plane) over a whole range of sample orientations. The sample orientation is usually expressed in terms of 2 Euler angles phi (Φ) and psi (ψ). This data is then density controlled and represented on a stereographic projection of a hemisphere (often called pole figures) here different points on the hemisphere represent different orientations of the sample.

A texture scan used, three peaks ([002], [100], and [110] planes) selected randomly amongst the other peaks for texture measurement, the scan settings are shown in Table 3. A texture measurement is also referred to as a pole figure. In Figure 3.5, considering the plane (h, k, l) in a given crystallite in a sample, the direction of the plane normal is projected onto the sphere around the crystallite. The point where the plane normal intersects the sphere is defined by two angles, a pole distance ($\psi = 85^{o}$) and an azimuth ($\Phi = 360^{o}$). Occasionally α and β are used to represent the pole distance and azimuth angles respectively. The azimuth angle is measured counter clockwise from the point E (East). The intensity of a given reflection (h, k , l) is proportional to the number of h, k, l planes in diffraction condition (Bragg's law). Hence, the pole figure gives the probability of finding a given crystal-plane-normal as function of the specimen orientation. If the crystallites in the sample have a uniform distribution of orientations recorded then intensity will be uniform [94]. Assuming that the plane normal for the plane (h, k, l) are projected from all the crystallites irradiated in the sample onto the sphere, each plane normal intercepting the sphere represents a point (X) on the sphere.

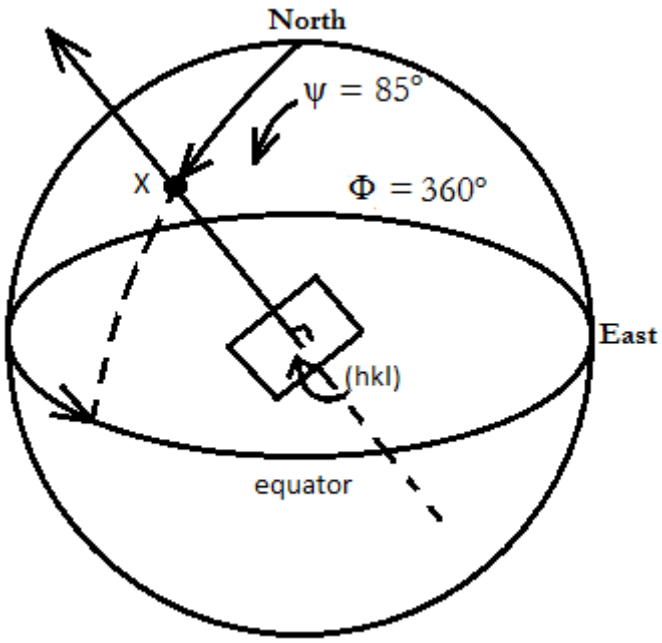

Figure 3.5 Schematic diagram of stereographic projection (sample orientation is usually expressed in terms of 2 Euler angles phi (Φ) and psi (ψ))

3.2.3 Pole figure

A pole figure is a projection of directions on to a plane. It is described when intensity distribution gained from the measurement of a lattice reflection with indices (*h, k, l*) where the sample is rotated around two axes (angles ψ and Φ) is drawn into a polar grid using contours lines [91]. The diffracted intensity is proportional to the fraction of crystallites within the tested volume oriented in a specific direction. Three angles are required to define the orientation of a crystallite in relation to the sample axes, a set of Euler angles ($\varphi_1, \Phi, \varphi_2$) are commonly used for the consecutive rotations around the z-axis, x-axis, and again z-axis [95]. The texture of a tested sample can be also described completely by the orientation distribution function with the orientation, $g(\varphi_1, \Phi, \varphi_2)$, this is described later in this chapter. A representation of the crystal orientation with respect to a unique sample orientation is called an inverse pole figure. Any sample orientation with respect to an external reference frame has its own inverse pole figure.

3.2.4 Intensity corrections and data reduction

A Complete pole figure cannot be measured by laboratory X-ray diffraction due to the strong defocusing effect and diffraction geometry, therefore the obtained intensity need to be corrected. Background corrections and defocusing measurements were performed, by removing the background and correcting for the beam defocusing that occurs as the ψ angle increases. As a result more accurate pole figures are produced [94]. Background intensity results from

incoherent scattering and fluorescence in the sample, from interaction of the beam with air molecules, and from electronic noise. Air scattering can be reduced by setting the incoming beam collimator and a receiving collimator close to the sample or by measuring in a vacuum. Background can also be reduced by choosing a small window for the pulse height analyser, because most of the background x-ray photons have a different wavelength. In practise one cannot eliminate the background, but the background intensity can be subtracted from the measured intensity [91]. The background correction curve is best determined empirically on a sample with similar composition but few diffraction peaks by placing the detector on a background region removed from any Bragg peak. The first step in data correction is to subtract the background from the intensity curve.

If $I^{bg}_{\alpha=0^o}$ is measured background at $\alpha = 0^o$ then the background I^{bg}_{α} at α is

$$I^{bg}_{\alpha} = I^{bg}_{\alpha=0^o} \frac{I^{bg(stand)}_{\alpha}}{I^{bg(stand)}_{\alpha=0^o}} \qquad \textbf{(3.2)}$$

The ratio as shown in the Equation 3.3 is the empirically determined background correction curve

$$r = \frac{I^{bg(stand)}_{\alpha}}{I^{bg(stand)}_{\alpha=0^o}} \qquad \textbf{(3.3)}$$

The shape of the irradiated area depends on the collimating system and the orientation of the sample surface relative to the incident x-ray beam. Since the x-rays penetrate the sample up to about 100- 200μm, the covered volume is larger and the true geometry is more complicated. The spread in area and the resulting distortion of the reflected signal causes defocusing x-rays. X-ray texture measurements usually record peak intensities rather than integrated intensities, the intensity decrease with tilt is severe, and therefore it is necessary to correct the intensity.

An empirical defocusing correction curve can be measured on a sample of the same material or a material with similar 2θ peak positions and the same sample geometry but with no preferred orientation. In this case, a Gilsocarbon sample was used for the defocusing scan to correct all the other texture scans; because it was assumed that Gilsocarbon has no preferred orientation. The correction depends on the alignment of the instrument, the shape and size of collimator and receiving slit, and the diffraction angle 2θ. A corrected intensity I^{corr}_{α} is obtained from;

$$I_{\alpha}^{corr} = I_{\alpha} \frac{I_{\alpha=0^o}^{rand}}{I_{\alpha}^{rand}} \quad \textbf{(3.4)}$$

Where $I_{\alpha}$is the measured intensity from the texture sample, and $I_{\alpha}^{rand}$is the intensity from the random sample at the same value of α, all these intensities must be corrected for background.

The correction curves obtained from Gilsocarbon (uniform orientation sample) were used as standard and applied to correct PGA samples. It was necessary to ascertain the uniformity of texture of the standard by measuring a pole figure and applying empirical corrections. This should produce a uniform distribution. The result from the standard sample is shown in chapter 4.

In this work, the pole figure was scanned from the center ($\psi = 0^0$), out to about $\psi = 85^0$ using Philips X'pert 1 goniometer (Figure 3.6).

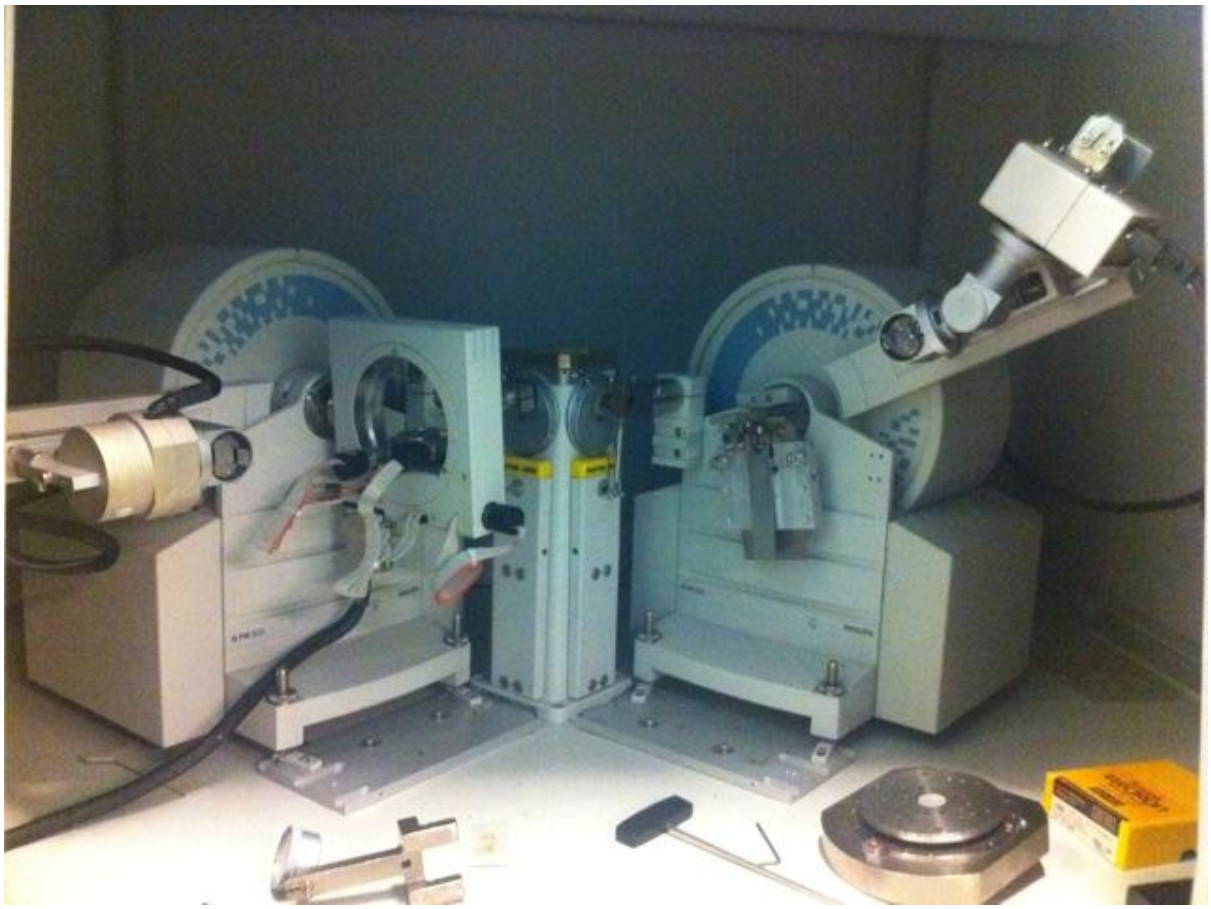

Figure 3.6 Philips X'pert 1 goniometer

It allows automatic scanning of the pole figure on a true spiral by changing Φ and ψ simultaneously and continuously [96]. By collecting pole figure data for several (h k l), the

complete orientation distribution function (ODF) of the material can be determined. This was achieved using Mtex (Matlab toolbox) [97]. MTex is an open- source Matlab toolbox for texture analysis and modelling [98]. It comprises functions to import, analyse and visualize diffraction pole figure data, to estimate an ODF, and compute texture characteristics.

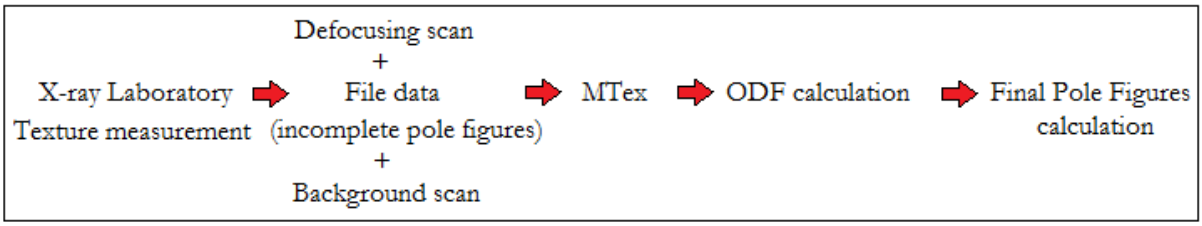

Figure 3.7 Texture analysis procedure (data regeneration)

The texture analysis procedure shown in the Figure 3.7 and it is summarised as follows

- The pole figure data including the background and defocussing data were collected for the following lattice planes [002], [100], and [110], and were imported in the command window of Matlab
- The graphite is Hexagonal with the following lattice spacings (a= 2.465 Å, c= 6.753 Å, and angles; $\alpha = 90^0$, $\beta = 90^0$, $\gamma = 120^0$ and is in the 6/mm Laue group.
- The script (m-file) was generated and worked with in other to visualize and to represent the pole figures.

3.2.5 Orientation Distribution Function (ODF)

Preferred orientation of the crystalline regions in polycrystalline samples may be investigated by X-ray diffraction. The information concerning the preferred orientation of each Bragg plane obtained can be examined [99]. These data may be summarised concisely by a series of pole figure diagrams. A collection of pole figure diagrams for a sample implicitly contains general and useful information called the distribution of orientations of the crystallographic unit cell. Mathematical procedures have been developed for deducing this information in the form of crystallite orientation distribution [95, 100-102]. Once the crystallite orientation distribution function has been determined, it may be used to compute pole figures for unmeasured planes. The crystallite Orientation Distribution Function (ODF) offers the most complete representation which can be gained from a given set of pole figure data [95]. Bunge [95] and Kocks et al. [91] defined ODF ($f(g)$) as

$$f(g) = \frac{dV(g)}{Vdg} \qquad (3.5)$$

The volume of all crystallites in a sample is denoted by dV, it contains an orientation g within an orientation region dg, g may be specified in a numerous ways (i.e. Euler angles $\varphi_1, \Phi, \varphi_2$). V is the total sample volume. The volume fraction of orientations within a certain region x of orientation space is then

$$V_f(g) = \frac{dV(g)}{V} = \frac{\int_{dx} f(g)dg}{\int_x f(g)dg} \quad \textbf{(3.6)}$$

Where x denotes the entire orientation space and dx denotes the region around the texture component of interest. In common practice, uniform density, $f(g)$ is normally set to 1. This is often called orientation density in multiples of a uniform distribution (m.u.d.). When the orientations are represented by Euler angles, the infinitesimal volume element is

$$dg = dA\boldsymbol{d\phi} \quad \textbf{(3.7)}$$

$$dg = sin\boldsymbol{\Theta}\ \boldsymbol{d\Theta}\ \boldsymbol{d\Psi}\ \boldsymbol{d\phi} \quad \textbf{(3.8)}$$

Where $\boldsymbol{\Theta}$, is the pole distance and Ψ is the Euler angle (azimuth in pole figure) and $\boldsymbol{\phi}$ represent the tilt angle in goniometer, dA is area element, whose magnitude depends on declination, these are shown in the Figure 3.8. The volume of element is corrected by $\boldsymbol{sin\Theta}$.

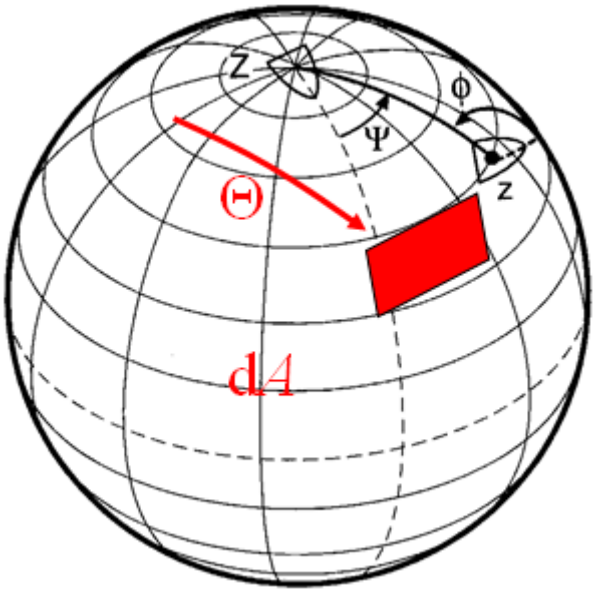

Figure 3.8 Symmetric definition of Euler angles as spherical coordinates for a vector on the surface of a unit sphere (adapted from [91])

3.3 Porosity measurement

Helium pycnometry was used to measure the percentage of connected pores (effective porosity) of each sample before and after deformation, while mercury porosimetery was used to measure the porosity volume, size and distribution of deformed and undeformed samples. The porosity distribution in each sample was compared with each other to gain more understanding of the effect of high pressure on porosity and the pore size distribution.

3.3.1 Helium pycnometer

The helium pycnometer was invented by Edward Y.H. Keng in 1967 [103]. It is a non-destructive instrument that allows the measurement of the volume and hence true density of solid sample. This is achieved by employing Boyle's law to determine the true sample volume. Boyle's law is employed with helium as the gas to determine the solid volume of a sample. The technique is rapid, and is valid on clean and dry samples. As the size of helium molecule is very small, it can the penetrates even the smallest open pores. In this work, the DHP-100 Digital Helium Porosimeter (Figure 3.9) was used to calculate the effective porosity percentage in each graphite sample before and after loading. The results are discussed in Chapter 4.

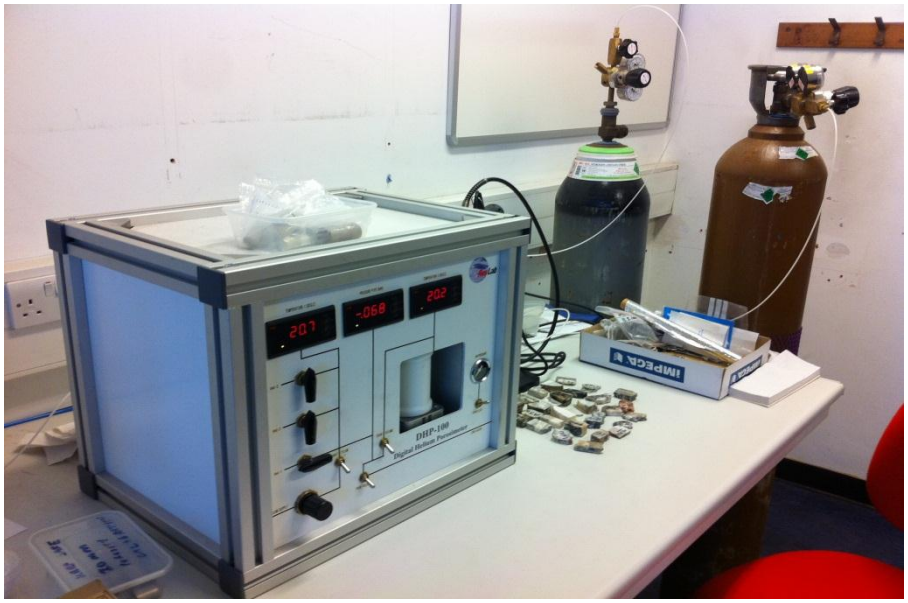

Figure 3.9 Helium Porosimeter

The effective porosity of the sample was calculated by applying the following procedure; the Boyle's law states that for an ideal gas, the pressure exerted by a gas held at a constant temperature varies inversely with the volume of the gas.

$$PV = nRT \tag{3.9}$$

Where R is the universal gas constant, P is the pressure of the system; V is the volume of the gas, n is the number of moles and T is the temperature. The helium gas in the reference cell isothermally expands into a sample cell. Thus the pressure-volume products are equal before and after opening the core holder valve.

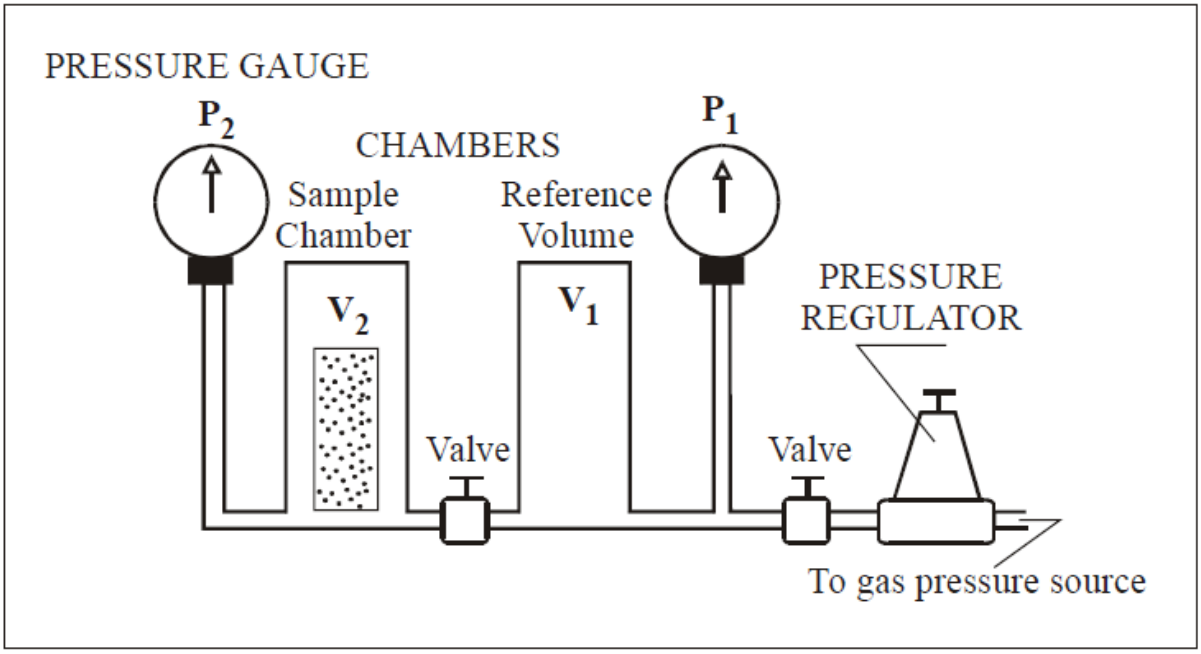

Figure 3.10 Schematic diagram of helium porosimeter apparatus adapted from [104]

$$P_1 V_1 = P_2 V_2 \tag{3.10}$$

After expansion, the resultant equilibrium pressure is measured. The helium porosimeter apparatus is shown schematically in the Figure 3.10.

Calculating grain volume requires the knowledge of P_1, P_2, V_1, V_c (reference pressure, gauge pressure reading, reference volume and sample chamber volume). The gauge pressure reading was obtained when the helium expands into the specimen chamber and it was assumed that temperature (≈ 20 ^{O}C) is constant. The $P_1 \approx$ 7 bar, reading was taking to 0.001 bar. In solving the equation of unknown volume, V_2,;

$$V_2 = V_1 + V_c - V_g \tag{3.11}$$

Since the product of the initial pressure and volume of the helium in the system is equal to the final pressure and volume of the helium in the system. Therefore, if a sample of unknown volume is placed in the core holder, its grain volume can be calculated by rearranging Equation (3.12)

$$\varphi = \frac{V_b - V_g}{V_b} \tag{3.12}$$

$$V_g = V_1 + V_c - \frac{P_1}{P_2} V_1 \tag{3.13}$$

Theoretical bulk volume (V_b) is calculated by using the equation of the volume of cylinder

$$V_b = \pi r^2 h \quad \textbf{(3.14)}$$

The effective porosity is defined as the ratio of pore volume ($V_b - V_g$) to bulk volume (V_b), and in this work it is expressed as a percentage (φ), in equation form

The open porosity of Gilsocarbon and PGA samples were measured in a helium pycnometer before and after deformation, and the closed porosity was calculated by using the equations below

$$Total\ porosity\ volume\ (\%) = \frac{V_T - V_C}{V_T} \times 100 \quad \textbf{(3.25)}$$

$$CPV = Total\ porosity\ volume - OPV \quad \textbf{(3.16)}$$

Where V_T represents the theoretical volume while the V_C represents the volume of the crystallites. The total porosity volume is the overall closed pore volume (CPV) and open pore volume (OPV).

3.3.2 Mercury porosimeter

Mercury porosimetry can be used to characterize pore size distribution ranging from 0.003μm to 950μm. Some of the useful sample characteristics obtained are the total porosity, open (accessible) porosities, mean pore diameter and distributions of the pore size, a direct comparison was made between the amount of effective porosity available to mercury and to helium. The experimental method in mercury porosimetry involves filling up an evacuated sample holder with mercury and then applying pressure to force the mercury pore spaces [104]. Both applied pressure and intruded volume are recorded and the data produced can be used to calculate the sample characteristic mentioned above.

Mercury porosimetry uses the Washburn equation (Equation 3.17) to describe the intrusion of mercury into a porous material as a function of pressure applied to the mercury [104-106]. Mercury is used because it is non-wetting and non-reactive for most solid surfaces. It also has a contact angle (θ) of about 140° for most solids and it will not enter fine pores until sufficient pressure is applied to force its entry into the pore[105].

$$r = \frac{0.736}{P} \quad \textbf{(3.17)}$$

Where *P*, the applied pressure, is in MPa and r, the pore radius, is in micrometers. PoreMaster 60 shown in Figure 3.11 was used for the mercury porosimetry measurements. It generates

pressure up to 414 MPa for pore size analysis from over 950 μm to 0.0036 μm pore diameter[107]. The evacuation setting was increased to 2 hours to allow proper evacuation of the glass cell and to allow mercury settling in the sample steadily during low pressure measurement.

Figure 3.11 PoreMaster series adapted from Quantachrome limited

The mercury porosimeter can cause damage to graphite specimens above a critical pressure range, which could make the porosimetry measurements misleading [106]. The results of porosity measurements are treated carefully taking account of the limitations of the technique, therefore good absolute, comparative values of porosities were obtained.

3.4 Dynamic Young's modulus measurement

The traditional method for measuring the dynamic elastic constants has been to employ an ultrasonic method in which the time of flight of an ultrasonic pulse along a specimen is measured [108]. A high frequency electrical pulse is transmitted to a sender piezoelectric transducer that creates an ultrasonic wave that passes through the sample and is received by the receiver piezoelectric transducer and reconverted to an electric signal [108, 109]. Travel time for the pulse through the specimen is measured. The use of both compressional and shear

transducers permits both compressional waves and shear waves to be observed so that both compressional wave velocity (V_L) and transverse wave velocity (V_T) can be determined. The bulk density of each sample is calculated from the ratio of weight (mass) to bulk volume of the sample. The dynamic Young's modulus (E) and shear modulus (G) of each sample before and after loading was calculated from the velocity of longitudinal waves and shear ultrasonic waves using the following equation [108, 110]

$$E = \rho V_L^2 \tag{3.18}$$

$$E = \rho\left(\frac{3V_T^2V_L^2 - 4V_L^4}{V_L^2 - V_T^2}\right) \tag{3.19}$$

$$G = \rho V_T^2 \tag{3.20}$$

The equations above shows the relationships between longitudinal and transverse wave velocities with Young's modulus and shear modulus.

3.5 Triaxial Deformation Apparatus (Big rig)

The big rig consists of a pressure vessel using synthetic oil as the confining medium into which a piston is introduced to apply elevated axial loads to the specimen; the confining pressure and axial load are independently controlled and measured. This rig was initially designed to study meso-scale fracturing processes. The rig is called big rig because it can be used to deform relatively large sample (25 mm diameter × 55 mm long cylindrical samples) and it can be used at pressures up to 300 MPa.

The big rig allows compression testing by superimposing a hydrostatic pressure and uniaxial stress. The system can deform samples under axially symmetric shortening or axially symmetric extension by using a servo-controlled axial loading system that lower or withdraws the piston to produce the required deformation conditions. The picture and the cross section of the big rig is shown in Figure 3.12. A pressure vessel is housed in a cylindrical shaped steel shield.

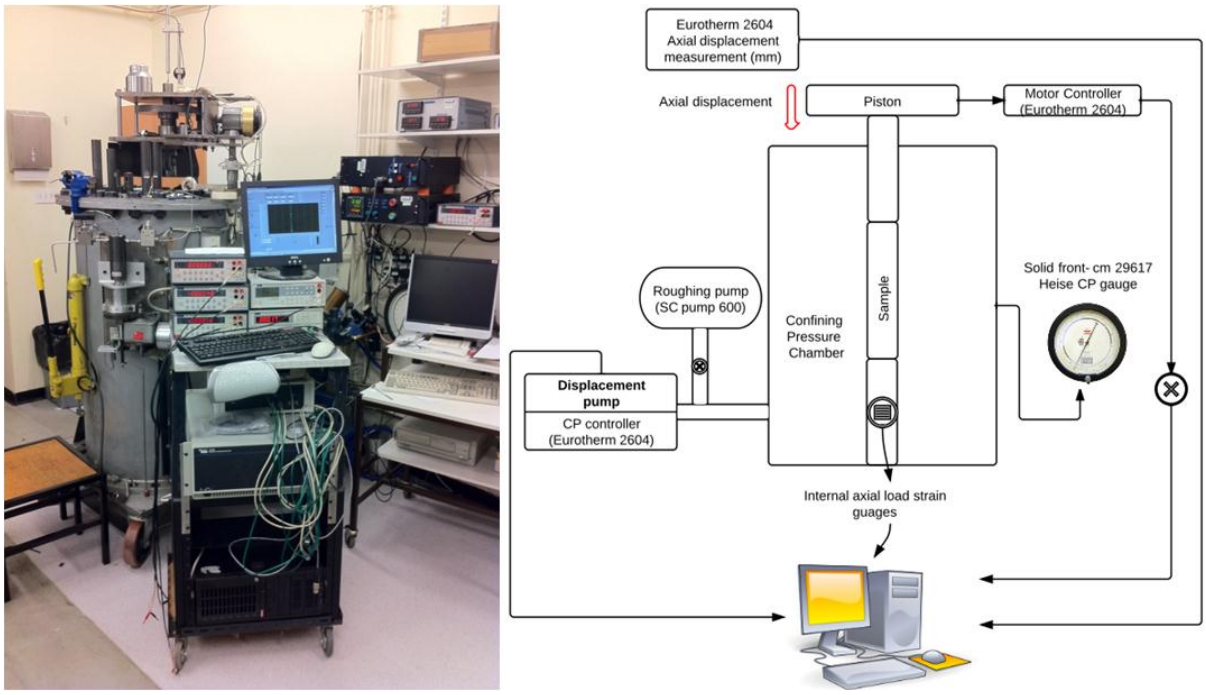

Figure 3.12 Big rig and Schematic of the whole big rig system

Confining pressure was applied using a compressed air-driven Haskel-type pump (SC Pump 600) to pressurize the vessel up to 7 MPa. Further confining pressure (up to 300 MPa) was controlled using a servo-controlled pressure regulator above 7 MPa. The confining fluid is Di-ethyl ester called Reolube-DOS® (chemically inert, no health hazard in use). Confining pressure was measured using a pressure transducer which was calibrated against a high accuracy solid front 29617 Heise pressure gauge. Confining pressure can be measured to an accuracy of 0.156 MPa, as shown in Figure 3.16.

3.5.1 Axial loading system

The axial loading system consists of ball screw press with an axial load capacity of 35tons. The ball screw is driven via a short gear train; in turn driven by a DC servo motor with a maximum speed of 3000 rpm and torque 90 Nm when driven by 60 Vdc from a servo- amplifier. The servo-control system generates uniform axial displacement rate by measuring the displacement of the piston with a LVDT (Linear Variable Differential Transformer) and automatically adjusting the motor speed to keep the piston displacement rate constant. Axial displacement rates of 1.22 mm/min that correspond to strain rate of 0.0004 s^{-1} were used in this work for both small and large samples respectively. The internal force gauge in the big rig measures axial force during the axial deformation experiment. As the force deforms strain gauges, the strain gauges convert the deformation strain to electrical signals and hence into a force value that is displayed on the instrument. The force gauge was calibrated, the result is discussed below.

3.6 Pressure vessel (Seismic velocity rig)

This is a high pressure (500 MPa) rig designed for measuring seismic velocities of solid materials at room temperature. Each sample was assembled (as shown in Figure 3.14) and placed in a pressure vessel so that pressure can be applied. Acoustic velocity measurements were taken during hydrostatic loading in the seismic velocity rig shown in Figure 3.13. In this experiment, the acoustic transducers used are 25mm diameter piezoelectric ceramic plates supplied by Morgan Acoustic Ceramics. The piezoelectric material used is lead zirconium titanate, referred to as PZT ($Pb(Zr,Ti)O_3$). These transducer plates (Sender and receiver) are operated when confining pressure was applied; good acoustic and electrical connections are necessary to achieve a good result. This work was carried out at confining pressure up to 200 MPa. The sample lengths were measured before and after test, length corrections were considered during data processing to take account of the change in volume and hence length of the sample due to the applied hydrostatic pressure. The changes in axial and volumetric strain as graphite compressed under hydrostatic compression are known from the static loading tests in the big rig. The results obtained from this experiment allowed detailed comparison between volume change and velocity change. The sample's density was corrected in order to calculate the dynamic elastic moduli as the sample compressed hydrostatically.

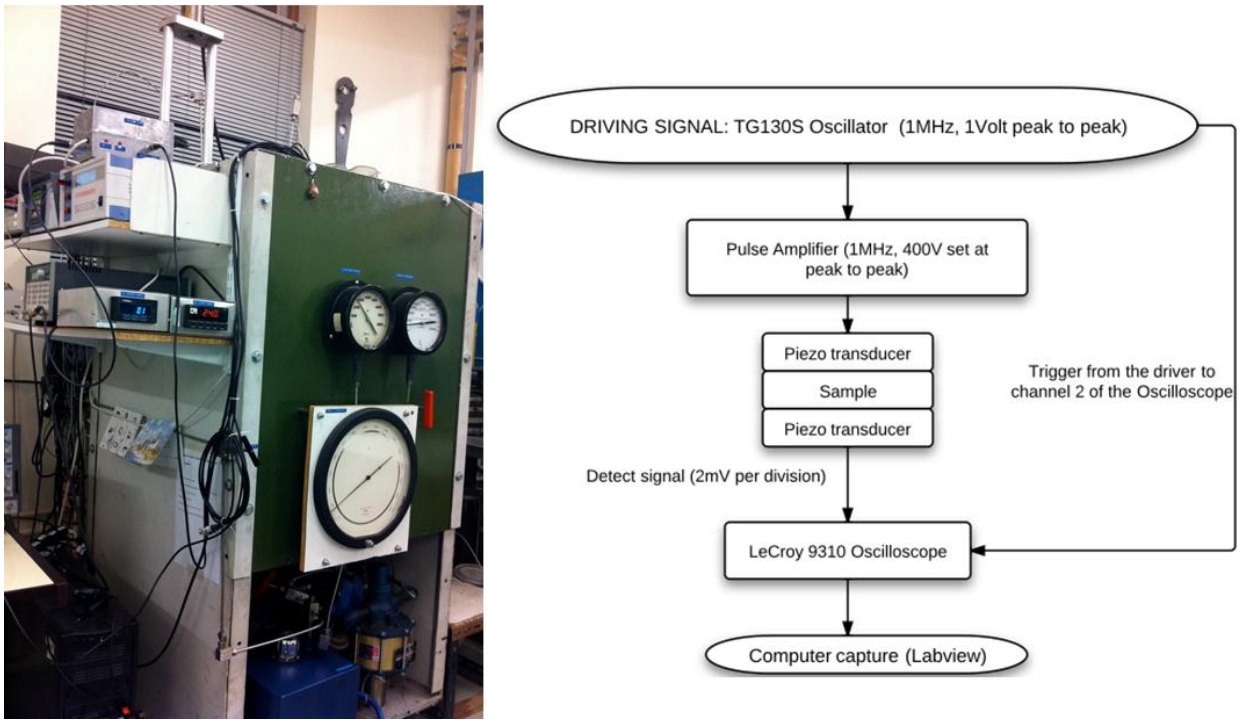

Figure 3.13 Picture and Schematic diagram of seismic velocity rig

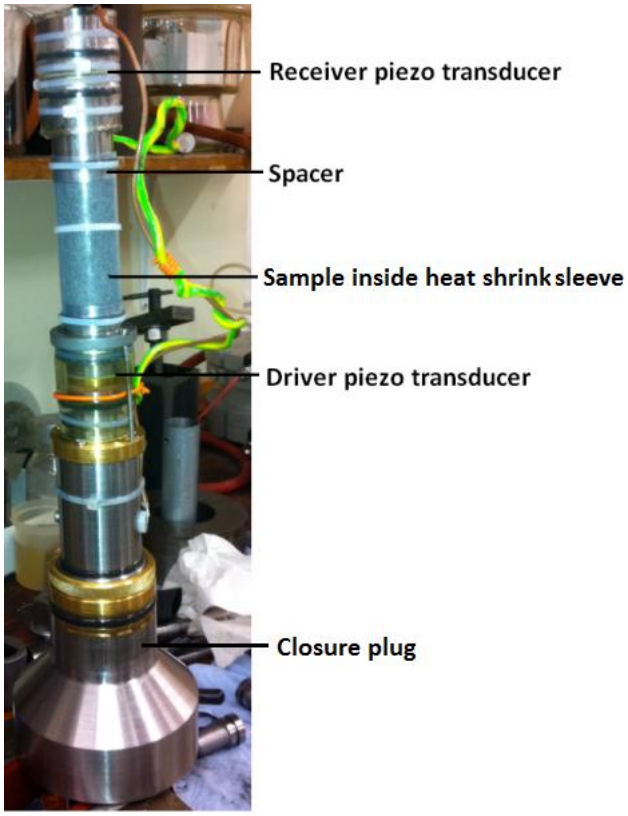

Figure 3.14 Piston assembly

3.7 Strain gauge instrumentation

A strain gauge is a device used to measure the strain (axial and circumferential) of a solid material by producing a resistance change proportional to the change in strain. YFLA-5-NOL post yield strain gauges were used in this work; they were made and supplied by Tokyo Sokki Kenkyujo Co. This gauge was used because it was designed for measurement of large strains up to 15 – 20 % without creeping or cracking. The gauge length, width and resistance are 5 mm, 2 mm and 120 ± 0.3 Ω respectively, with a gauge factor of 2.10 ± 2 %. The operational temperature is -20~+80 ^{O}C. CN-E glue is designed for bonding strain gauges to porous materials; the curing time under normal conditions is 4 - 120 seconds. It was used to attach the strain gauges to the graphite sample with the help of a technician (Bill Storey).

3.7.1 Sample assembly

Four strain gauges were attached to each sample, two strain gauges were attached parallel to the sample axis and two parallel to the sample circumference. There are two layers of heat shrink sleeving applied, one to protect strain gauges and connecting wires and the second to isolate the sample from the confining pressure. The sample was jacketed with heat shrink to prevent the wire attached to strain gauges from breaking. The strain gauge driving voltage is 125 ΩH. To avoid heating, the energy generated by each gauge is 1 watt (YFLA-5-NOL post yield strain gauges are sensitive to keeping low watt).

The sample was jacketed with heat shrink to the loading pistons. The connected cables were pushed through the hole in the middle of the piston as shown in Figures 3.15A and 35B below (final assembling). The whole assembly is lowered into the pressure vessel, making sure that it was carefully placed on top of the internal load cell. The loading frame (gear train, ball screw, driver motor and external loading cell) are pivoted into place and the main closure nuts are tightened to the pressure vessel. The data logging proceeds for the duration of the test, the output data is saved as text file containing raw data such as time (hours), time (seconds), strain 1, strain 2, strain 3, strain 4, force (kN), volumetric strain, confining pressure (MPa). The saved files can be opened in an Excel spreadsheet for further analysis. The sample final assembling is shown in Figures 3.15A – 3.15D.

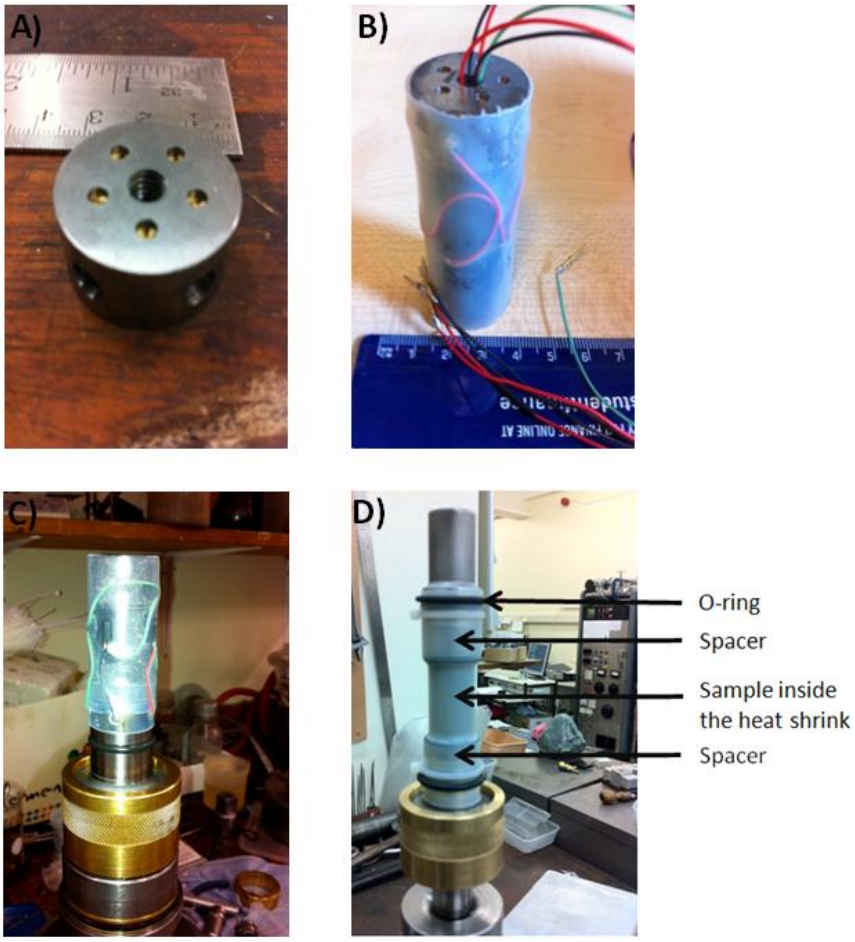

Figure 3.15 Sample assembling; A) component built by the author to protect the cables during pressurization, B) sample with strain gauges attached, covered with heat shrink, C) the sample jacketed to the loading piston, D) the sample was jacketed with heat shrink to the loading pistons

3.8 Hydrostatic tests

Each cylindrical graphite specimen was subjected to confining pressure up to 30000 Psi (200 MPa). The pressure rate was controlled by a servo-controlled motor that moved a piston in and out of a pressure vessel via a gear box and screw jack. Servo control was achieved with a Eurotherm PID control which used the pressure transducer as the feedback. The longitudinal and circumferential strains and pressure were continuously logged throughout the experiment. When a pressure of 200 MPa was reached, the pressure was lowered at the same rate at which it was applied and the strain was measured as the pressure was lowered. The loading and unloading pressure-strain curves from the data points represent the deformation behaviour of graphite under a complete pressure cycle. The effect of hydrostatic cycling on graphite deformation was also investigated by repeating the whole hydrostatic test procedure. The effect of creep on

hydrostatic deformation was investigated by loading graphite up to 200 MPa and then holding the pressure constant for 24 hours before unloading to atmospheric pressure.

3.9 Axial deformation tests

Axial compression was performed on hydrostatically compressed graphite specimens to obtain useful data such as Young's modulus and Poisson's ratio. When the required confining pressure (200 MPa) was attained, the axial drive motor was controlled automatically at desired displacement rate (1.22 mm/min). Each sample was loaded to different stresses; cyclic axial deformation test were also conducted to various differential stresses. At the end of the test, the axial load was removed. The confining pressure was then released, and the sample was taken out of the rig.

3.10 Seismic velocity measurements

The compressional and shear wave velocities were determined for the samples from the transit time of ultrasonic pulses (approximately 1 MHz). The time difference between the two transducers (sender and receiver) is the time required for the group stress waves to travel through the specimen. The higher the excitation frequency, the more reliable is the time pick (sharp first break at the receiver), but more attenuation occurs at higher frequencies, both within the sample and through the decrease in gain of the pulse amplifier with frequency.

A signal generator (TG130S Oscillator) was used to generate 1 V peak to peak (P - P) square wave pulse or half cycle sinewave. This pulse was amplified to provide a driver waveform of up to 150 V- 400 V P-P for piezo transducer (sender). The rise of the driver waveform was used to trigger a LeCroy 300 MHz digital storage oscilloscope. The detected signal from the piezo transducer (receiver) was connected to the LeCroy9310 Oscilloscope. The signals (pulses at 300ms interval) were averaged to reduce noise. Time of flight was read off from the oscilloscope trace to a resolution of 0.0075 μs. In choosing the first break, it is estimated that the time could be estimated reliably to half of 1 % of the time of flight. The time of flight through the steel piston at each end of the specimen (determined separately) was subtracted from the total time of flight through steel and sample. This was conducted by measuring the time delay with the platens in contact (no sample) with an applied load.

3.11 Calibration data (Hydrostatic pressure measurement)

The big rig loading system was calibrated by carrying out hydrostatic and axial deformation tests on an EN24 steel specimen in order to measure the strain in a material with well-known elastic properties. Confining pressure was measured using a pressure transducer with an excitation voltage of 11.72 V. The calibration was carried out, and was very linear with parameters 47.1 MPa/mV with 0.16 mV output at zero pressure. The calibration graph of the pressure transducers and the force gauge are shown in the Figures 3.16 and 3.17 respectively. At zero force, the internal force gauge output during loading and unloading are 0.0782 V and 0.1641 V respectively.

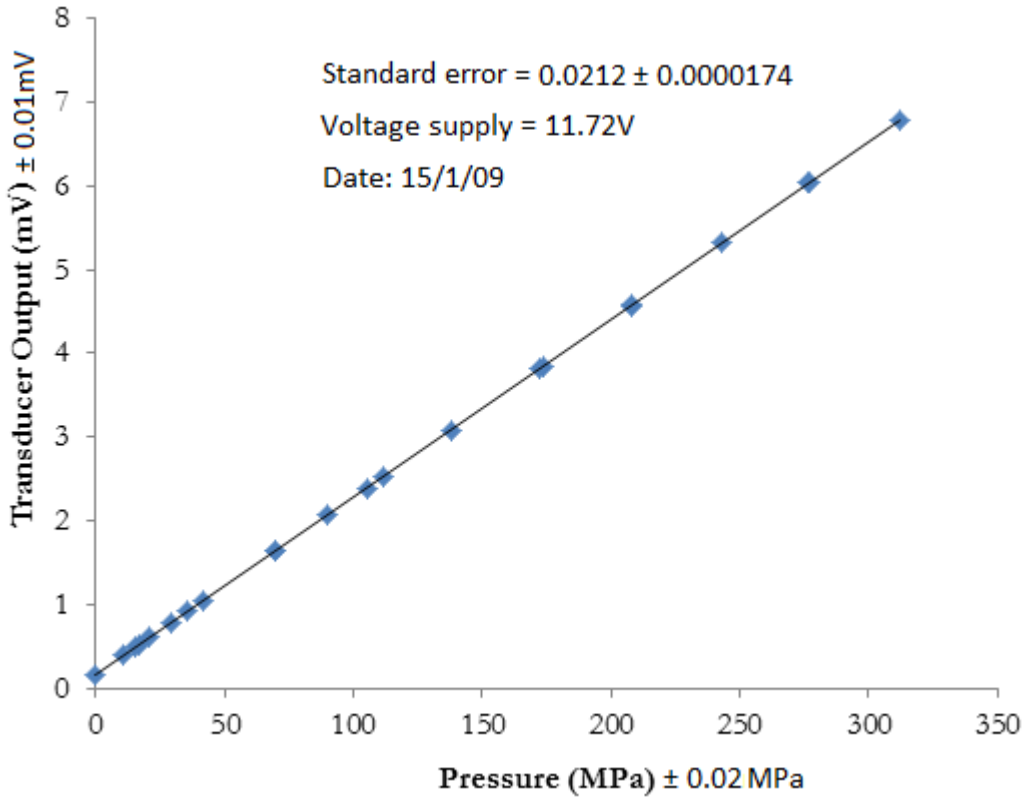

Figure 3.16 Calibration for the pressure transducer, the voltage supply is 11.72V

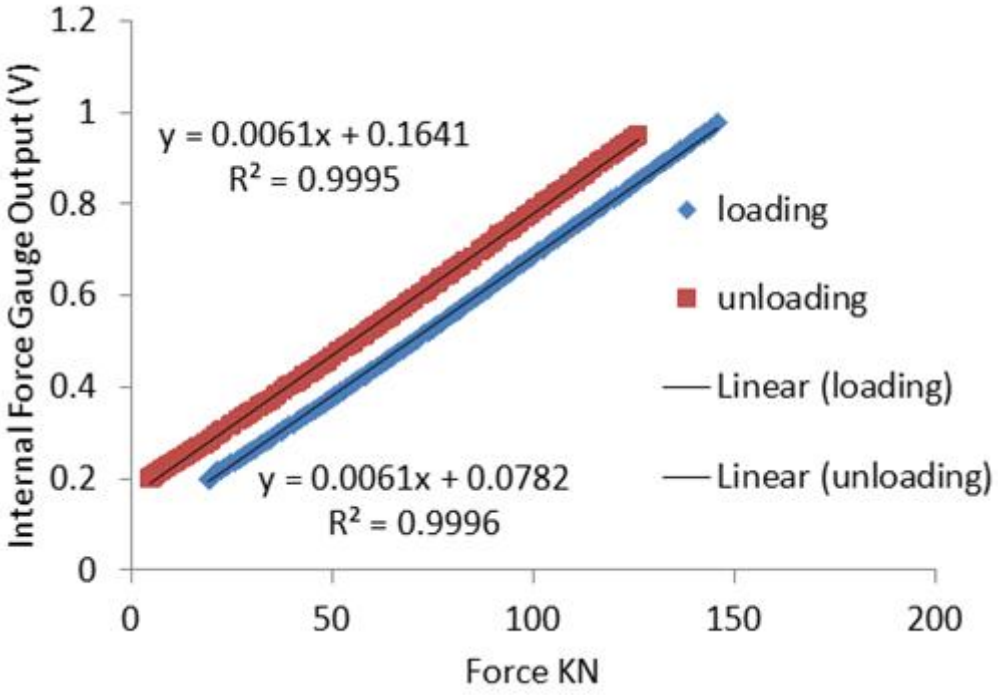

Figure 3.17 Big rig force gauge calibration

3.12 Calibration data (Hydrostatic P- and S- waves measurements)

The total time of flight of the ultrasonic pulse recorded includes the time taken for the wave to travel through the steel piston between the piezoelectric transducers and the sample. A correction for this time must be made. This was achieved through running a calibration with no sample so that the pistons are in direct contact with each other, so that the time of flight measured is only the time taken for the seismic wave to pass through the pistons. Such a calibration was run at a number of pressures and the pressure of flight was seen to decrease with time for two reasons

- the steel was becoming slightly stiffer with increasing pressure and
- the length of the steel piston reduced as the pressure increased.

Such a calibration is shown in the Figure 3.18.

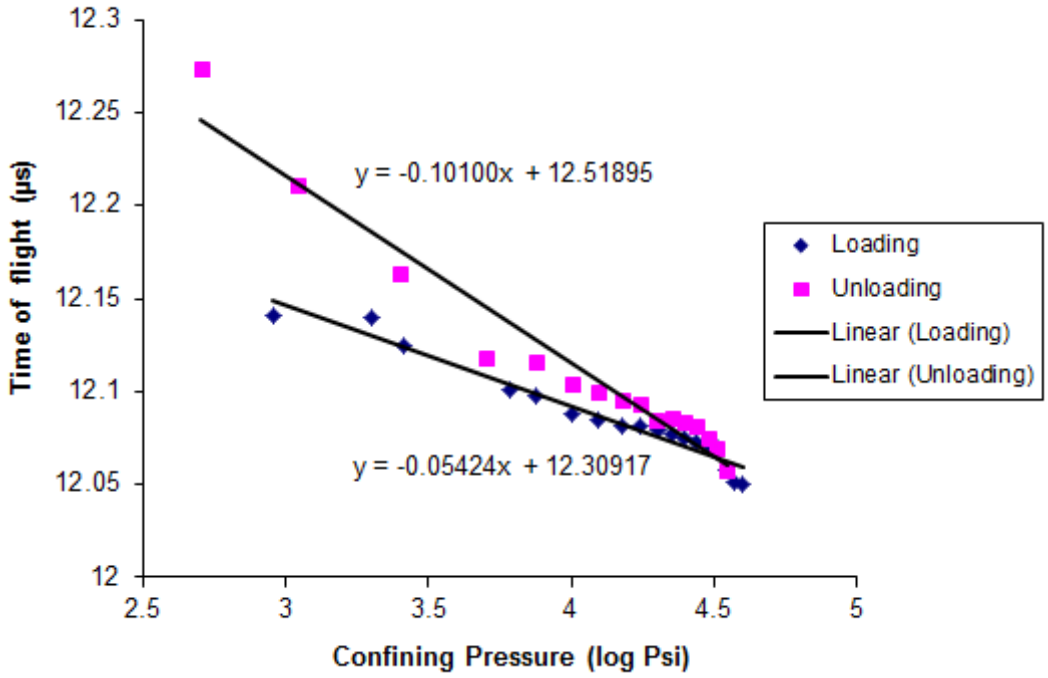

Figure 3.18 P-P transducer Assembly Calibration

The linear equations obtained from the pressure circle in Figure 3.18 were used to correct the time of flight of the P-waves on all the samples measured. Dynamic Young's modulus and shear modulus were calculated from the P- and S- wave velocities respectively using Equations 3.18 and 3.20 in Chapter 3.

The P-S sample- transducer arrangement allows simultaneous measurements of P and S velocities. The P-S sample was loaded up to 208 MPa without a sample and the history of pressure versus time of flight is shown in Figure 3.19.

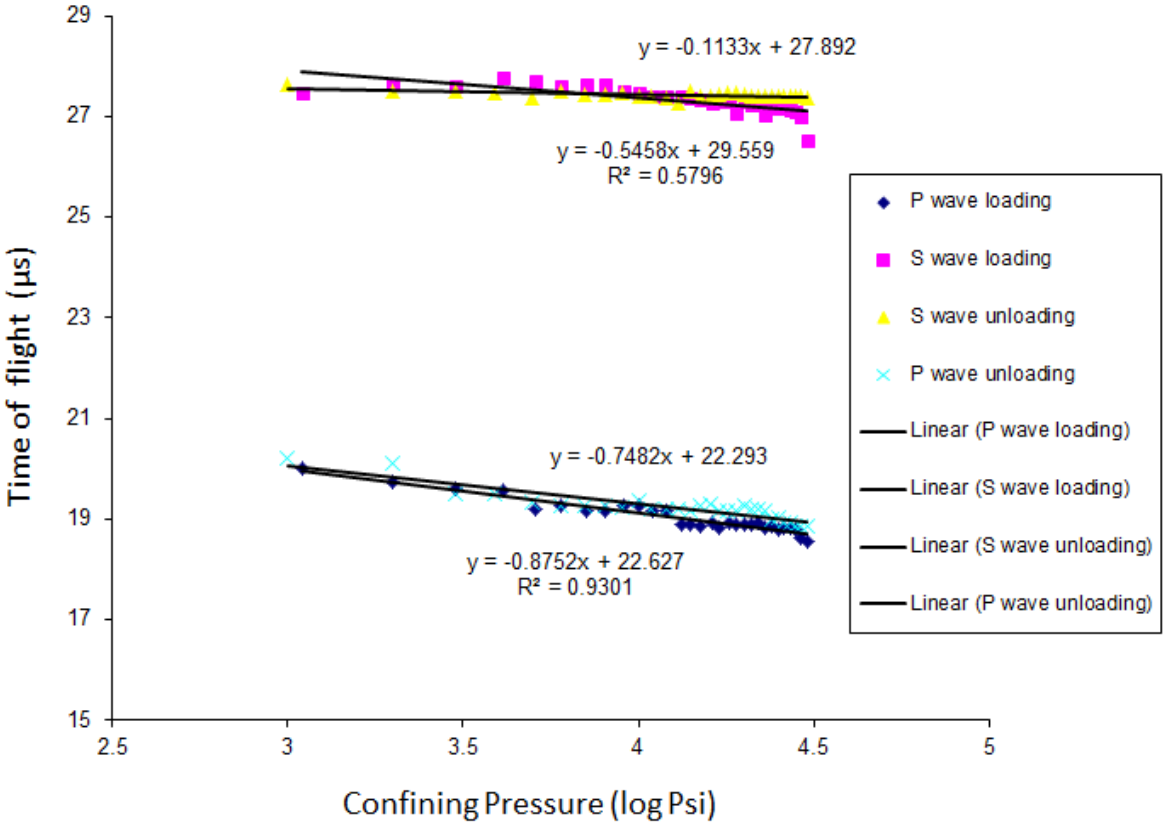

Figure 3.19 P-S transducer Assembly Calibration

Similar calibration that was done with the P-P transducer assembly in the Figure 3.18 was repeated with the P-S transducer assembly, the calibration is shown in the Figure 3.19. The linear equations obtained from the pressure circle in the Figure 3.19 were used to correct the time of flight of the S-waves on all the samples measured in this experiment. Shear moduli was calculated from the S- wave velocities respectively using Equation 3.20 in Chapter 3

3.13 Conclusion

The mechanical properties of nuclear graphite are necessary to determine the structural integrity of graphite component in a reactor. These mechanical properties (static and dynamic elastic moduli, uniaxial strength, strain to failure e.t.c.) are vital to determining the capability of the structural strength and integrity of the reactor core.

The irradiation changes to graphite properties are related to opening and closure of porosity and reorientation of the crystallites in polycrystalline graphite. Loading graphite under high hydrostatic pressure (up to 200 MPa) is a method of simulating this behaviour and was employed in this work. In order to understand changes in graphite microstructure under stress, a change in microstructure will be induced by loading the samples hydrostatically and also with differential stress, using two high pressure rigs (big rig and seismic rig).

Non-destructive X-ray tomography will be investigated for its ability to determine the microstructure within individual test samples. It allowed samples to be analysed before and after the loading tests. Image analysis techniques (using Matlab) will be used to enhance information such as pore size distribution in the virgin and deformed micrographs. The visible microstructural change in the deformed sample micrographs due to stress history will be compared to the original micrographs, so that the microstructural evolution and modifications as a result of hydrostatic stress can be established. The X-ray diffraction method will be investigated in order to examine the orientation of the crystals in the graphite microstructure before and after tests.

Precise dimensional measurements (diameter and length) of all deformed samples will allow macroscopic dimensional changes to be determined; the pore size distribution of the deformed samples will be calculated (using helium and mercury porosimeter) and compared to virgin samples values for each test. Each cylindrical shaped graphite sample's identity (ID), the dimensions and the samples direction of extrusion (AG and WG) is shown in the Table 3.4.

Table 3.4 The samples identities, directions and dimensions as well as the test done on each sample

Sample	ID	Direction	Diameter (mm)	Height (mm)	Machining and Experiments
Gilsocarbon	A2		9.97	20.03	Machined to 9X19 mm cylindrical shape samples for Hg porosimeter
	E1		20.02	40.04	It was loaded up to 200 MPa in seismic rig, but there was a leak
	E2		20.02	40.04	Confining pressure of 200 MPa
	E3		20.02	40.04	
	E4		20.02	40.07	Machined to two 9X19 mm cylindrical shape samples for Hg porosimeter
	I1		24.96	50.84	Confining pressure of 200 MPa
	I2		24.98	50.84	Confining pressure of 200 MPa and cyclic differential forces of 28 KN & 17 KN
	I3		24.98	50.85	Confining pressure of 202 MPa and cyclic differential forces of 36 KN & 20 KN
	I4		25.37	50.81	Seismic loading up to 207 MPa with a P rod (Pwave)
	I5		25.37	50.81	Seismic loading up to 207 MPa with a S rod (P&Swave)
	I6		25.37	50.81	Seismic loading up to 207 MPa with a S rod (Swave)
	I7		25.34	50.81	Cable disconnected twice during the test, sample was still loaded up to 80 MPa
	I8		25.37	50.82	Cyclic confining pressure of up to 200 MPa, down to 20 MPa, up to 200 MPa,down to 16 MPa, up to 100 MPa
	I9		25.37	50.82	
	I10		25.38	50.82	Cyclic seismic loading up to 207 MPa with a P rod (Pwave)
	I11		25.38	50.82	Machined to two 9X19 mm cylindrical shape samples for Hg porosimeter
PGA	B2	WG	9.97	20.02	Machined to 9X19 mm cylindrical shape samples for Hg porosimeter
	B4	AG	10	20.04	Machined to 9X19 mm cylindrical shape samples for Hg porosimeter
	F1	WG	20.02	40.06	Confining pressure of 200 MPa
	F2	WG	20.01	40.15	Confining pressure of 60 MPa and cyclic differential forces of 16 KN & 11 KN
	F3	WG	20.03	40.07	Confining pressure of 60 MPa and cyclic differential forces of 17 KN & 12 KN

	F4	AG	20.02	40.07	Confining pressure of 60 MPa
	F5	AG	20.03	40.07	Confining pressure of 200 MPa
	F6	AG	20.02	40.04	Repetition of J8 but Confining pressure of 200 MPa and cyclic differential forces of 17 KN & 20 KN
	F7	AG	20.04	40.09	Confining pressure of 60 MPa and cyclic differential forces of 16 KN & 11 KN
	J1	WG	25.01	50.85	Confined up to 58 MPa, then shut circuit, sample reassembled and loaded up to 200 MPa
	J2	WG	25.01	50.88	Confining pressure of 200 MPa and differential force of 28 KN
	J3	WG	25.01	50.84	Confining pressure of 200 MPa and cyclic differential force of 17,20,23 & 28 KN
	J4	WG	25.01	50.99	Confining pressure of 60 MPa
	J5	AG	24.99	50.85	Confining pressure of 120 MPa
	J6	AG	25	50.87	Shut circuited during test, beside the sample cracked, therefore the result was not reliable
	J7	AG	24.98	50.84	Confining pressure of 200 MPa and differential force of 28 KN
	J8	AG	24.97	50.84	Confining pressure of 200 MPa and differential force of 36 KN
	J9	AG	25.35	50.84	Seismic loading up to 207 MPa with a P rod (Pwave)
	J10	AG	25.37	50.84	
	J11	AG	25.38	50.81	
	J12	AG	25.32	50.81	Cyclic confining pressure of up to 200 MPa, down to 20 MPa, loaded and unloaded at 200 MPa
	J13	AG	25.31	50.82	Machined to 20X39 mm cylindrical shape sample for Hg porosimeter
	J14	AG	25.36	50.82	
	J15	AG	35.35	50.82	Seismic loading up to 207 MPa with a S rod (Swave)
	J16	AG	25.36	50.82	
	J17	AG	25.36	50.82	
	J18	AG	25.34	50.82	Machined a disk for XRD experiment & 9X19 mm cylindrical shaped sample for Hg porosimeter
	J19	AG	25.36	50.82	

	J20	AG	25.33	50.82	
	J21	WG	25.33	50.73	
	J22	WG	25.28	50.72	Confining pressure of 200 MPa, loaded and leave up to 24hours before unloading (creep test)
	J23	WG	25.31	50.73	Cyclic seismic loading up to 207 MPa with a P rod (Pwave)
	J24	WG	25.31	50.73	Seismic loading up to 207 MPa with a S rod (P&Swave)
	J25	WG	25.3	50.73	Machined to 20X39 mm cylindrical shape sample for Hg porosimeter

CHAPTER 4

4 Results

The irradiation changes to bulk properties are said to be, in part, related to closure of porosity and reorientation of the crystallites [60, 82]. Pore closure and crystallite reorientation can be mimicked by loading graphite under high hydrostatic pressure [54]. PGA (WG and AG) and Gilsocarbon nuclear graphites were loaded hydrostatically up to 200MPa, the relationships between the graphites' mechanical properties such as static and dynamic bulk modulus, shear modulus and Poisson's ratio were analysed. The relationships between the mechanical properties of different loading modes such as

- hydrostatic loading using strain gauges,
- hydrostatic loading followed by shortening,
- cyclic hydrostatic loading,
- measuring acoustic loading under hydrostatic stress to express the moduli

were analysed. This research combined measurement of properties under high pressure and compares the experimental results with various to effective medium (EM) models in Chapter 5.

Each sample was characterized before (pre-microstructural characterization) and after loading (post-microstructural characterization), by using the equipment listed in the Chapter 3. The results obtained are discussed in this chapter.

4.1 Pre-microstructural characterization and properties measurement

4.1.1 X-ray goniometry results

A summary of the experimental X-ray diffraction spectrum is shown in Figure 4.1, showing the positions of all Bragg reflections. A general texture two dimensional scan was taken; three peaks were needed for the texture measurement. Several pole figures are needed to define the ODF (as discussed in the Chapter 3). Since the 002, 100 and 110 peaks are the most intense and sharp peaks, they were selected for the texture measurements.

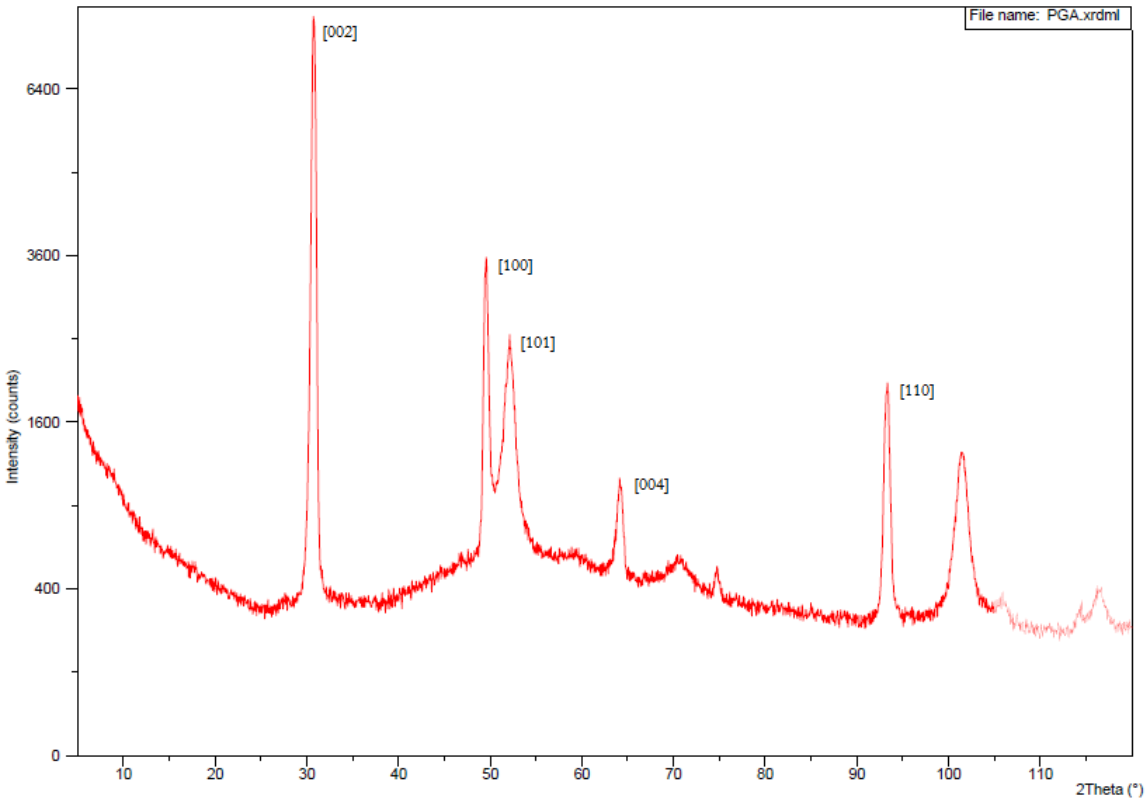

Figure 4.1 X-ray diffraction spectrum for PGA

The pole figures shown below (Figures 4.2 and 4.3) are only projections of three crystallographic axes of the full ODF. The pole figures describe the orientation distribution of all crystal cells of a given phase of the sample. The experimental pole figures of the sample for three graphite crystal planes (*h k l*) are determined by X-ray diffraction and they are shown in the Figures 4.2a and 4.3a. Gilsocarbon (Figure 4.2) is nearly isotropic, this is shown by uniform intensity across the pole figures while PGA (Figure 4.3) showed preferred orientation (anisotropic characteristic).

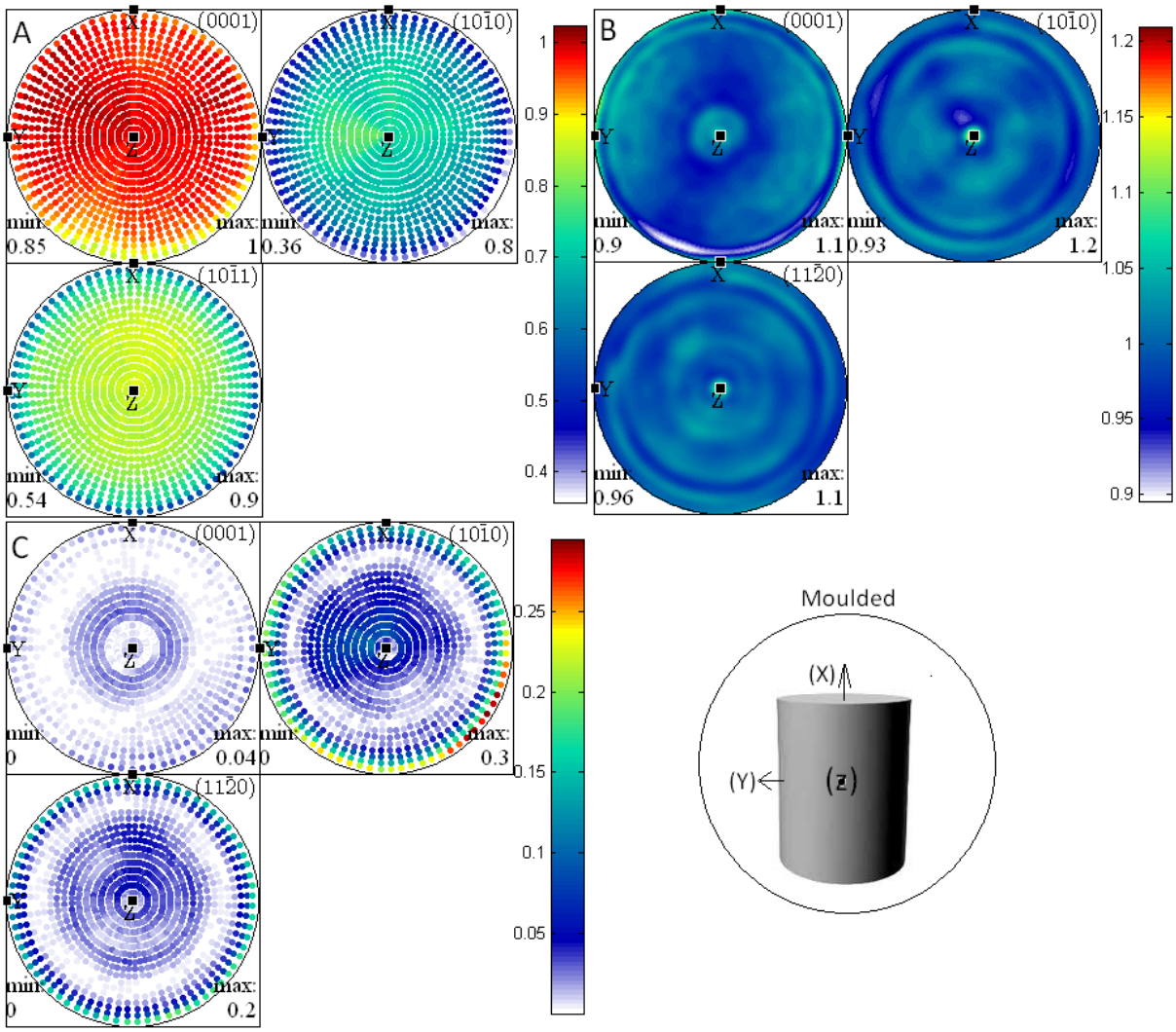

Figure 4.2 Pole figures of the considered Gilsocarbon graphite sample, a) experimental figures derived by the X-ray diffraction method, b) recalculated pole figures from ODF derived from the experimental pole figures, c) difference between calculated ODF and the experimental data. The set colour range in represent the intensity scales. The colour range have no unit, it was denoted as multiples of uniform distribution (mud) values. It varies from 0 to 1.2mud for the ODF derived

The region of extreme intensity is in some way correlated with the axes of the sample coordinate system (X is the extrusion direction; Y and Z are approximately parallel to the other sides of the original graphite block). The calculated pole figures in the Figure 4.2b show no preferred orientation (the grains are uniformly orientated), however there is an artifact around the circumference. The original pole figure data collected below 75^{O} tilt of the sample can be trusted; the data above 75^{O} is unreliable because of defocusing of x-ray beam which in systematically lower intensity as the tilt is increased. The pole figures for PGA were corrected for the defocusing effect using pole figures for a sample of Gilsocarbon, that has almost no lattice preferred orientation. The moulding of Gilsocarbon might have led to the random orientation of the graphite crystal cells in the block, and having spherical grains (Gilsocarbon coke) or grains

within which the layer plane orientation which has considerable variation, these contributed to the isotropic nature in Gilsocarbon [111].

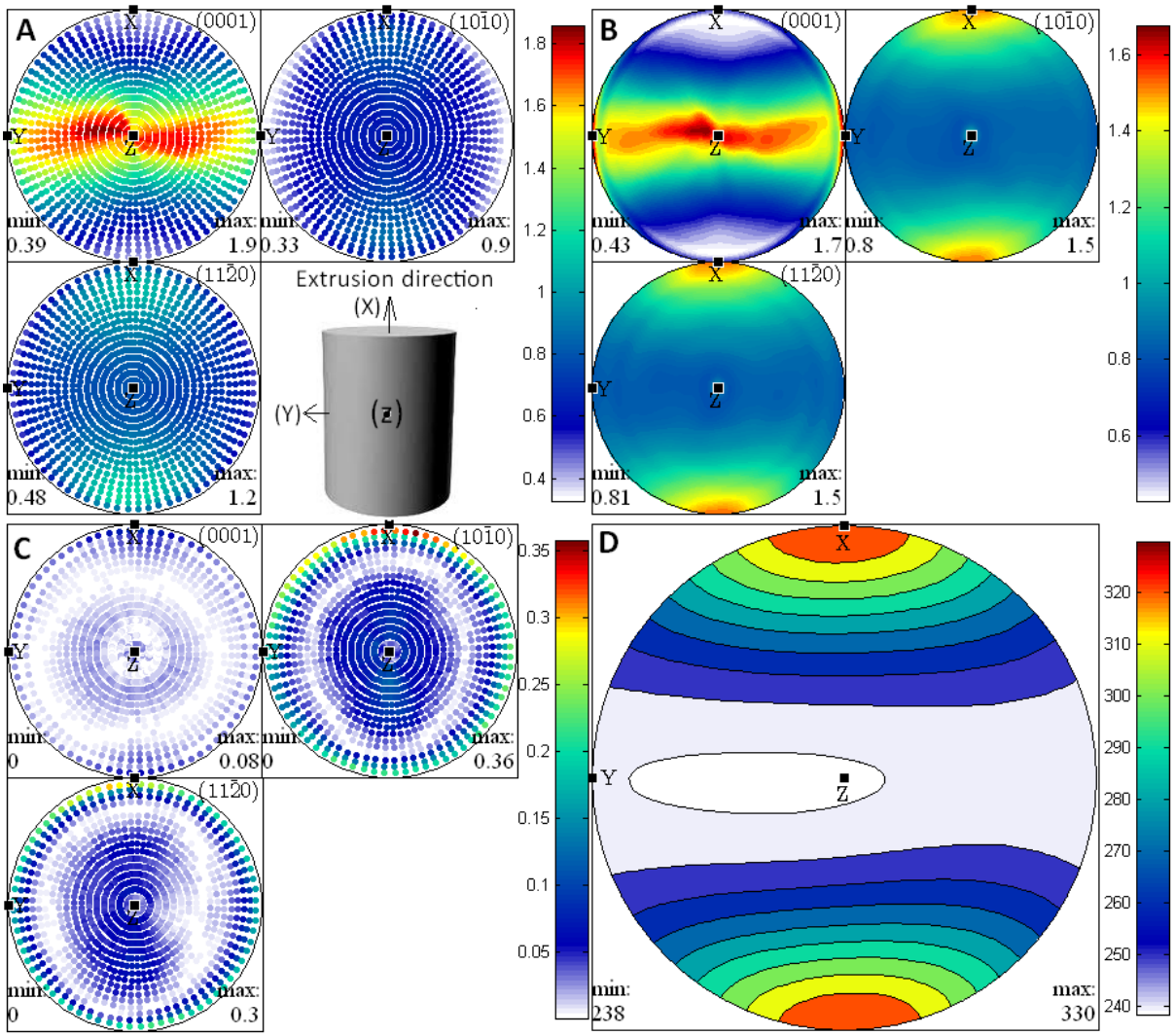

Figure 4.3 Pole figures of the considered PGA (against grain) graphite sample, a) correction of the experimental figures derived by X-ray diffraction data, b) recalculated pole figures from ODF derived from the experimental pole figures, c) difference between calculated ODF and the corrected x-ray data, d) Young's modulus calculated from elastic tensor of a single crystal and ODF. The colour range varies from 0 to 1.7 mud for the ODF derived.

It can be seen that PGA has a preferred orientation of the lattice planes especially the basal planes (Figure 4.3). This is in contrast to Gilsocarbon which has a more random distribution (Figure 4.2). The lattice preferred orientation LPO of anisotropic PGA graphite can be seen from pole figures where the (0001) poles and hence c-axes are preferentially oriented in a plane perpendicular to the extrusion direction. There are weak clusters of the (10$\bar{1}$0) and (11$\bar{2}$0) axes parallel to the extrusion (Figure 4.3).

It is possible to calculate the bulk properties of a polycrystalline material if the properties of the single crystal and ODF are known [112]. The Young's modulus in different directions can be calculated from the single-crystalline graphite elastic tensor(Cij) [21] and ODF assuming the aggregate has no porosity. The minimum and maximum Young's modulus of PGA calculated in this way are 283 GPa and 330 GPa respectively (Figure 4.3d), these clearly indicated that the modulus is higher in the direction (x) parallel to the extrusion direction than in the plane perpendicular to the extrusion direction. These Young's moduli calculated are 28 - 32 times stiffer than the modulus of polycrystalline nuclear graphites (Gilsocarbon and PGA). This is due to the present of 18-26 % porosity in the polycrystalline graphites.

The graphite elastic tensor obtained from Bosak [21] was used to calculate the VRH elastic bulk modulus by using Berryman's equation [113]. The effective bulk moduli of non-porous graphite calculated is 36 GPa. The effect of porosity on Bulk modulus was considered by using models such as VRH, HT and KT. The effective bulk modulus (36 GPa) was used and addition of porosity was also considered in the models. This is discussed later in Chapter 5.

4.1.2 Tomography scans and mercury pycnometry results

The virgin PGA and Gilsocarbon microstructural properties and porosity distributions were characterised using X-ray computed tomography, helium pycnometry and mercury porosimetry. Example tomographic images of PGA and Gilsocarbon are shown in the Figure 4.4. The grey region (region that absorbed X-rays) in the tomographic image represents the graphite material whilst the black region (region with no X-rays absorption) represents the porosity.

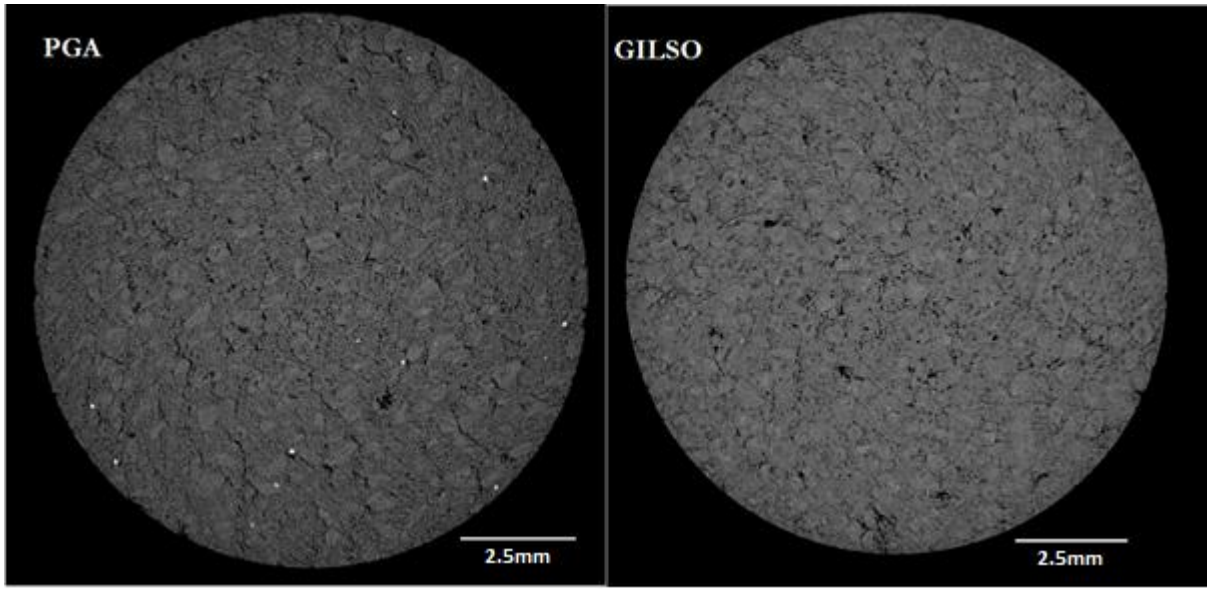

Figure 4.4 Tomography of Virgin PGA and Virgin Gilsocarbon (Gilso)

This non-destructive method allows investigation of the microstructural changes before and after deformation. The smallest resolvable feature in the tomographic image is 14.6 μm, and the change in microstructural features below this resolution was not visible. Since graphite microcracks closure and formation have also been reported in previous work [54] to be responsible for changes in elastic properties, it was important to investigate porosity size ranges beyond the resolution of the tomography technique. Therefore the changes in microstructure were analysed by using mercury porosimetry and helium pycnometry to measure the porosity distribution and total porosity in the virgin and deformed graphite. According to previous work[4], the pore entrance radius in nuclear graphite ranged from nanometres to micrometres (100 μm). In this work, the pore entrance radius ranged between 3.6 nm to 100 μm as shown in the Figure 4.5.

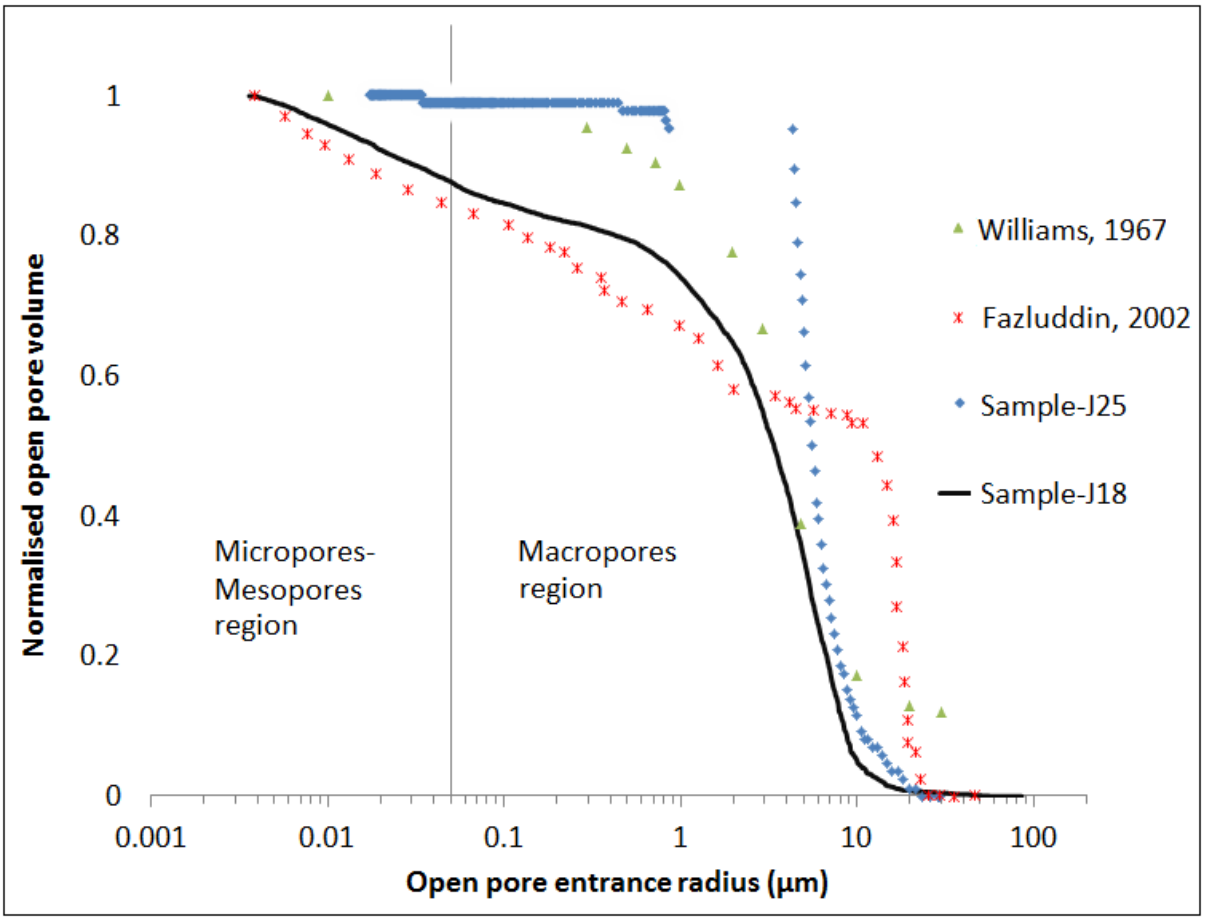

Figure 4.5 Normalised PGA open pore volume entrance radius versus open pore volume

The mercury porosimetry of different sizes of PGA samples (J18 and J25) are compared with other data for PGA [4, 114]. The pore volume of each PGA graphite is normalized by its maximum value in order to compare the author's data to previous work (as shown in Figure 4.5). Sample J25 was a large virgin PGA sample (20 mm diameter by 39 mm in length). Therefore the pore distribution analysis was carried in a macro cell assembly (27 mm diameter by 40.6 mm in length) attached to the porosimeter kit. The pore radius measurement showed an inconsistency between the low pressure and high pressure measurements, which suggested that there was insufficient mercury available to fill the pores of such a large sample.

Sample J18 was a small virgin PGA sample (9 mm diameter by 19 mm in length). Therefore the pore distribution analysis was carried in a small cell assembly (11 mm diameter by 25 mm in length) attached to the porosimeter kit. The pore radius measurement showed consistency between the low pressure and high pressure measurements, which suggested that there was

sufficient mercury available for the analysis due to the smaller size of the sample compared with sample J25.

Fazluddin [84] porosity distribution was similar to the author's measurements (J18) at high pressure as well as Williams' [114] data. At low pressure, the data in the work of Fazluddin [84] increased sharply suggesting that the low pressure measurement might have been run faster due to scan mode settings and short evacuation period compared with the 2 hours evacuation settings used in this study.

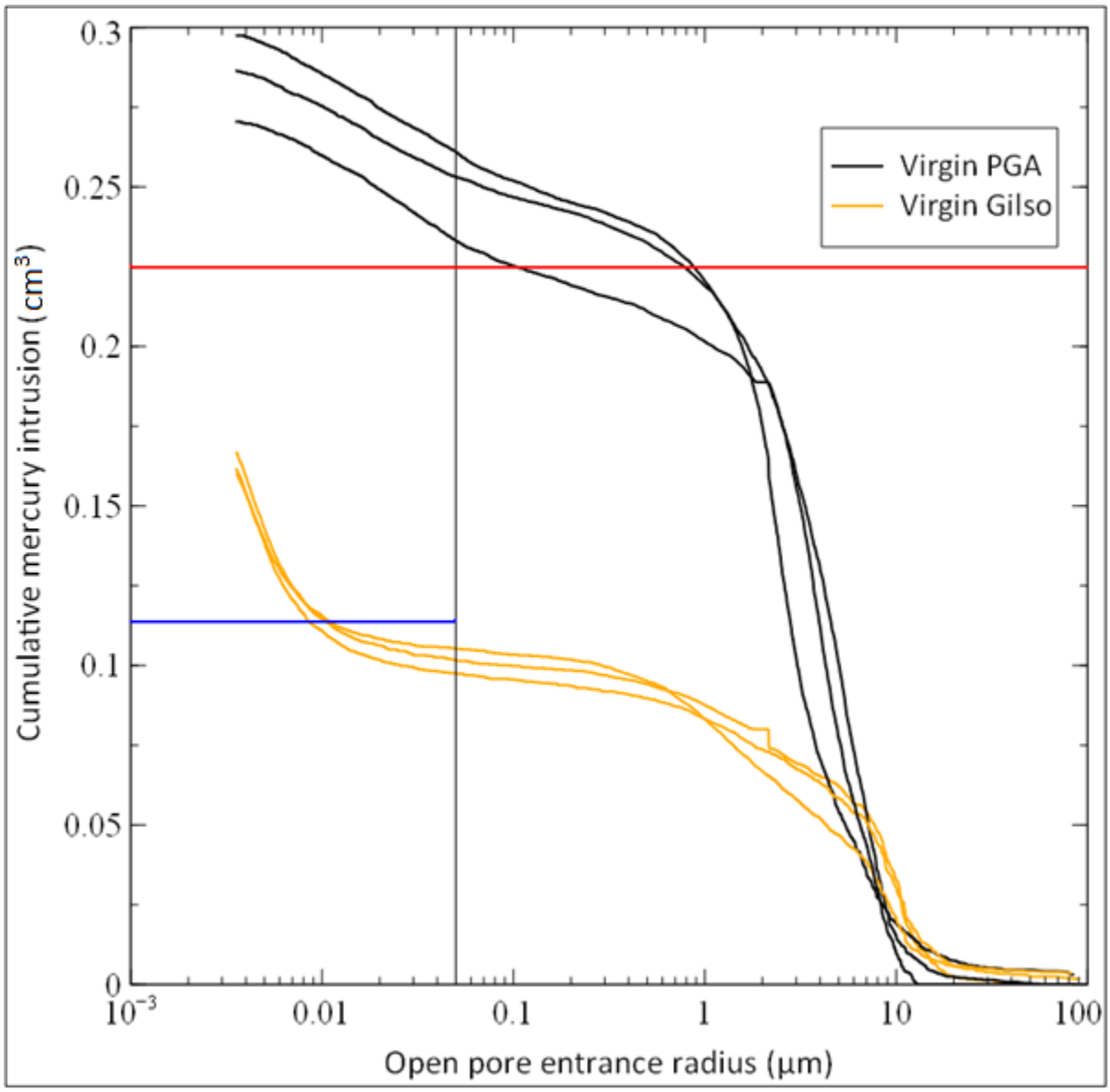

Figure 4.6 Pore size distribution in Virgin PGA (B2, B4 and J18) and Gilsocarbon (A2, I11 and I11b) nuclear graphite

Both PGA and Gilsocarbon samples showed a distribution within the macropore region extending to the mesopore and micropore regions as shown in Figure 4.6. At higher pressures

(13.8 - 20.6 MPa- critical pressure range) measurement, porosity is being created by injected mercury opening new cracks. Previous work [4, 114] suggested that some closed porosity was graphites was made accessible under high mercury pressure and also completely new porosity are generated. The additional accessible porosity might be caused by mechanical break-down of thin pore walls and the rest by reversible elastic crack opening. Therefore it was safer to use mercury porosimetry data only below a critical porosimetry pressure. The critical pressure was estimated from the porosity curves in Figure 4.6. PGA's open pores cumulative mercury intruded volume was 0.225 cm^3 (red line) while the Gilsocarbon open pores cumulative mercury intruded volume was 0.1125 cm^3 (blue line), these values of open pore volume are roughly coincident with an inflexion point in the maximum value of open porosity obtained from the helium pycnometry results. According to previous work [106], the critical porosimetry pressure for most graphite lies between 13.8 - 20.6 MPa. In this work, the mercury porosity was equal to the helium porosity at an intermediate pressure of 20.6 MPa, corresponding to a pore radius of about 0.05 μm.

The PGA graphite samples had the largest volume of open porosity volume due to high cumulative volume of mercury intruded (0.225 cm^3) compared with Gilsocarbon samples which had a lower mercury intrusion volume (0.113 cm^3). The volumes of mercury intruded into PGA and Gilsocarbon were similar to the average open porosity (22% and 10% respectively) obtained from helium porosimetry. It can be physically observed that the graphite microstructure has a wide range of small pore sizes, with a fair proportion of large pores, but the pores size distribution does reflect this. The Graphite material is heterogeneous; therefore different parts of the graphite machined from the same graphite block could show similar or different porosity distribution from each other as shown in the Figure 4.6. After measuring the open porosity by helium pycnometry, the calculated closed porosity of the PGA and Gilsocarbon samples were 4% and 8% closed porosity respectively.

4.1.3 Dynamic Young's modulus and helium pycnometer results

Dynamic moduli (Young's modulus and shear modulus) were measured before and after deformation by using bench top piezoelectric transducers at atmospheric pressure. The Gilsocarbon microstructure is near isotopic and therefore can be an elastically isotropic linear material which can have their elastic properties determined by any two of the following moduli; Young's modulus (E), Poisson's ratio (υ), Bulk modulus (K), Shear modulus (G), and P-wave modulus(M). From any two moduli, any other elastic moduli can be calculated. Bulk modulus is calculated by using Equation 4.1 below

Due to graphite spatial heterogeneity, each graphite sample from the same graphite block can be expected to display significant differences in moduli as shown in the Figures 4.7 and 4.8.

Table 4.1 Average DYM of the graphite

Graphite	Average E (GPa)	Average G (GPa)
PGA-WG	11.1	4.2
PGA-AG	5.9	3.3
Gilsocarbon	12.4	5.1

The average DYM and shear modulus of PGA-WG, PGA-AG and Gilsocarbon were shown in the Figures 4.7 and 4.8. These values (shown in Table 4.1) correspond with the values from previous work [115, 116] on PGA (DYM = 11.7 GPa and shear modulus = 5.4 GPa respectively) and Gilsocarbon (DYM = 11.6 GPa). There was a vague trend of DYM lowering with increase in porosity in the PGA while the Gilsocarbon DYM seemed to be independent of porosity.

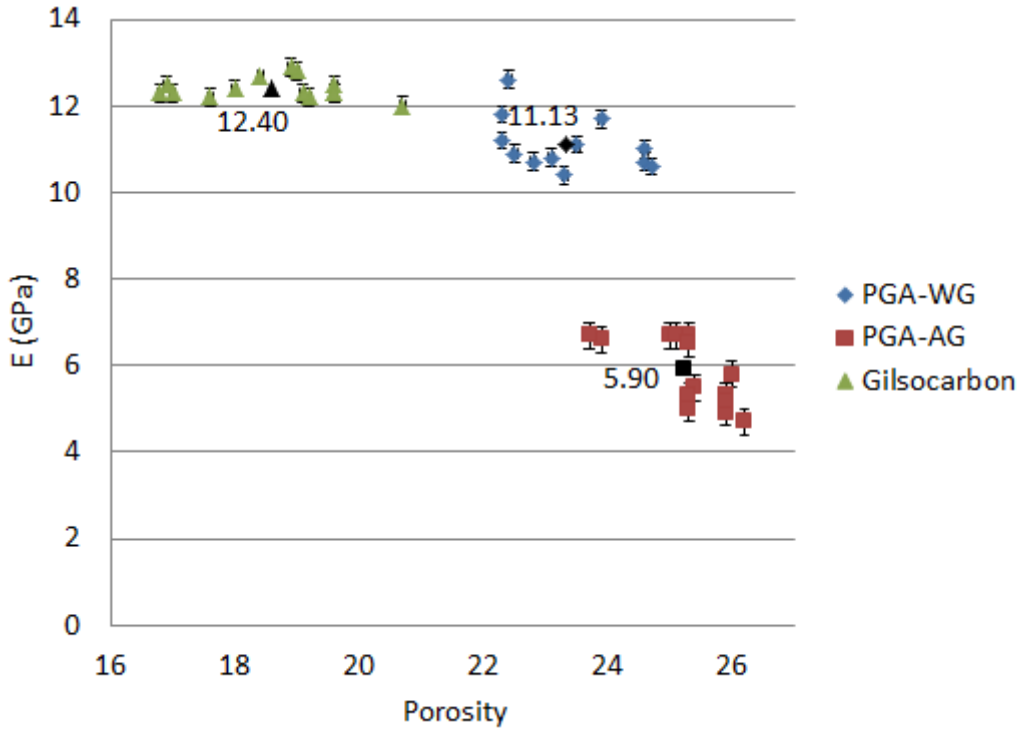

Figure 4.7 Dynamic Young's modulus (DYM) against total porosity in PGA-WG (PGA sample parallel to the extrusion direction), PGA-AG (PGA sample against the extrusion direction) and Gilsocarbon

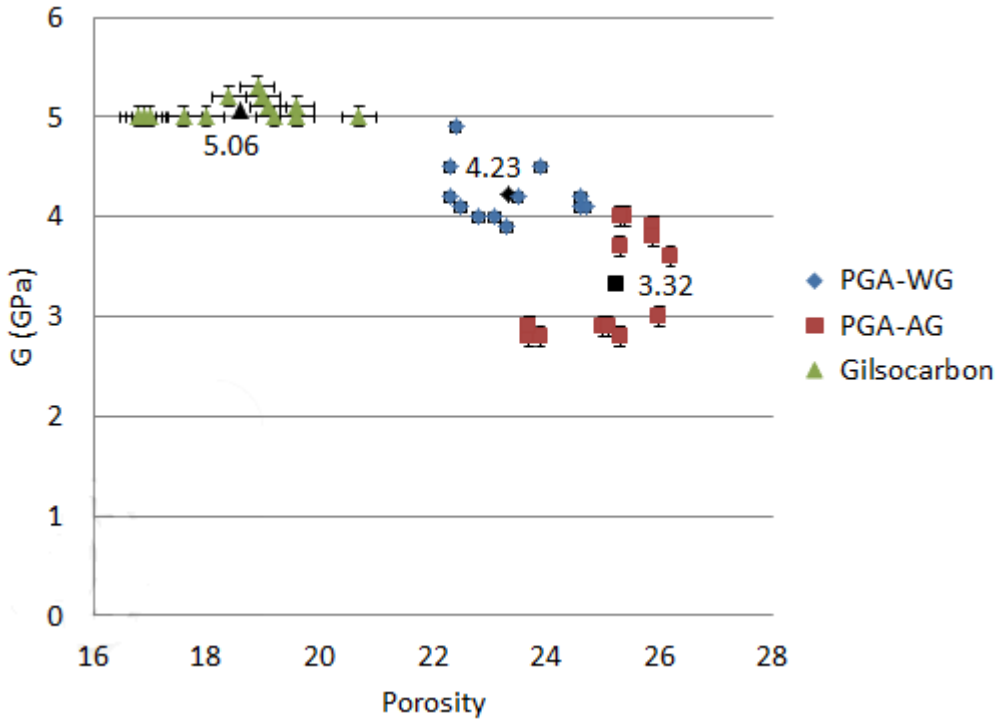

Figure 4.8 Shear modulus against total porosity in PGA-WG (PGA sample parallel to the extrusion direction), PGA-AG (PGA sample against the extrusion direction) and Gilsocarbon

4.2 High pressure loading (hydrostatic measurement)

Variation of volumetric strain of PGA-WG with hydrostatic pressure up to 60 MPa and 200 MPa are depicted in Figure 4.9. The conventional stress-strain curve for graphite aggregates under uniaxial stress have a convex upward shape [42, 56], and it is interesting that observe the resulting curve from hydrostatic compression exhibited a concave shape. The generic behaviour of the graphite aggregates under hydrostatic stress is divided into three stages: these can be marked I, II and III on the volumetric strain curve for the 200 MPa experiment in the Figure 4.9. The stages were described in the Table 4.2

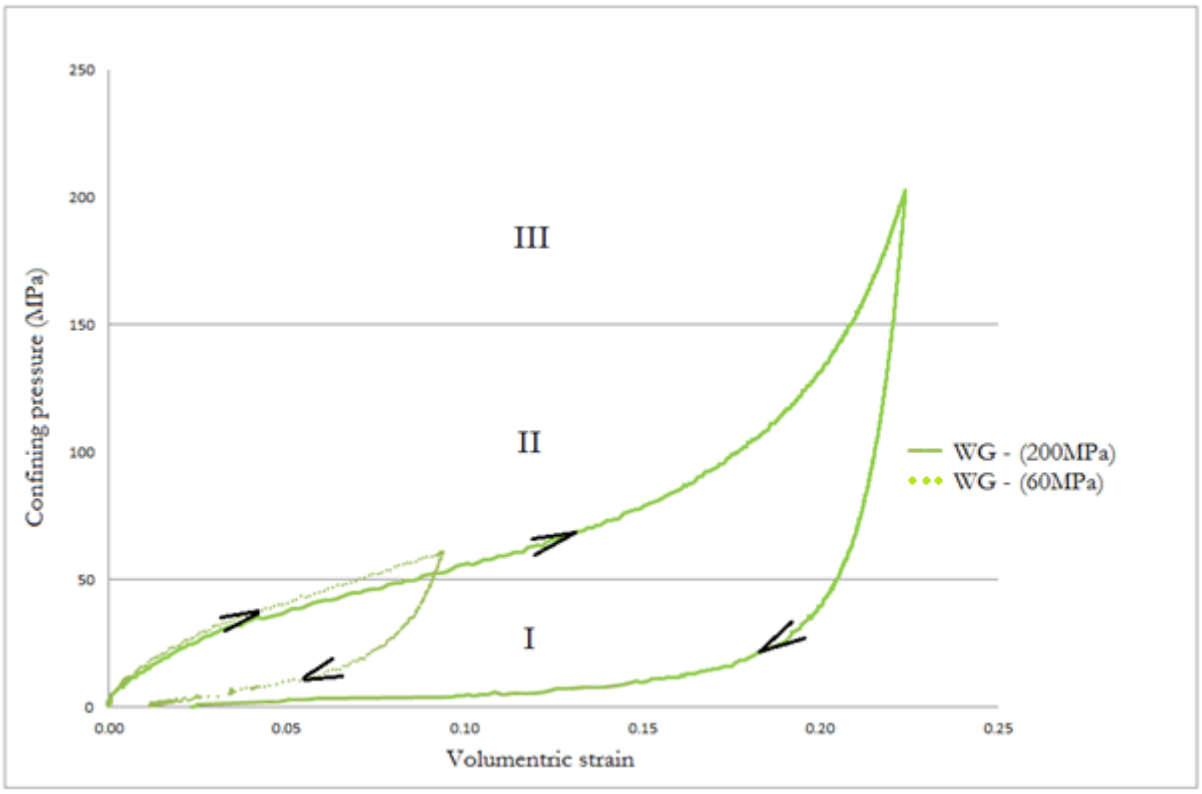

Figure 4.9 Volumetric strain (V.S.) of PGA-WG- J4 and F1 during hydrostatic compression up to 60MPa (dotted line) and 200MPa (solid line). The volumetric strain was changed from negative strain to positive strain. The three stages (I, II and III) were explained in Table 4.2

When a sample is compressed, the change in length and strain are negative, but for the purpose of clarity in this work, the negative strain was changed to positive strain. In the Figure 4.9, the samples J4 and F1 were compressed, the sample sizes were reduced as the confining pressure increased. The removal of applied pressure results in a small amount of permanent strain indicating that there are some pores must have collapsed permanently during initial loading. There was a remarkable volume recovery during the release of confining pressure at ~50 MPa; for the PGA sample compressed at 60 MPa, original volume was approximately recovered, but for the sample compressed at 200MPa, 98-99% volume recovery was noted. A permanent set of 1 - 2 % was comparable with Paterson's work [54]. The postulated mechanisms for the graphite inelastic and recovery behaviour are presented in Table 4.2.

Table 4.2 Description of graphite inelastic and recovery behaviour using the volumetric strain curve

Stages	Loading	Unloading
I	The strain increased with an increasing in pressure (up to 8 %). It is suggested that there might be not enough pressure to overcome the friction between the basal plane, lower rate of pore closure with increase in pressure	Rapid volume recovery at below 50 MPa was observed. This behaviour was generic to both PGA with-grain and against-grain. It is suggested that during this stage there was enough pressure release to overcome the friction between the basal plane
II	The strain increased substantially with small increase in pressure (from 8-21 %). The author suggests that the graphite deforms and large pores close easily (i.e. lenticular and globular porosity)	From 150 to 50MPa, the material slightly recovered 1% of its volume after loading.
III	The strain almost level off with the pressure (from 21-22 %). According to Yoda et al. [56], this behaviour can only be observed in elastomer material e.g. rubber. Majority of graphite pores closed at high pressures (approaching zero porosity); therefore for further increase in pressure makes the graphite less deformable and grain compression dominate. The graphite behaviour approaches hypothetically non-porous graphite.	Many pores disappeared; the material held on to its strain (22 %), even though the confining pressure was released, the material volume remains constant.

The behaviour of graphite under hydrostatic loading can also be explained further by using micromechanical model such as spring and frictional element diagram shown in the Figure 4.10, where K_a and K_c represent the two springs and F represents the frictional element ($K_a \sim K_c$) and ($K_b \ll K_a$).

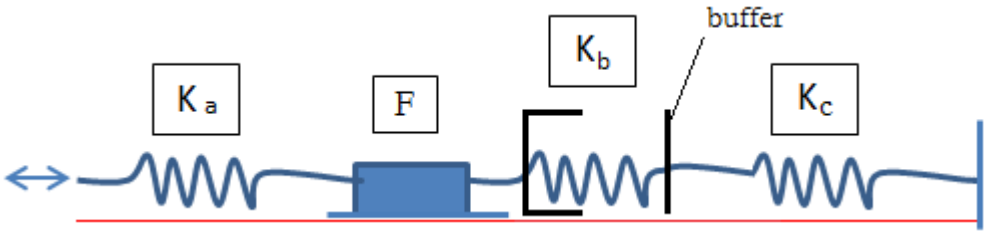

Figure 4.10 Spring/frictional element diagram

Considering the loading behaviour of graphite samples (i.e. sample F1 in the Figure 4.9), it was initially stiff then it became less stiff after a few percent volume strain and then after about 20% the material stiffens up again.

Conceptually it was envisaged that during the initial loading, the graphite was initially stiff as large, equant pores are not closing. In the model above the initial loading represent compression of spring K_a. Once some critical value of stress is reached, to overcome either friction on basal planes or break some van der Waal's bonds between basal planes, then the frictional element (F) will slide, the spring K_b hit the buffer (combination of K_a and K_b), allowing the less-stiff K_c to be loaded which represents the poroelasticity of the smaller inequant cracks and pores. Once all the large pores have closed (represented by the limited displacement capacity of K_c), K_c will no longer be able to accommodate any strain therefore any further strain will have to be accommodated by further displacements on the stiffer K_a which represents the elasticity of the graphite with remaining open microcracks and the collapse of the more equant larger pores.

During unloading, the slope of the stress/strain curve was steep and in the model above, the spring K_a was been unloaded without sliding on the frictional element and K_c does not unload. Once the stress difference on either side of the frictional element had reached a critical value, it started to slide unloading K_b and finally unloading K_c. One possibility of explaining this is when the equant porosity closes, basal planes of graphite are placed together and they bind together with weak van der Waals bonds. They only break on release of the pressure when there is critical stress on them. One of the ideas for interpreting the hysteresis was to see whether this was possible with the energy lost in the process.

Mechanical workdone is the area under stress-strain curve. Work was done on the sample as it was compressed. This energy was stored as strain energy. Since the material showed hysteresis behaviour during unloading, only some of this energy was recovered. In the Figure 4.11, the

energy lost during loading and unloading was calculated as ~155 J. This energy must have been dissipated through:

- creation of new surface area by rupture and sliding of the basal planes (i.e. crystallites reorientation resulting to porosity closure and opening) as suggested by Abrahamson [117]
- dissipation through plastic deformation and defect creation (creation of basal plane dislocations)
- heat lost (ΔT): the heat lost was calculated (using thermodynamic equation; $Q = mc\Delta T$) to be ~308.2 K/35 ^{O}C

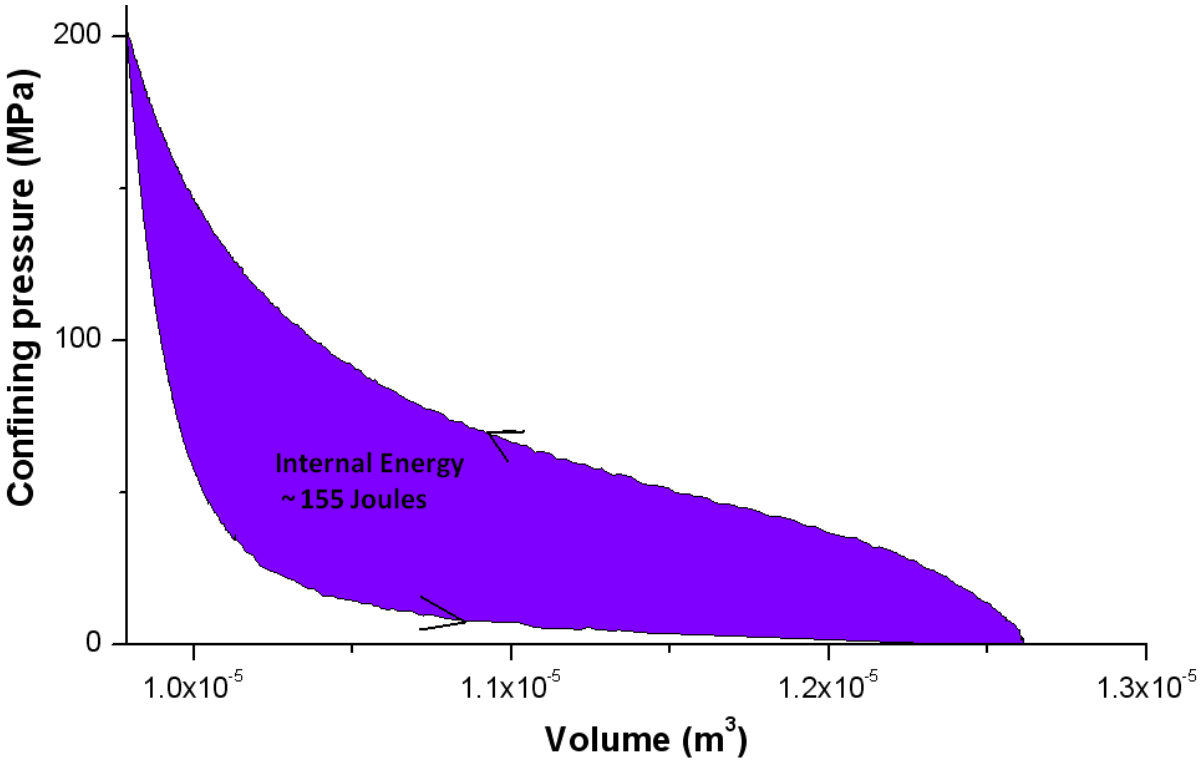

Figure 4.11 Energy lost in the stress- strain curve of sample F1

The work done per unit volume to deform a material from a stress free reference state to a loaded state is the strain energy density of that material. The strain energy density was calculated as 12.3 MJm^{-3}. In this work, the effect of the loading on the graphite microstructure was examined.

PGA-WG and PGA-AG samples were hydrostatically compressed up to 60 MPa in order to study the effect of graphite crystallite orientation on their compressibility. PGA-WG axial strain

was less than circumferential strain as shown in the Figure 4.12, but PGA-AG showed opposite behaviour. This behaviour was due to the preferential alignment of the graphite grains in different direction (i.e. PGA-WG: parallel to extrusion direction, therefore it became easier to close the pores perpendicular to the circumferential strain gauge, whilst vice-versa for PGA-AG). The volumetric strain is independent of the alignment of the specimen. The PGA-AG was taken to higher pressure than PGA-WG, therefore the volumetric strain of PGA-AG is larger than PGA-WG. In Figure 4.12, the true error was calculated using error propagation between extreme individual observations in strain was represented with the error bars, this serves as a form of reliability of the observed strain. The uncertainty in the confining pressure was calculated as ± 150 - 155 Pa, which was too small to be included in Figure 4.12.

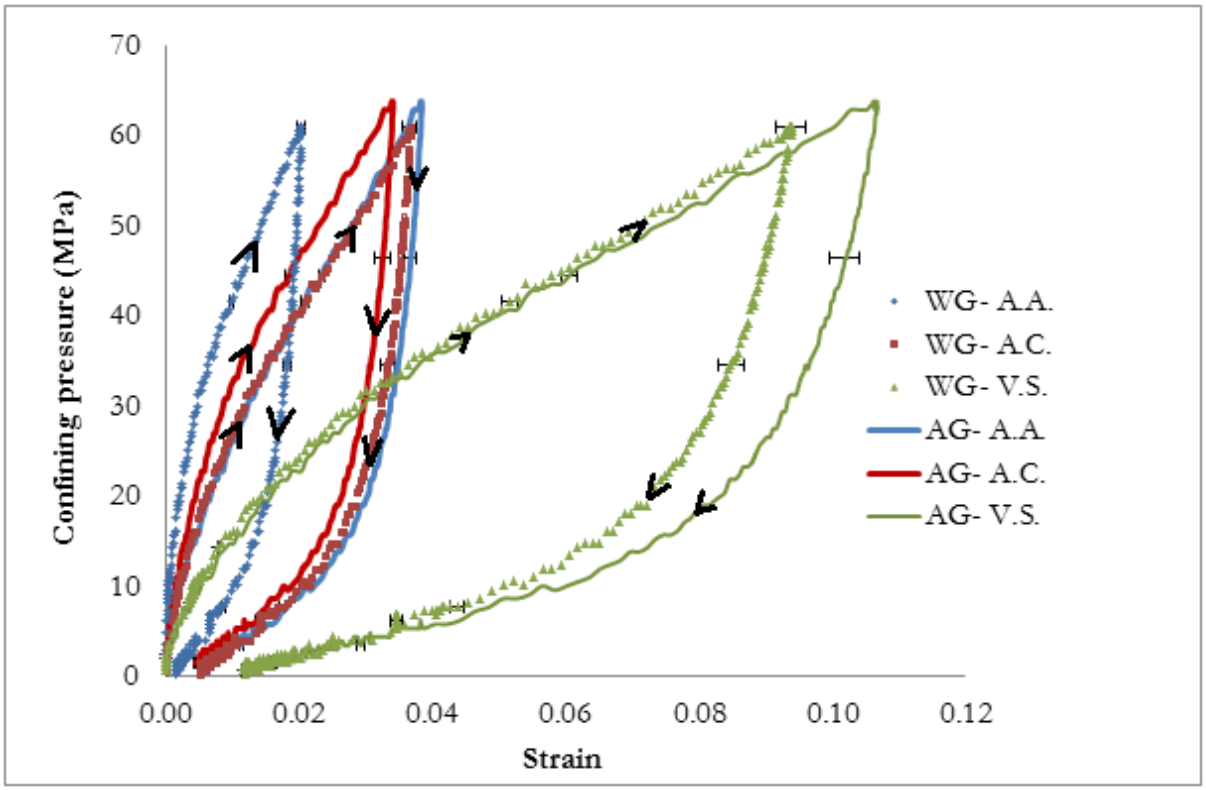

Figure 4.12 The history of axial, circumferential and volumetric strain during hydrostatic compression of PGA with grain-J4 (dotted line) and PGA against grain-F4 (solid line) at 60 MPa. A.A- Average axial strain, A.C- Average Circumferential strain, V.S- Volumetric strain

The schematic diagram in the Figure 4.13 was proposed in order to interpret the result in the Figure 4.14 in term of porosity closure. The two dimensional schematic diagram in the Figure 4.13 shows the alignment of elliptical pores (i.e. lenticular cracks) parallel to the basal plane and other randomly oriented circular porosity (i.e. globular pores) in the binder. Polycrystalline graphite consists of binder, grains and porosity [23, 25, 41, 79]. Lens shaped pores are

preferentially aligned parallel to the direction of extrusion in the PGA-WG. It was noticed that under hydrostatic compression, that samples whose axis was parallel to the extrusion direction compressed more in the circumference direction than the axial direction, this was due to closure of elliptical pores that are preferentially oriented parallel to the sample axis. With sample whose axis are perpendicular to the extrusion direction, axial strain was higher than the average circumferential strain and there was also slightly anisotropy in the circumferential strain. Resulting in slightly lower circumferential strains recorded in strain gauges glued parallel to the extrusion direction. The volumetric strain of the samples cored in the two directions under hydrostatic compression is the same just as expected.

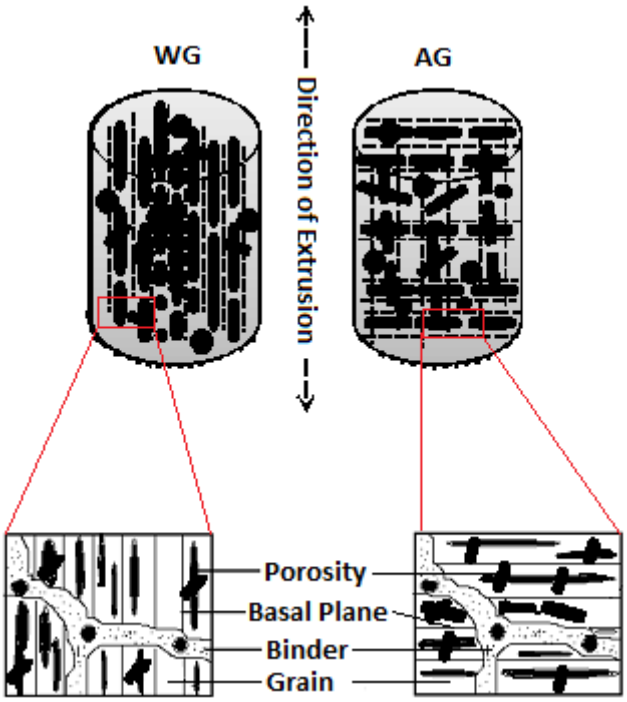

Figure 4.13 Schematic diagram of PGA-WG and PGA-AG, the three dimensional schematic are proposed by the author and the two dimension schematic are adapted from Eto et al. [118],

The Figure 4.14 shows the volumetric compression behaviour of Gilsocarbon, PGA-AG and PGA-WG nuclear graphites under hydrostatic load up to 200 MPa. The figure shows the experimental data obtained upon hydrostatic loading and unloading respectively.

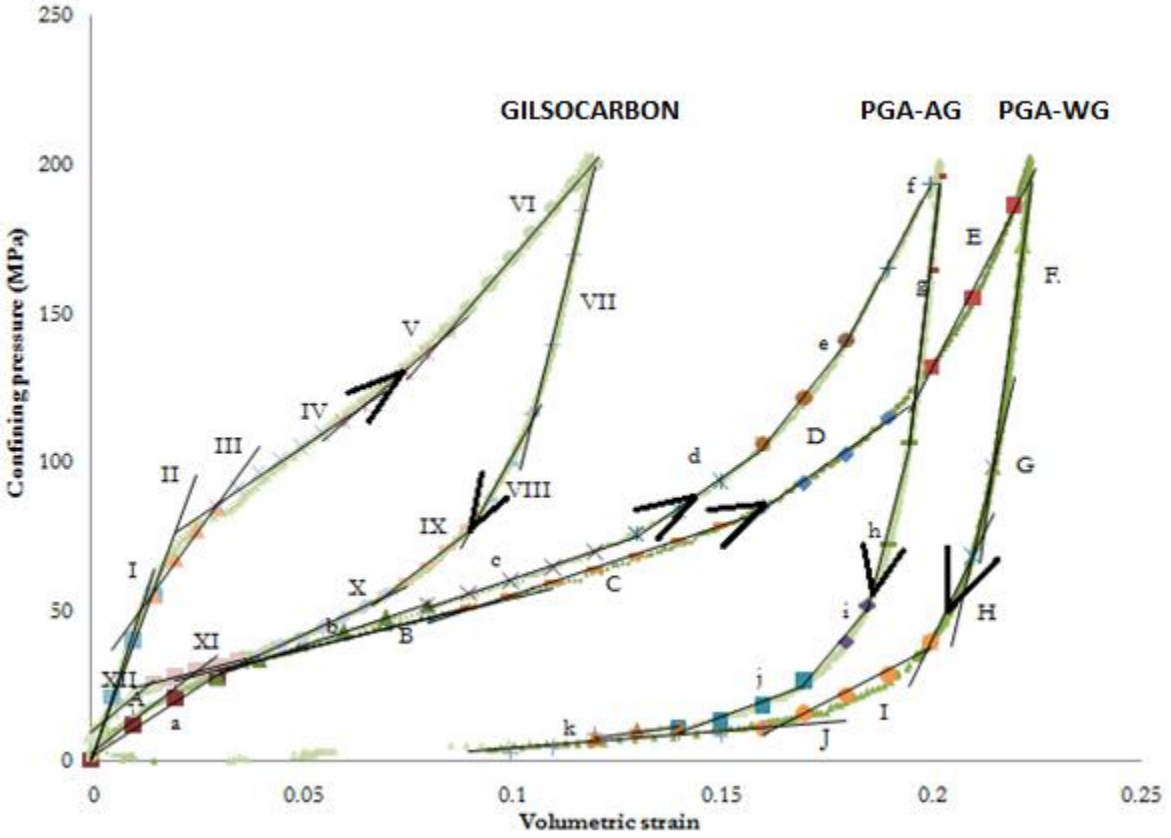

Figure 4.14 Volumetric behaviour of Gilsocarbon (E2), PGA AG (F5) and WG (F1) under hydrostatic stress (200 MPa) states

The variation of volumetric strain with hydrostatic pressure up to 200 MPa are shown in Figure 14. The data have been divided up into a number of segments within which slope on the Figure 14 was roughly constant (I-XII, A-J and a- k). From the slope the average bulk modulus within each pressure range was estimated. The magnitude of permanent strain in the PGA samples was higher than the Gilsocarbon, resulting from the fact that the compressive strength of Gilsocarbon (70 MNm^{-2}) was higher than the compressive strength of PGA (27 MNm^{-2}) [116]. The strain in the conventional uniaxial stress-strain curve is much lower than the strain in the hydrostatic stress-strain curve in this work. A conventional stress-strain curve under uniaxial stress exhibits a convex shape (probably because of less pore closure), while the resulting curve under hydrostatic stress exhibits a concave feature beyond a strain of 0.01 for Gilsocarbon and 0.15 for PGA. Porosity closure in graphite was the main strain accommodation mechanism [54, 56]. At the maximum applied pressure, the change in volume of Gilsocarbon, PGA-AG and PGA-WG graphites are about 13, 20 and 23 % respectively. When compared to the starting porosities of 20 % for Gilsocarbon and 26 % for PGA it can be seen that the majority of the porosity has been closed by the application of 200 MPa confining pressure.

In Figure 4.14, Gilsocarbon seems not to display stage II mentioned in the Figure 4.9, unlike both PGA samples where stage I, II and III appeared. This might be due to less porosity volume fraction in Gilsocarbon compared with PGA.

The bulk modulus of Gilsocarbon was calculated using Equation 4.1, where $\boldsymbol{K}$, $\boldsymbol{E}$ and $\boldsymbol{v}$ are bulk modulus, Young's modulus and Poisson's ratio respectively. Using the DYM value at atmospheric pressure in the Table 7.1, the bulk modulus of Gilsocarbon was calculated as 6.11 GPa, and the observed value was in good agreement with this.

$$K = \frac{E}{3(1-2v)} \qquad \textbf{(4.1)}$$

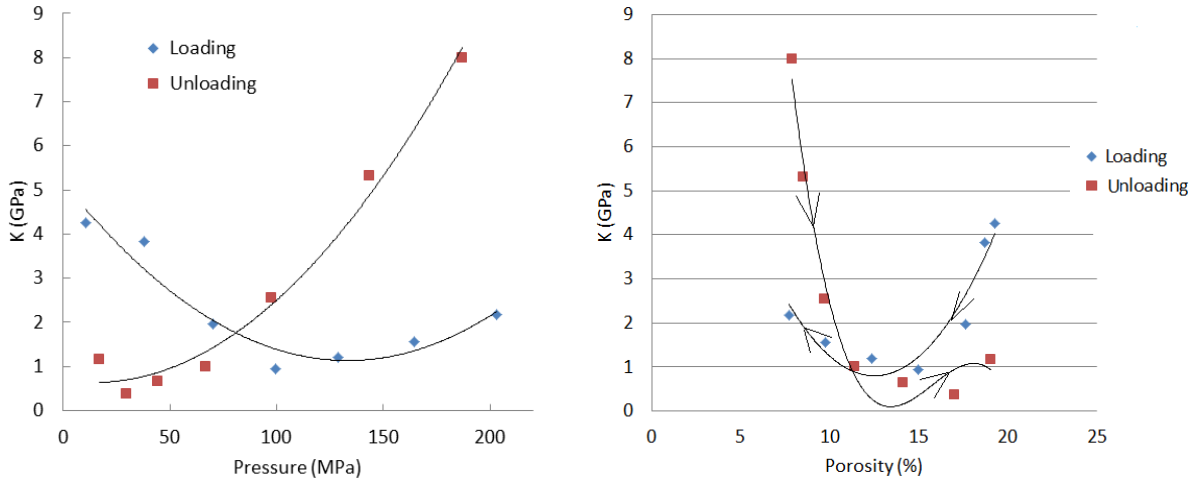

a) Average bulk modulus against confining pressure

b) Average bulk modulus against porosity

Figures 4.15 Gilsocarbon (E2) graphs of average bulk modulus against a) pressure and b) porosity

The change in average bulk modulus of Gilsocarbon as porosity changes is shown in Figure 4.15. During the initial loading, there was a lower rate of pore closure (from 19.3 % to 15 % porosity), as pressure increased, resulting in a decrease in bulk modulus to 1 GPa until a sudden change in direction was experienced at higher pressure i.e. from 100 MPa. Above 100 MPa, there was an increase in bulk modulus to 2.2 GPa; this is due to closure of the large porosity. At maximum applied pressure (200 MPa), the volumetric strain in Gilsocarbon is 12.5 % (Figure 4.14), which suggested that majority of porosity would have closed (13 % closed). In this state; the graphite is behaving like lower porosity graphite. According to Barsoum et al. [119], during graphite loading, there is an accumulation of local dislocations resulting in formation of kink bands. Since dislocations are confined to the basal planes, they cannot entangle and can thus move reversibly

over relatively large distances resulting in the dissipation of energy during each cycle (loading to unloading) [119].

In the spring model shown in Figure 4.10, during the initial stage of unloading, the force on both spring K_a, K_b and K_c are equilibrium, further unloading makes K_a extend first until there is a large enough difference in force on either side of the frictional element to make it slide. Once it slides, K_b can be unloaded and then K_c unloaded subsequently. In the nuclear graphite, it was assumed that during unloading, the basal planes which were held together due to the dislocation pile up, were released gradually until it reaches critical pressure, where the sample almost recovered its initial volume. This was why there was a large difference between the average bulk modulus at maximum pressure after loading (2.2 GPa, this is inelastic) and before unloading (8 GPa, this is elastic).

By using a nano-indentation technique, Berre et al. [120] measured the Young's modulus and Poisson's ratio of hypothetical non porous graphite to be 15 GPa and 0.2 respectively [120]. The resultant calculated bulk modulus of non-porous gilsocarbon graphite is 8.3 GPa. In this work, the average bulk modulus of the resulting Gilsocarbon curve upon unloading from the maximum pressure (200 MPa) appears to be 8.1 GPa. The discrepancy between the observed bulk modulus upon unloading and calculated bulk modulus seems to be insignificant. During unloading, initially only internal distortion within graphite crystals is unloaded, then once the stress dropped below a certain value closed pores started opening gradually, resulting in a decrease in bulk modulus to 1 GPa. At 50 MPa a sudden rise in K was observed, this might be due to the fact that the reopening of the larger pores forced the large population of microcracks to close, therefore increasing in bulk modulus. This could also mean that maybe the frictional element has stopped sliding so easily, therefore the poroelastic element was not offloaded so much but more of the intracrystalline elasticity was unloaded. PGA did not show this behaviour.

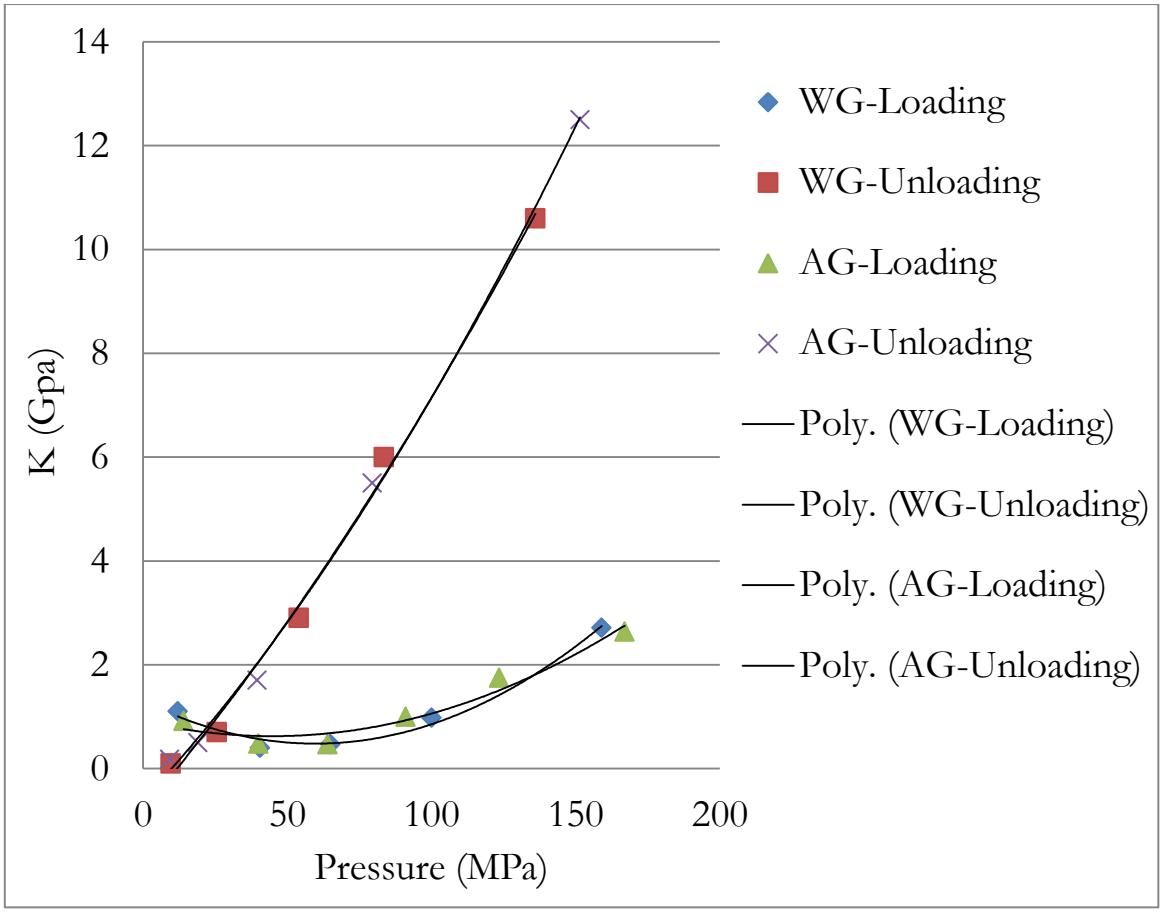

Figure 4.16 PGA WG (F1) and AG (F5) average bulk modulus against confining pressure

The deformation behaviour of both PGA WG (F1) and AG (F5) in the Figure 4.14 was evaluated in the Figure 4.16 in a similar manner to the Gilsocarbon graphite mentioned above in the Figure 4.15. Gilsocarbon is denser than PGA graphite, but PGA-AG and PGA-WG samples have the same density, yet the apparent average bulk moduli of each PGA-AG and WG sample was ~1 GPa. The loading history shows that the difference between the average bulk modulus of PGA AG and WG during loading seems to be insignificant since they are the same material.

During loading of PGA a sudden change in slope was observed at much lower pressure (50 MPa) unlike Gilsocarbon. This suggested that the threshold stress to activate pore closure in Gilsocarbon is higher than in the PGA samples. This may be due to the crystallographic preferred orientation of PGA, which means that when a pore closes by sliding on a basal plane it is more likely to be compatible with closure of other pores in similar orientations. The apparent bulk modulus of the resulting curves upon unloading from the maximum pressure were similar, and reduced from 12.7 GPa to 0.3 GPa, this value (12.7 GPa) was higher than the bulk modulus of graphite, this might be due to the LPO and preferred pore orientation. If pore collapse is

mainly parallel to the c-direction, if inhibited by the friction component then compressibility has to be accommodated more within the basal planes which are much stiffer.

4.2.1 Combined hydrostatic and differential stress (axial deformation)

A triaxial compression test is generally conducted in two phases; a hydrostatic compression phase and a differential phase. During the hydrostatic phase, the specimen is subjected to isotropic compression, while measurements of axial and radial deformations are made. The differential phase of the test is conducted after the desired confining pressure has been reached during the hydrostatic phase. While holding the desired confining pressure constant, the axial load is increased. The total history of the volume change during the experiment is shown in Figure 4.17.

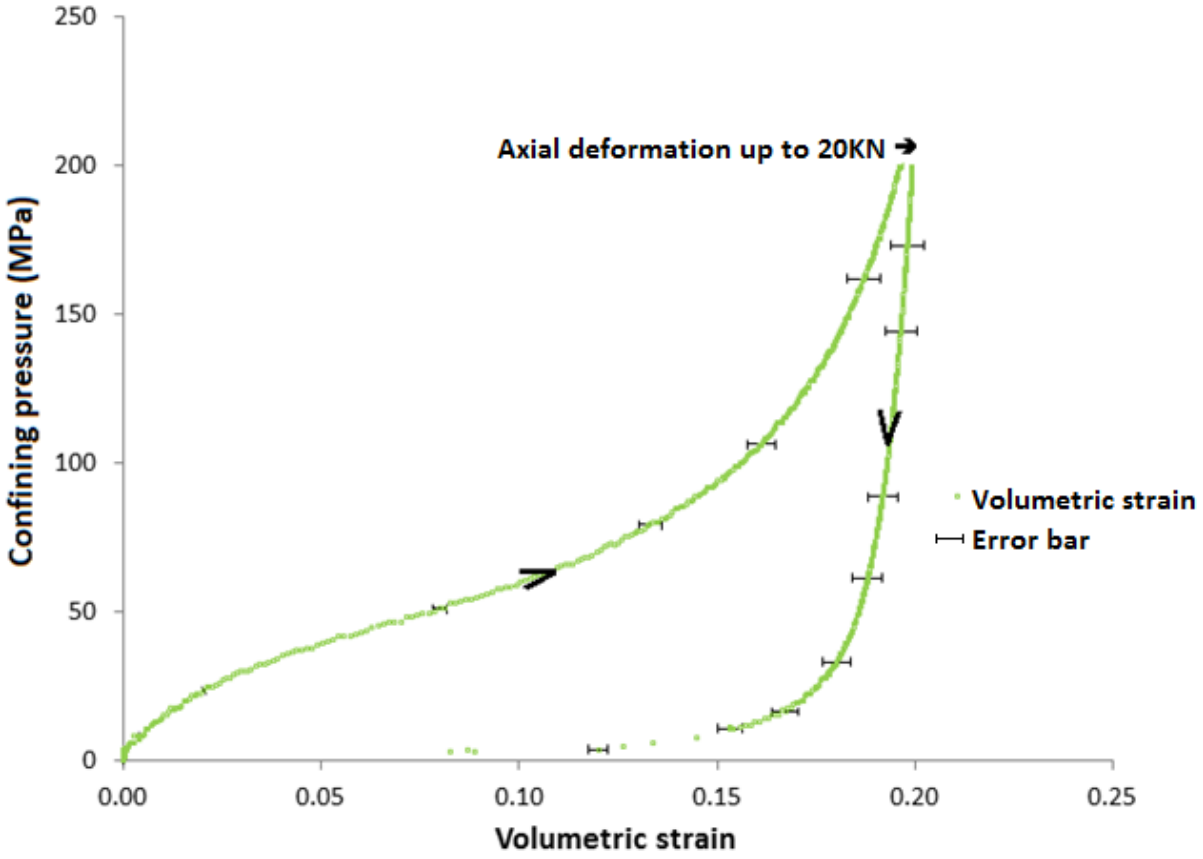

Figure 4.17 Total history of PGA-AG (F6) volume change during experiments (increase in confining pressure, followed by axial deformation, and then confining pressure unloading)

After the volume decrease on applying confining pressure up to 200 MPa, the sample is then deformed axially; there was a further volume decrease during an additional 12.5 % axial strain at fixed confining pressure. A large increase in volume occurred during the release of confining pressure (Figure 4.17).

4.2.2 Axial deformation

In the axial deformation curve, the axial strains represent a contraction and the circumferential strains represent an expansion. The circumferential strain curves in Figures 4.19-4.21 show strain around the sample circumference for the applied stress along the axial direction (referring to the experiment listed in **Table 3.4**). At low stresses, compaction occurs. This stage was quite brief, immediately after compaction the elastic-plastic deformation follows. There is limited deformation at the elastic region. If the load were to be released in the elastic region, it is suggested that the strain might be recoverable up to about 2/3 the elastic region.

In the inelastic deformation, as the stress increases, the axial strain begins to show nonlinear behaviour, it is suggested that the beginning of this stage, there was a competition between **closure** of pores oriented roughly perpendicular to the sample axis and **opening** of pores roughly parallel to the sample axis. Initially the closure of cracks overcome the opening of cracks but as the stress increased more pores opened up parallel to the axis which had a dramatic effect on the circumferential strain, resulting to production of **dilatancy**. The behaviour was different at higher pressure. The sample is only start dilating when the slope of the volumetric strain graph goes positive. The dilatancy results in a net volume expansion of the sample. The higher the stress, the more granular microcracks grow, the strains at higher stress are not recoverable. The typical confined stress-strain curve behaviour is shown in the Figure 4.18.

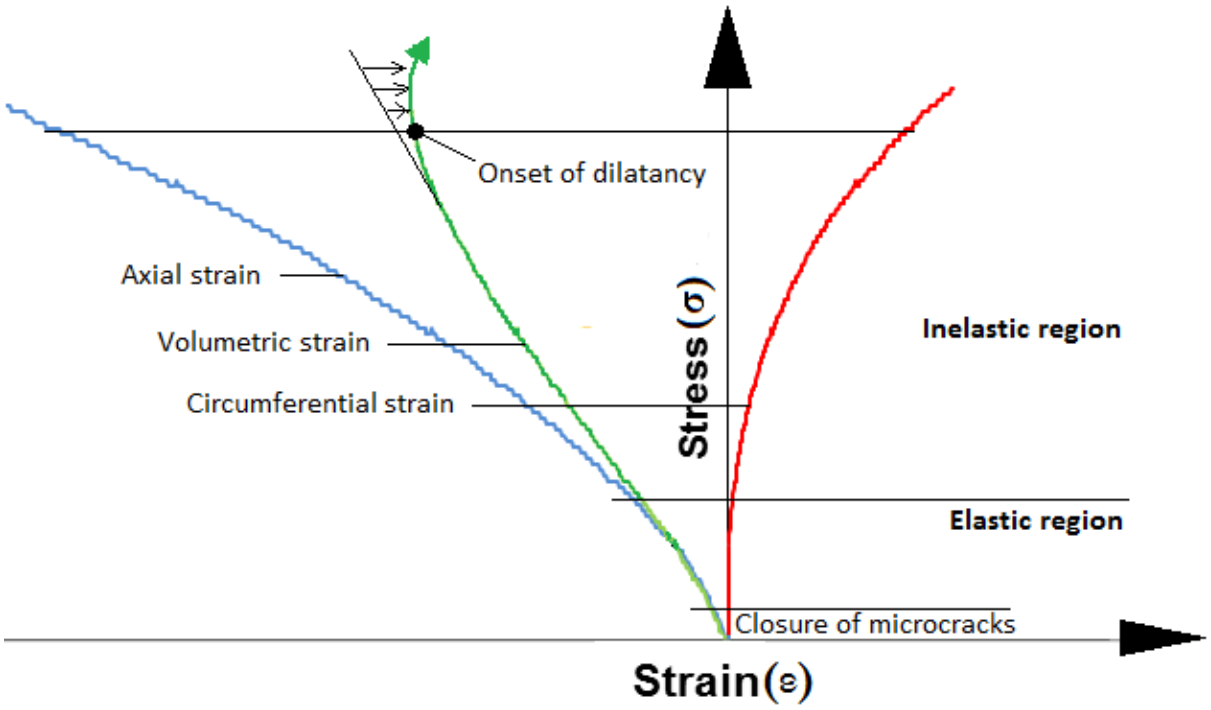

Figure 4.18 Schematic stress-strain curves for the confined axially symmetric shortening of graphite

The Figure 4.18 stress-strain curve can also be explained using the micromechanical model. At the initial loading stage, the slope was stiff until a critical stress was reached, and then the material became less stiff due to the changes in the microstructure caused by an increase in force. This is applicable to both axial and circumferential strains.

The confined average axial, circumferential and volumetric stress-strain curves for PGA-AG samples in compression are shown in the Figures 4.19, 4.20 and 4.21. The axial strain represent contraction and circumferential strain represent expansion. In all cases average axial and circumferential strains were measured as a function of applied load before failure. Average volumetric strain was measured or calculated from the combined average axial and circumferential strains as shown in the Equation 4.2. The form of the stress-strain curve is consistent with numerous experimental data sets for graphite [42]. For small strains (where ε^2 « ε) the volumetric strain is given by:

$$\varepsilon_v = \varepsilon_1 + \varepsilon_2 + \varepsilon_3 \qquad (4.2)$$

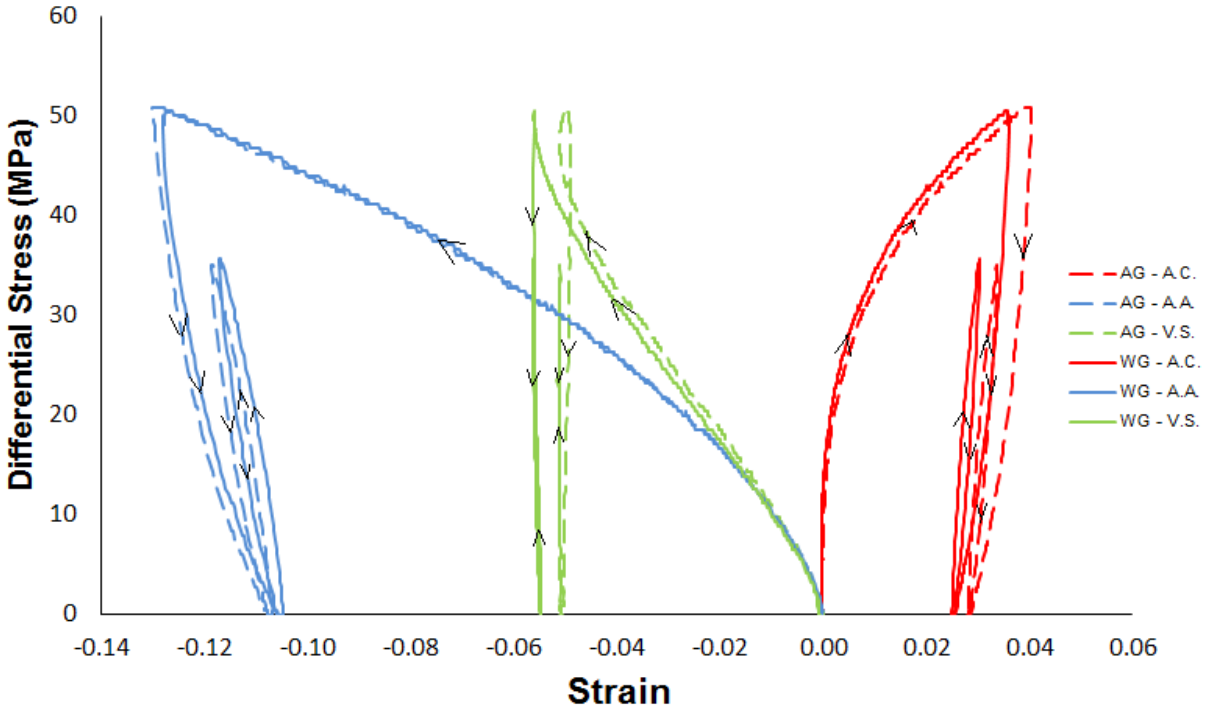

Figure 4.19 Axial deformation tests of PGA-WG (F2) (solid lines) and PGA-AG (F7) (dotted lines) samples at CP of 60 MPa and both taken to maximum differential stresses of 50 MPa (A.A. - Average axial strain, A.C. - Average circumferential strain, V.S. - Volumetric strain)

As the stress increased the graphite pore spaces are closed due to the porosity orientation roughly perpendicular or parallel to the sample axis and the volume is seen to decrease, the grain to grain contacts becomes stressed or stiffer. This region is quickly passed as the stresses for new fracture development to occur. This marks the onset of dilatancy in the sample. The onset of dilatancy can be easily observed from the behaviour of volumetric strain.

It was surprising to see that the PGA-AG and PGA-WG have such similar behaviour as shown in the Figure 4.19, considering the anisotropy of the DYM and the differences in the axial and circumferential strains in the hydrostatic compaction experiments. However there are still some differences in the behaviour of both samples.

Referring to the Figure 4.13, for PGA graphite, initial pores tend to be preferentially arranged parallel to the direction of extrusion, therefore when axial load is applied perpendicular to the extrusion direction, the porosity will be more easily closed as the pores are preferentially oriented perpendicular to the maximum compression direction ($\boldsymbol{\sigma_1}$). As shown in Figure 4.19, it was suggested that PGA (AG) was slightly less stiff than PGA (WG) during axial deformation.

During unloading, the stress within the graphite grains reduced, and permanent strain was noticed. This strain is almost recovered on the release of confining pressure. Similar behaviour was reported in previous work [42, 52].

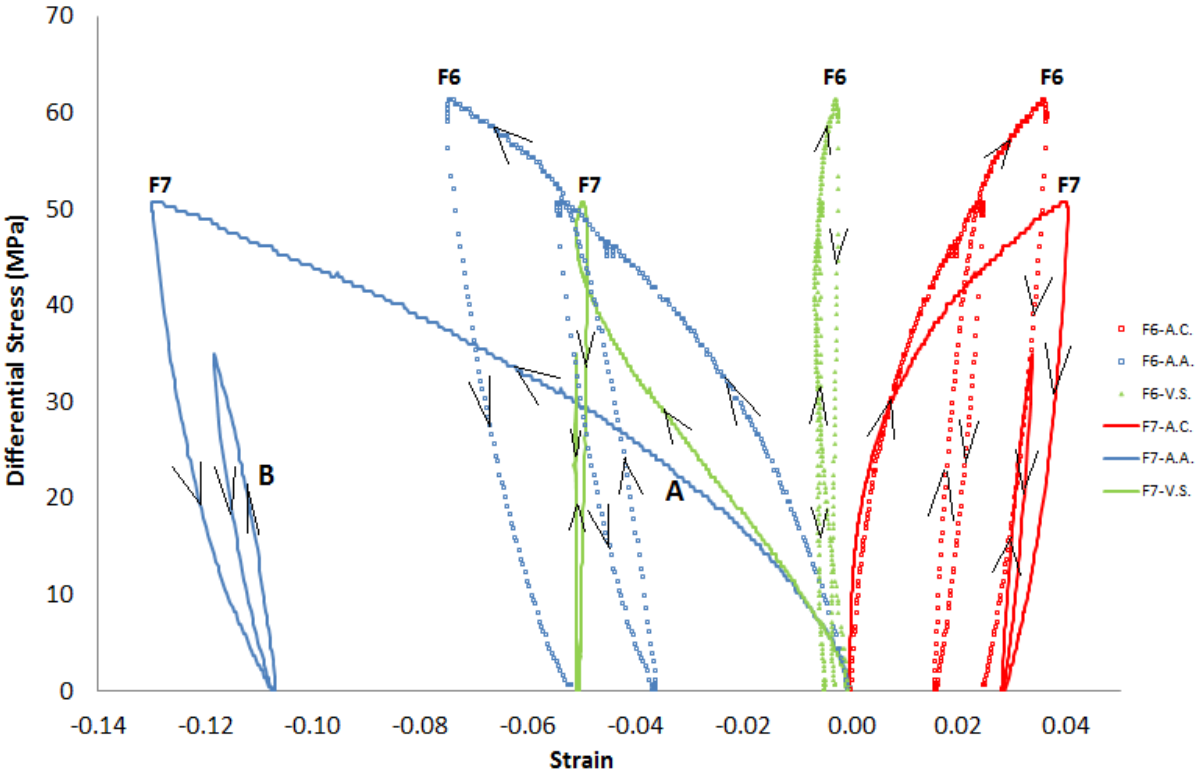

Figure 4.20 Axial deformation tests of two PGA (AG) samples, one at CP of 60 MPa – F7 (solid lines); maximum differential stress of 50 MPa and another at CP of 200 MPa – F6 (dotted lines); maximum differential stress of 62 MPa (A.A.- Average axial strain, A.C.- Average circumferential strain, V.S.- Volumetric strain). A and B represent the slope of the first and second axial loading of F7. The test conducted using samples F6 and F7 are listed in Table 3.4

The "permanent" strain whilst under confining pressure was observed which increased with stress attained, as shown in Figure 20. The generic behaviour of both samples indicated that there is more axial contraction than circumferential expansion. The volumetric strain at 60 MPa confining pressure (solid lines) is much less stiff than for a confining pressure of 200 MPa (dotted lines), this is due to more porosity closure during initial hydrostatic loading to higher pressure (Figure 4.20). Also it can be seen that the deformation at 200 MPa occurs at approximately constant volume (Figure 4.20).

In Figure 4.20, A and B represent the first and second loading period on the average axial strain curve. In the first loading cycle taking the differential stress up to 50 MPa, a certain amount of porosity collapsed during this loading. At 50 MPa, the sample was unloaded back to zero

differential stress. The sample deformed plastically, resulting in a permanent strain at that hydrostatic pressure. The majority of this strain was accommodated by porosity change. This means that the sample has a lower porosity and hence should be stiffer. At loading period B, the sample was reloaded up to 35 MPa, before unloading back to zero differential stress. The inelastic Young's modulus of A (first loading) and B (second loading) are 0.4 GPa and 2.63 GPa respectively. These Young's modulus values were calculated from the linear part of the curves. The difference in stiffness for low pressure samples can be explained by the reduction in porosity as seen by the volumetric strain but the high pressure samples do not change volume during the axial deformation so the porosity is constant. The stiffness change for the high pressure experiments could be explained by either or both of the following:

- ❖ despite the sample being deformed at constant volume there was pore closure in the axial direction but this was offset by the amount of pore opening in the radial direction. Thus there was a reduction in the porosity in an orientation that was easily closed by axial loading.
- ❖ the strain induced in the first loading cycle has locked in some residual internal stress that compressed the aggregate, making it stiffer.

This suggests that the material with higher porosity was less stiff and has lower Young's modulus in comparison with a material with lower porosity, as would be expected. After axial deformation, confining pressure was released. Each sample recovers almost their original volume and dimensions. The samples F7 and F6 are 1.2 % and 2 % smaller than their original volume.

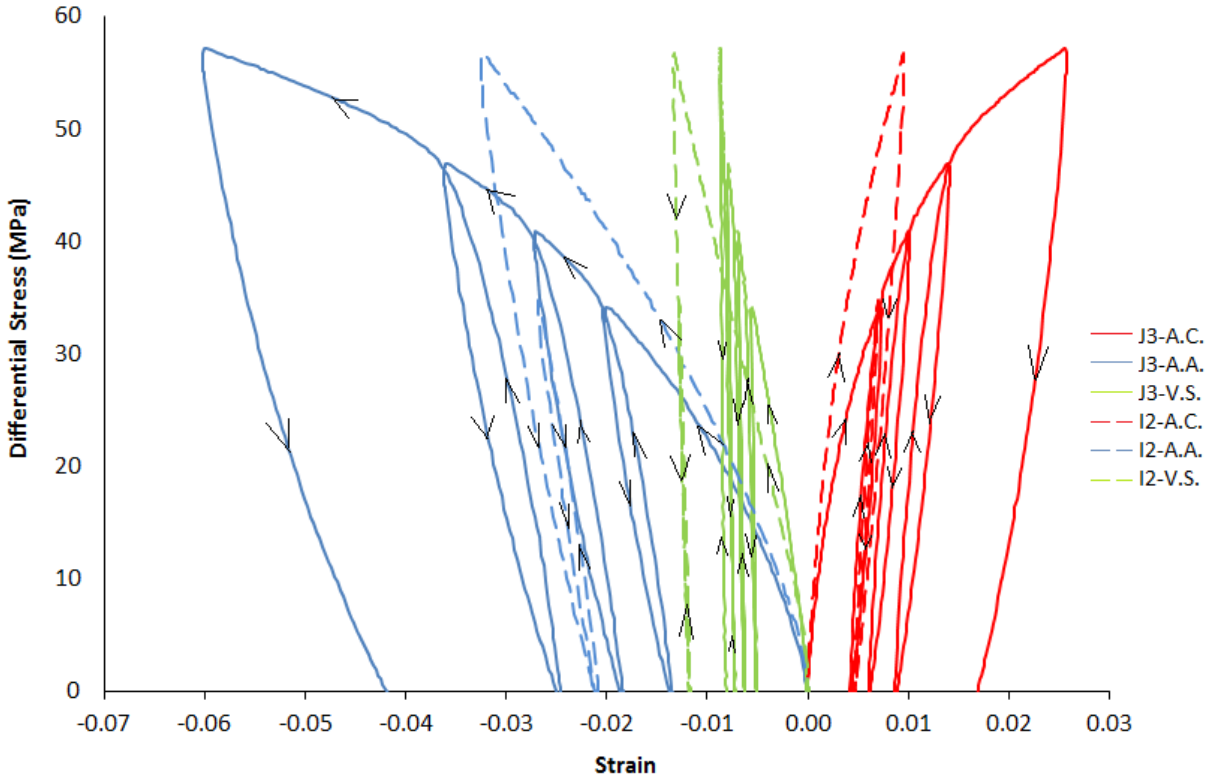

Figure 4.21 Axial deformation tests of PGA-WG (J3) (solid lines) and Gilsocarbon (I2 as shown in Table 3.4) (dotted lines) samples at CP of 200 MPa and both taken to maximum differential stresses of 57 MPa (A.A. - Average axial strain, A.C. - Average circumferential strain, V.S. - Volumetric strain)

The change in strain of both PGA (WG) and Gilsocarbon samples under axial deformation are shown in the Figure 4.21. The maximum differential stress attained during cyclic deformation was 57 MPa. As the stress increases, both Gilsocarbon axial and circumferential strain increased less rapidly than both PGA strains. At the same strain value, Gilsocarbon sample supported more differential stress than PGA samples. This suggested that Gilsocarbon was stiffer than PGA, due to lower porosity in Gilsocarbon compared to PGA as mentioned above.

4.2.3 Poisson's ratio

The ratio of circumferential to axial strain magnitudes is dependent upon the stress, yielding a Poisson's ratio (ν) [42]. In the Figure 4.22, sample (F6) at a confining pressure of 200 MPa has a lower Poisson's ratio (0.2 - 0.3) than sample (F7) at confining pressure of 60 MPa (0.25 - 0.45). Low Poisson's ratio implies volume reduction during loading. High porosity material was closer to a Poisson's ratio of 0.5 (constant volume deformation).

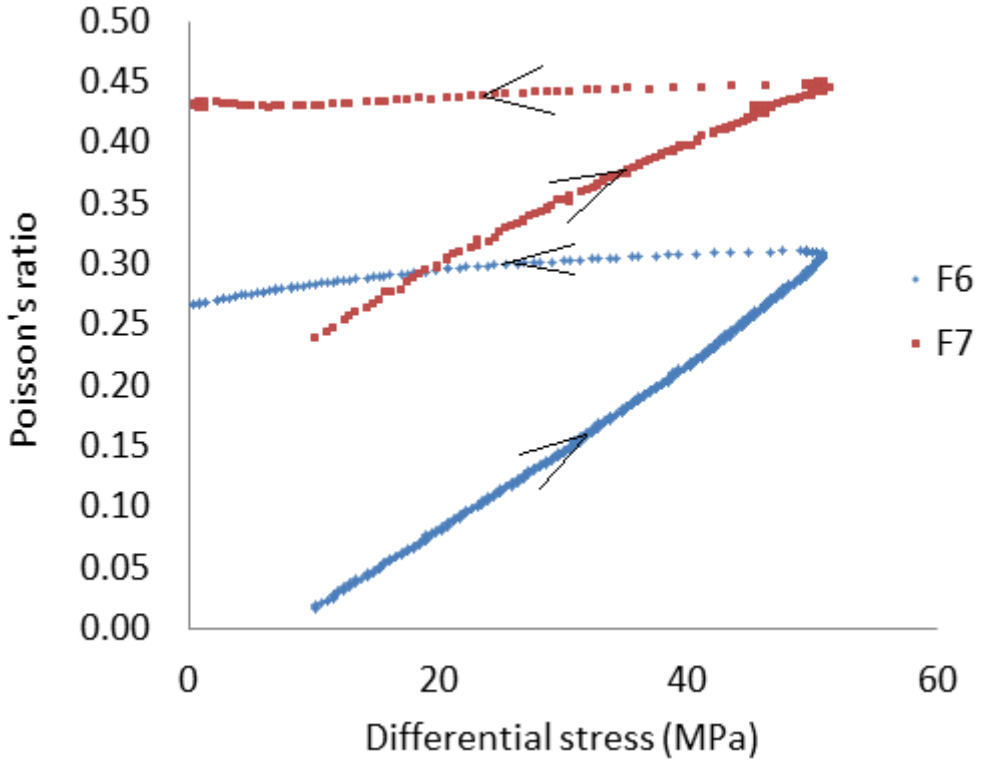

Figure 4.22 Poisson's ratios of two PGA-AG graphite samples (F7) at CP of 60 MPa and PGA-AG (F6) at CP of 200 MPa during axial deformation

4.3 High pressure ultrasonic measurements

One effect of nonlinear elasticity on strain wave propagation is that the velocity of the elastic wave is a function of the applied stress or strain on the material. The ultrasonic method used in this study to determine the bulk elastic properties of graphite is based on the measurement of the ultrasonic velocities in different directions of the sample. The velocity obtained from ultrasonic measurements of each sample was used to calculate the dynamic Young's moduli (DYM) as a function of pressure. The results show the overall bulk elastic constants at different pressures, including the influence of porosity on bulk modulus.

The main difference between the ultrasonic tests and the static tests described above is that the static method is based on the measurement of deformation induced in a material by the application of known force whilst dynamic method is based on the measurement of ultrasonic body wave velocities

The piston-sample-transducer assembly employed allowed the simultaneous measurement of compressional (P) and shear (S) wave velocities parallel to the sample axis (Z) direction as a function of confining pressure up to 200 MPa. Dynamic modulus is directly proportional to the

ultrasonic velocity (as shown in Equations 3.18- 3.20 in chapter 3) and therefore an increase in P-wave velocity implies an increase in the dynamic modulus. However as the pressure was increased, material become more stiff and therefore the density increased, this change in density during loading was taken into account by correcting the sample density, using the bulk density of the sample at zero pressure. Upon loading, there are elastic and inelastic deformation occurring whereas upon unloading, the initial slope corresponded to mostly elastic deformation

4.3.1 Hydrostatic P-wave measurements

With increasing the confining pressure, the dynamic Young's modulus and shear modulus showed a nonlinear increase and the Figures 4.23, 4.25 - 4.30 show that the non-linearity increase approaches linear behaviour above 200 MPa.

Both PGA (AG and WG) and Gilsocarbon were loaded up to 207 MPa in the seismic rig, using the P-wave and S-wave assemblies. The Figures 4.23 and 4.24 show how DYM varies with pressure for PGA and Gilsocarbon respectively. Both PGA samples show very similar behaviour, exhibiting of hysteresis and a non-linear increase in dynamic modulus (ultrasonic velocity with increasing pressure). The dependency of P-wave velocity on confining pressure was similar to the behaviour observed in previous work on graphites under pressure [112] and also on rocks [121, 122]. According to Lokajicek et al. [112], the P-wave velocity increase in graphite is mainly related to the closure of the internal pores and possibly closure of basal (cleavage) microcracks.

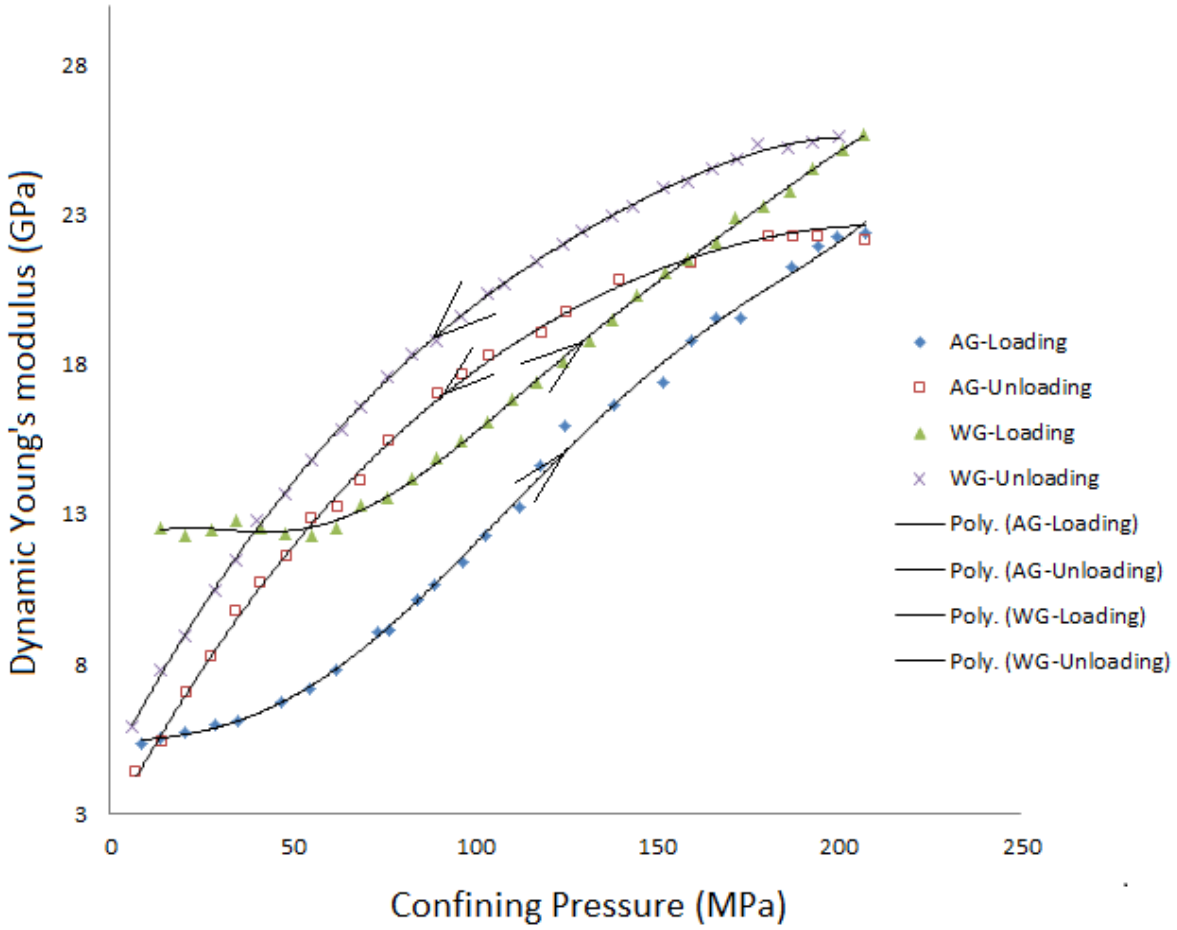

Figure 4.23 Dynamic Young's modulus with respect to the applied confining pressure on the PGA-AG (J9) and PGA-WG (J23) graphite samples

It may be suggested [21] that at low pressure (below 50 MPa), there is not enough pressure to distort the graphite grains in order to close the pores. In the hydrostatic experiments, it was known that between 50 MPa and 100 MPa there was a large change in the slope of the hydrostatic compaction curve and this corresponds to a steepening of the DYM against pressure graph shown above. Above 50MPa, the graphite becomes more stiff, less dense, hence increase in DYM. As shown in Figure 4.23, at 207 MPa, the maximum DYM of PGA-AG and PGA-WG are 22 GPa and 25.5 GPa respectively. These values are less than the both modulus of graphite single crystal c_{11} and c_{33} (1056 GPa and 36 GPa respectively) [123], and also there is a huge difference in elastic properties. This will be discussed later in Chapter 6. At 207 MPa, the DYM was still rising which indicated that the pores and microcracks in the graphite were not completely closed at this pressure (as shown in the Figure 4.24). The change in behaviour in PGA around 50 MPa was also noticed in the static loading.

At the beginning of unloading, the time of flight stayed almost the same, the sample change in length was constant due to fact that the graphite sample held on to its initial strain at 207MPa. The more pressure was released the more the DYM decreases. The hysteresis loop is much less pronounced for the DYM than for the volumetric strain. In the Figure 4.23, it can be seen PGA-AG is less stiff than PGA-WG, the time of flight of PGA-WG is shorter than PGA-AG due to the preferential alignment of the stiff basal planes parallel to the measurement direction in the PGA-WG sample.

The average DYM of PGA-AG before and after loading were 6.5 GPa and 3.3 GPa respectively, whilst the average DYM of PGA-WG before and after deformation were 10.4 GPa and 6 GPa. The value after loading is almost half of the value before loading. This might be due to change in microstructure (complex reorientation of the crystallite due to closure of pores and opening of grain boundaries).

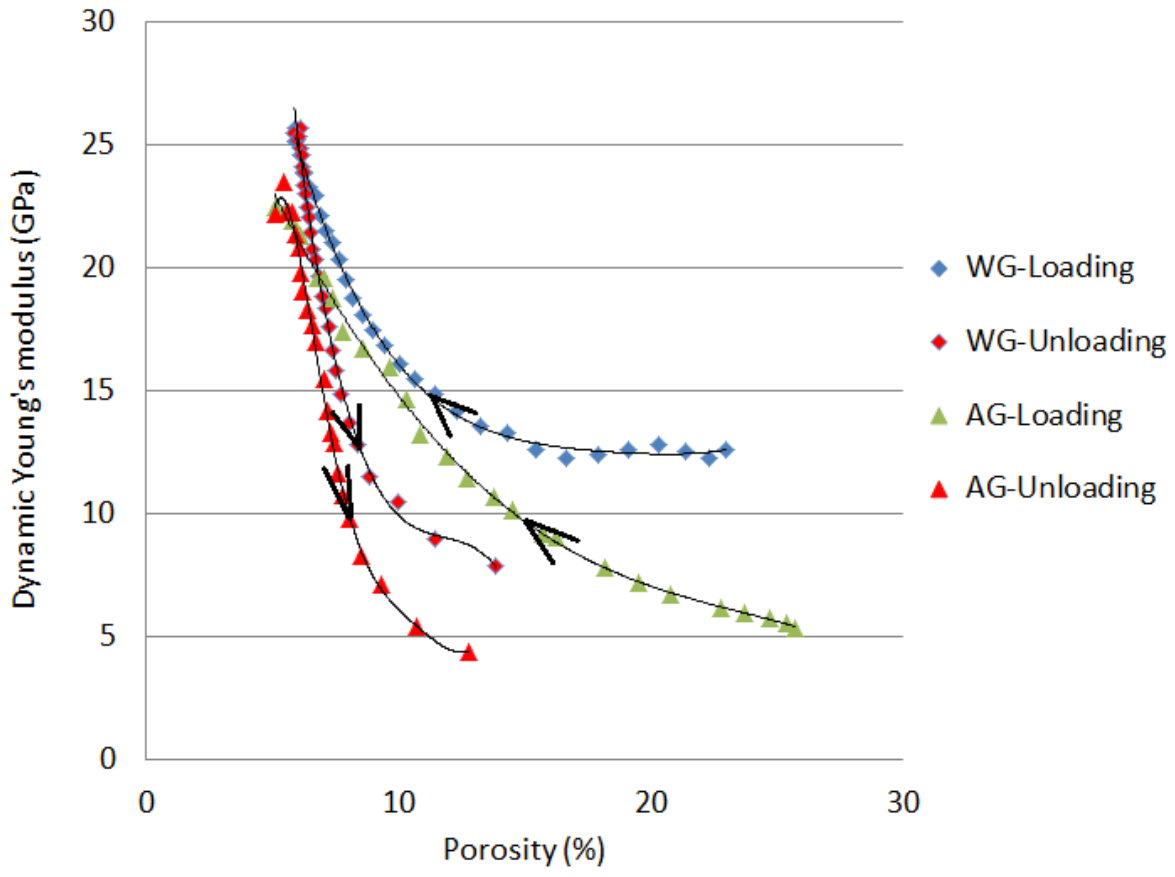

Figure 4.24 Dynamic Young's modulus against the porosity change due to pressure effect on the PGA-AG (J9) and PGA-WG (J23) graphite samples

The change in DYM against porosity change is shown in the Figure 4.24. Hysteresis loop was observed in the porosity change, which means the rate of change of porosity during loading, was different from the rate of change of porosity after loading. The porosity gradual closure was noticed at lower pressure, at higher pressure, the DYM increased sharply as the porosity closed (as expected). During unloading, porosity opened gradually as the graphite volume recovered. However not all porosity that closed during loading recovered during unloading, resulting to change in the graphite microstructure (sample became smaller in size compared with virgin sample size), hence the DYM value after loading reduced.

In Figure 4.23, slight decrease in modulus from 0 - 50 MPa, followed by a large increase in modulus behaviour is observed in irradiated graphite (see Figure 2.16 in the chapter 2).

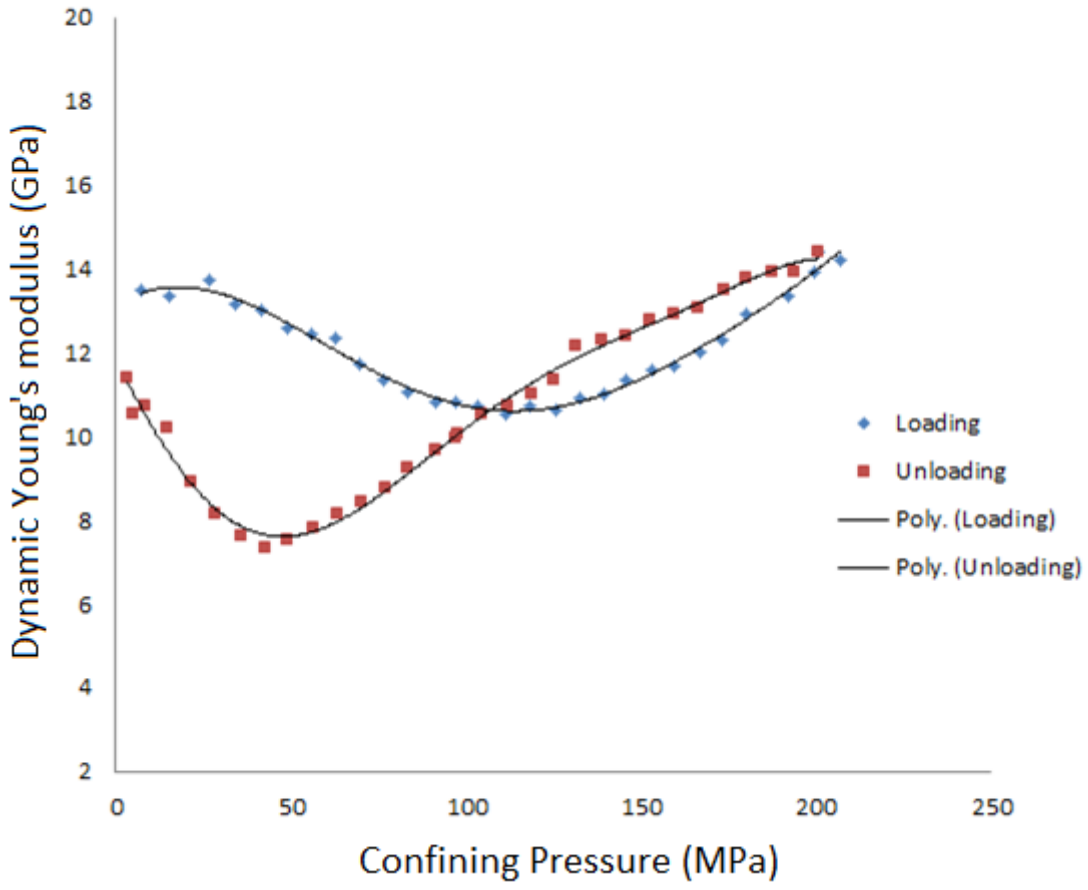

Figure 4.25 Dynamic Young's modulus with respect to the applied confining pressure on the Gilsocarbon graphite sample (I4)

The Figure 4.25, shows the different behaviour of Gilsocarbon (I4) compared with PGA. With increased pressure, the value of DYM dropped from 14 to 10.5 GPa over the first 100 MPa and

then rose to 14 GPa at 200 MPa. As the pressure increased, the grains became less stiff unlike PGA, and the DYM began to decrease, a sudden increase in DYM at 120 MPa was probably due to the fact that the grains became more stiff (enough pressure for closing larger porosity), and the DYM value was raised by 14 % of the initial DYM value at room pressure (12.4 GPa). During unloading, the DYM decreased and the sudden increase in DYM was experienced at 50 MPa, similar to the sudden volume recovery experienced at 50 MPa. The value of the residual DYM was 8 % less than the initial DYM value at room pressure.

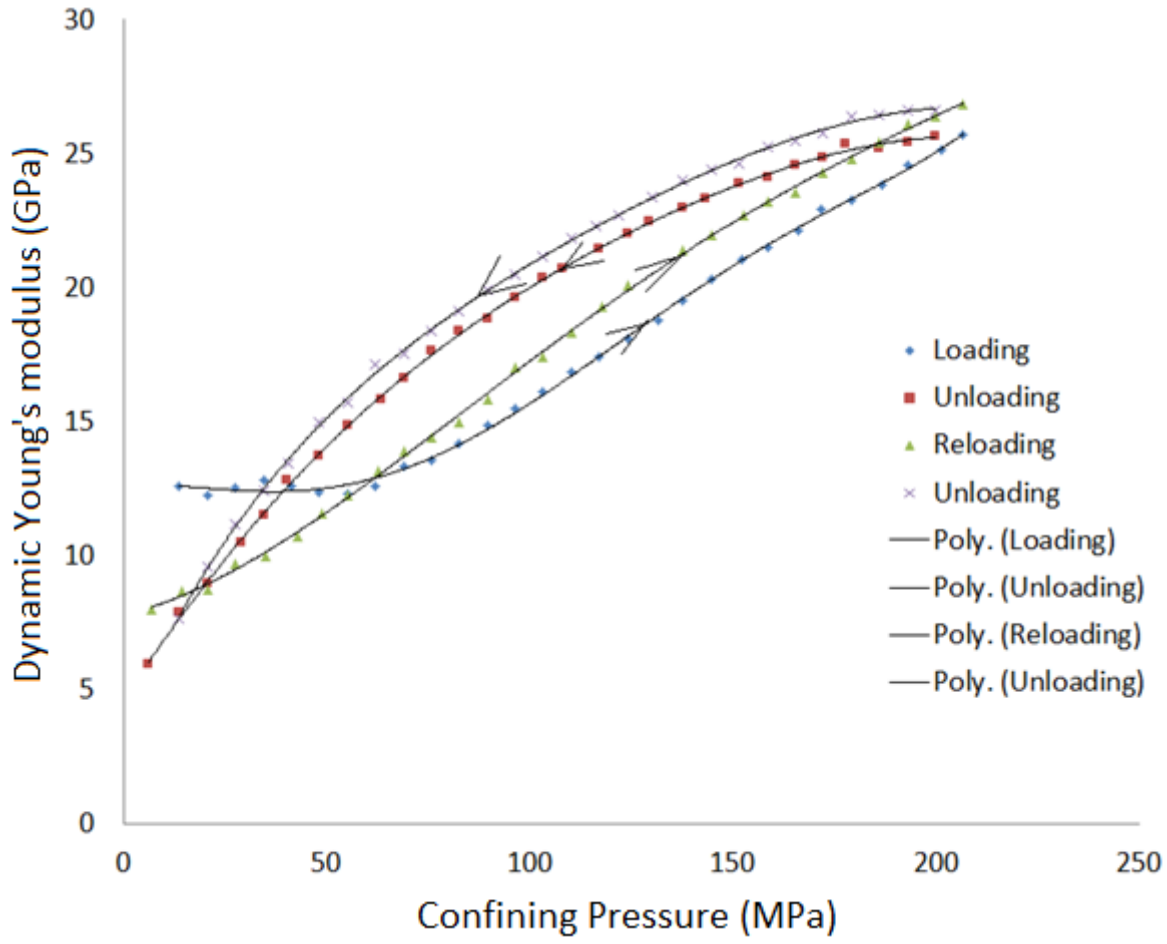

Figure 4.26 Dynamic Young's modulus with respect to the applied cyclic confining pressure on the PGA-WG (J23) graphite samples

In the Figure 4.26 and 4.27, both PGA and Gilsocarbon showed similar trend in their cyclic behaviour compared with their first cycle, only that their second cycle of loading became stiffer compared with the first circle of loading. The non-linear steep DYM increase with pressure was clearly a result of progressive closure of microcracks. The turnaround (sudden change) tends to move slightly to the left hand side during the second cycle which suggested that the reloaded graphite microstructure is different to the virgin microstructure, hence different behaviour during loading leading to different values of the turnaround. The author suggests that repeating the loading cycle more than once would increase the stiffness of the sample until there was no further major change in the sample microstructure. This is at least consistent with compaction of rocks (polycrystalline material) that compact more if pressure cycled [124].

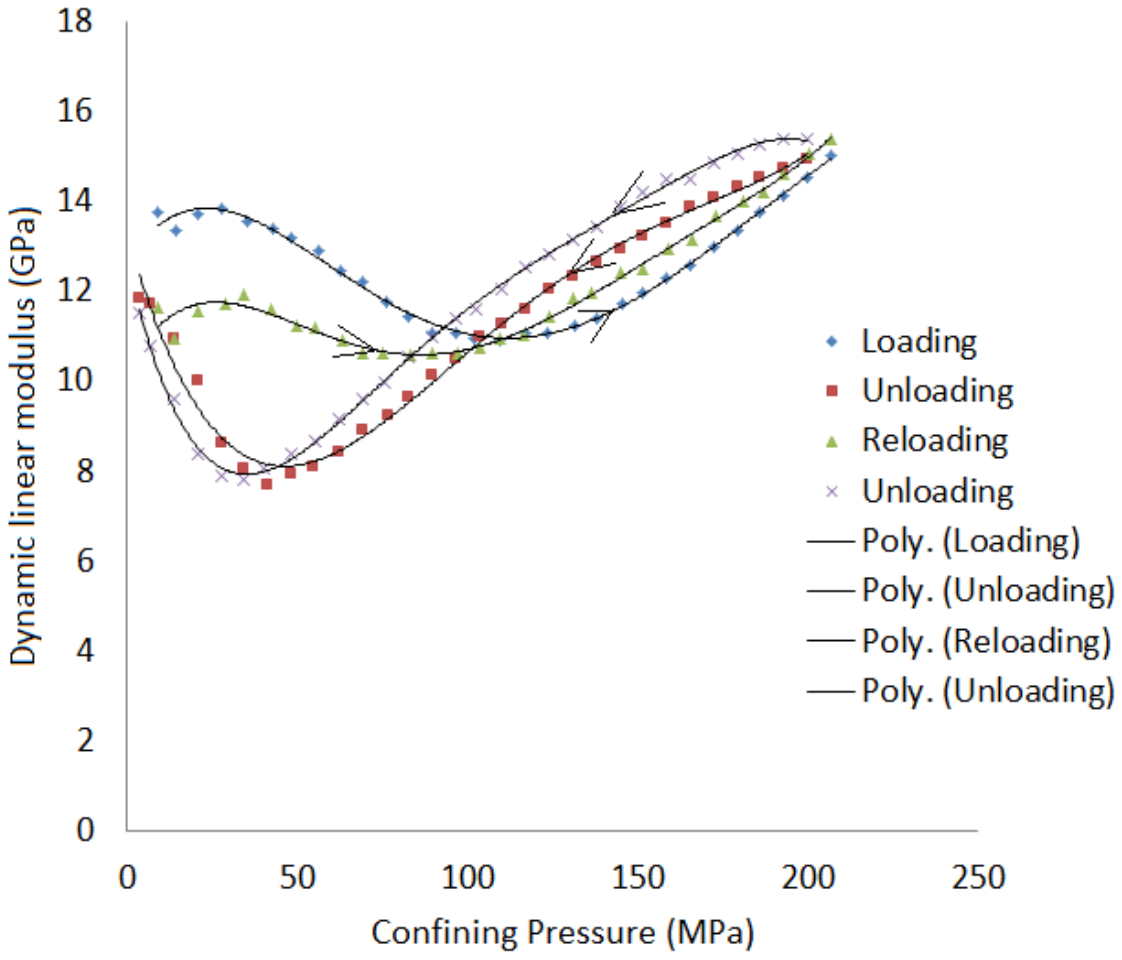

Figure 4.27 Dynamic Young's modulus with respect to the applied cyclic confining pressure on the Gilsocarbon (I10) graphite samples

4.3.2 Hydrostatic S-wave measurement

The behaviour of the graphite S-wave velocity under compression (Figures 4.28 and 4.29) were similar to the graphite P-wave velocity behaviour mentioned above, this was due to opening and closing of the microcracks. The shear modulus value of Gilsocarbon (Figure 4.29) was higher than the value of PGA, this due to higher density of Gilsocarbon. In the PGA-AG sample, the stiff basal plane are preferentially aligned perpendicularly to the measurement direction, therefore the PGA-AG was less stiff compared with Gilsocarbon which was more dense. Gilsocarbon had shorter time of flight, which resulted in a higher shear modulus than PGA-AG.

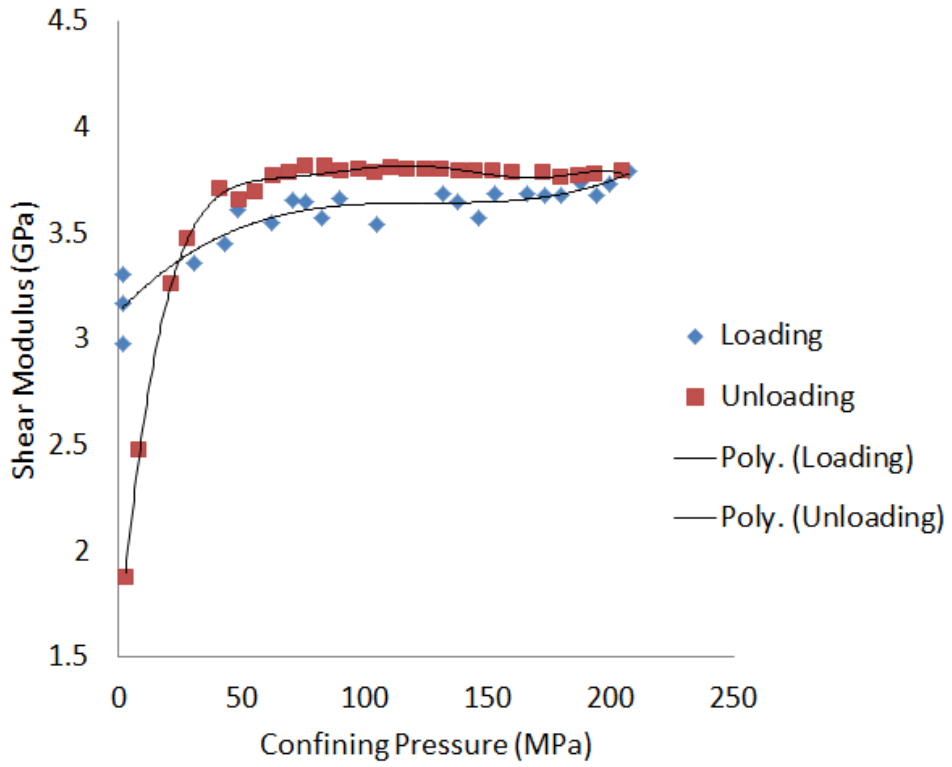

Figure 4.28 Shear modulus with respect to applied confining pressure on the PGA-AG (J15) graphite samples

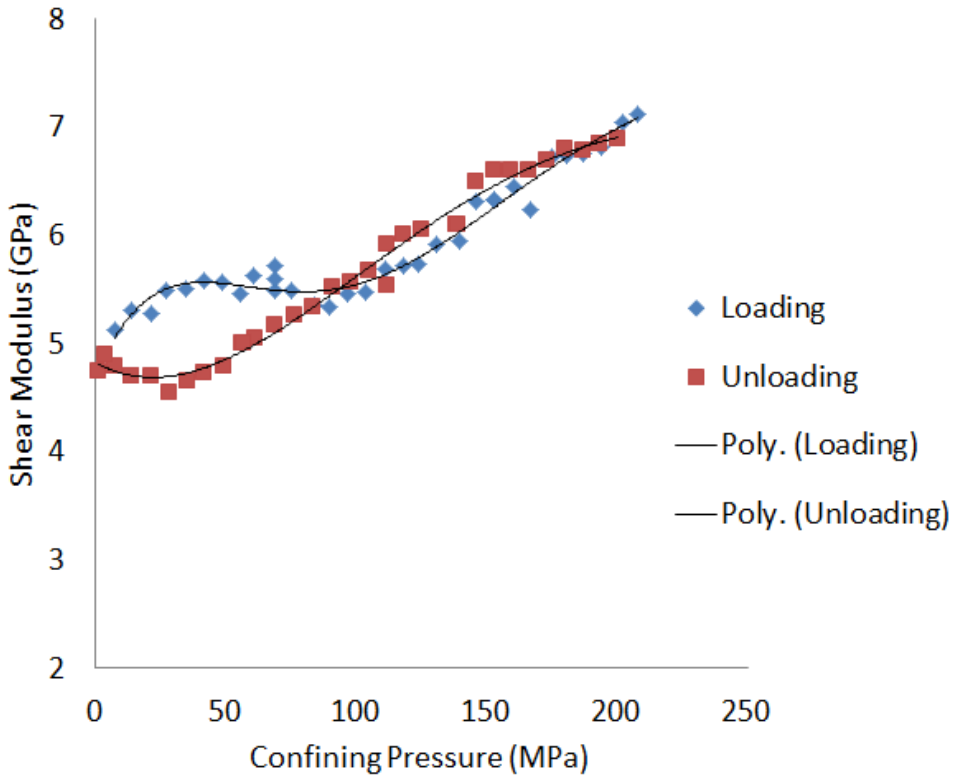

Figure 4.29 Shear modulus against applied confining pressure on the Gilsocarbon graphite sample (I5)

4.3.3 Comparison between static and dynamic modulus of PGA and Gilsocarbon

The magnitude of the strain in variation and dynamic experiment was tiny compared to the strain variation in a static experiment. Also the wave length of the ultrasonic wave was important as the wavelength must be much larger than the grain size otherwise if the wavelength was too small it could pass through the material without interacting with the porosity.

As shown by the hydrostatic loading cycles (Figures 4.15 and 4.16), the static stiffness corresponding to the slope of the loading line was much lower than the dynamic stiffness in the Figures 4.23 and 4.25- 4.27 that was determined from the ultrasonic velocity measurements. Upon loading, there are elastic and inelastic deformation occurring whereas upon unloading, the initial slope corresponded to mostly elastic deformation. Hence the unloading stiffness (as illustrated in the Figure 4.15 and 4.16) are quite similar to the dynamically measured stiffness during loading apart from Gilsocarbon dynamic loading stiffness.

4.3.4 Discussion and conclusion

The static and dynamic elastic moduli of the two grades of graphites (PGA and Gilsocarbon) have been measured for comparison. It was shown that the anisotropy of the elastic properties of PGA is due to the crystallographic texture formed during the extrusion process, the pores and

microcracks are not totally closed at a pressure of 200 MPa and they greatly influence the exact values of the bulk elastic moduli of graphite. At low pressure, the increase in modulus was negligible, due to the fact that there was not enough pressure to cause major grain distortion and porosity. The modulus of the graphite grades increased rapidly in a non-linear manner below and above a critical pressure, critical pressure referred to as the crack-closure pressure, as the pressure increased. During loading, the microcracks are closed at critical pressures of ~50 MPa and ~100 MPa for PGA and Gilsocarbon respectively. The modulus increased sharply after these critical pressures. During unloading, closed cracks reopened gradually until the critical pressure was reached. Below the critical pressure, the graphite almost recovered its original volume at a faster rate. It can be concluded that there was strong stress dependency in the hydrostatic confining conditions due to closure and opening of microcracks.

4.4 Post-deformation microstructural characterization and properties measurement

After deformation, the change in microstructure properties was characterized using the x-ray tomography technique, the helium pycnometer and the mercury porosimeter mentioned in Chapter 3.

4.4.1 Tomography scans and mercury pycnometry results

Gilsocarbon graphite sample (I8) was scanned before and after hydrostatic deformation, the total tomography slices for each sample was 1800 slices. One of the middle slices (slice 957 is shown in the Figure 4.30) was chosen in order to examine the microstructural change. The scan of the virgin sample is shown in the Figure 4.30A and the scan of the deformed sample is displayed in the Figure 4.30B. In the deformed scan, the red circled areas showed some of the regions where there was porosity closure while the green areas showed some of the areas where crack opening was noticed. Both porosity opening and closure were noticed though out the whole graphite microstructure (filler and binder). These microstructural changes were responsible for the behaviour of graphite under high pressure measurement.

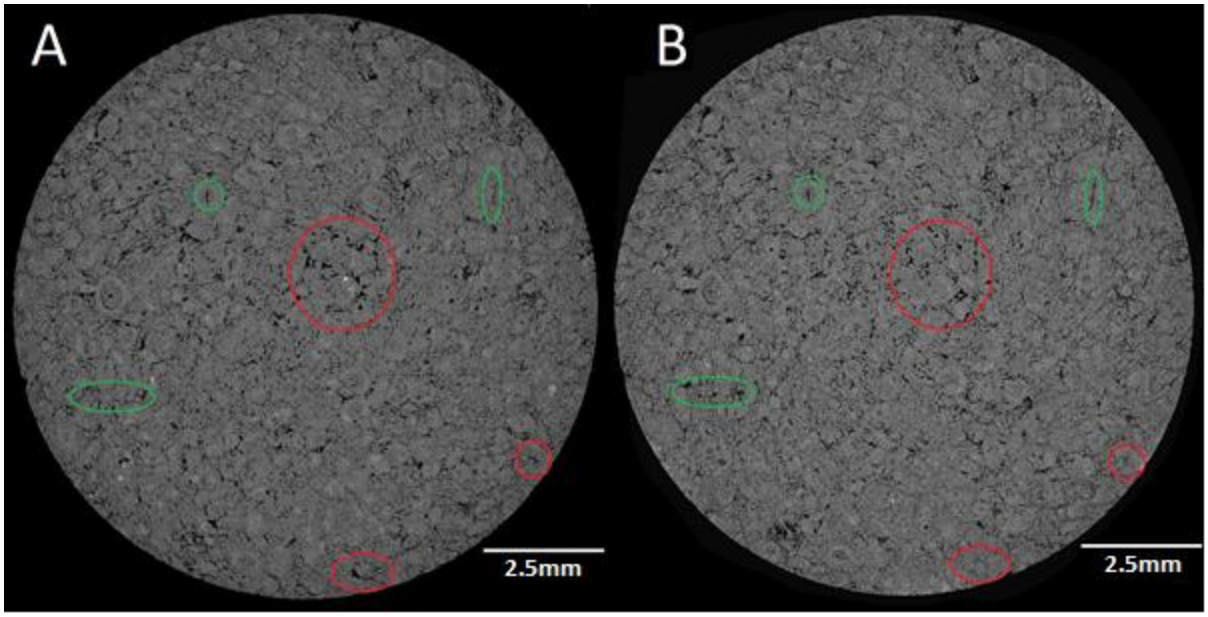

Figure 4.30 Tomographic scans of Gilsocarbon (I8); (A) before and (B) after cyclic confining pressure of up to 200 MPa. The red circled areas showed some of the regions where there was porosity closure while the green areas showed some of the areas where crack opening was noticed after deformation.

In order to investigate the porosity changes before and after deformation, Aviso was used to estimate the equivalent pore diameter of tomography scans of Gilsocarbon sample (I8) before and after deformation. The same region of interest was analysed in both scans. A volume of 300X300X300 voxels was analysed. The result is shown in the Figure 4.31. The smallest feature in the tomography scan was 14.6 μm/pixel. In the Figure 4.31, the equivalent pore diameter below 51.1 μm is reduced after deformation. The results indicate that the amount of macropores have reduced after deformation. The same trend (closure of macropores from pore radius 10 - 100 μm) was noticed in the mercury pycnometry result shown in Figure 4.32. It provided reasonable evidence that confirmed the pore closure seen in the two dimensional image (Figure 4.30). The only limitation to with this approach is that porosity micropores below 14.6 μm cannot be seen in the scans.

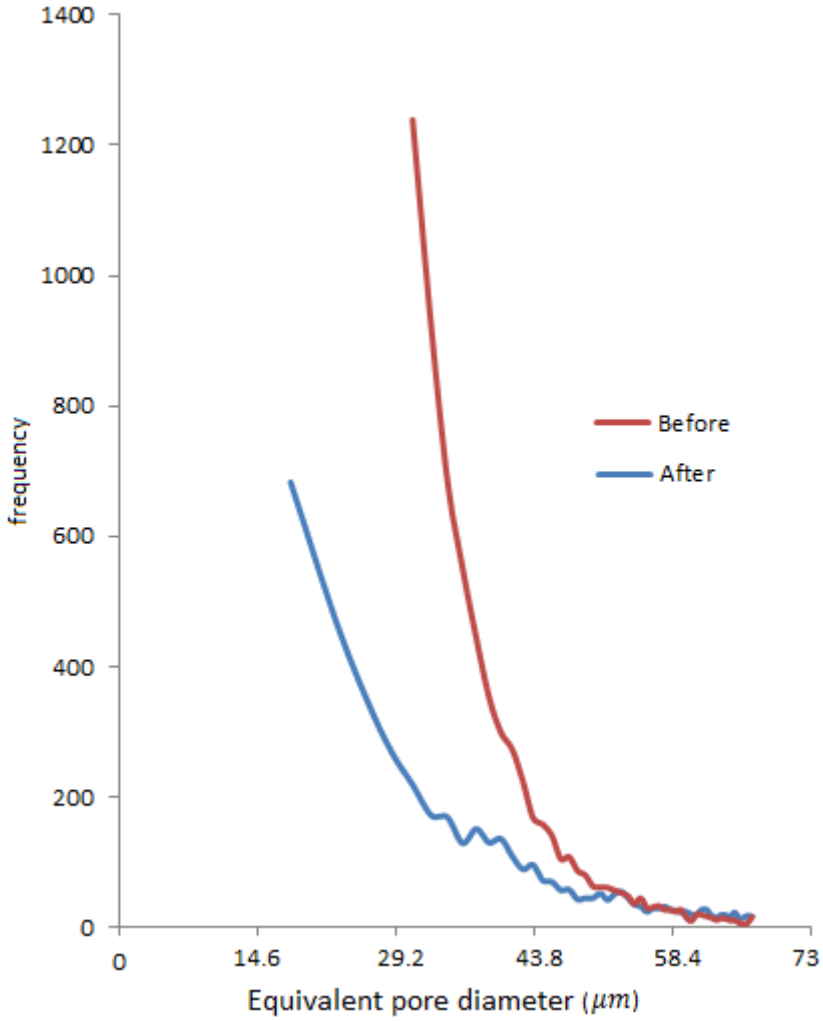

Figure 4.31 Frequency of the equivalent pore diameter of Gilsocarbon sample I8 tomography scans before and after deformation

The change in porosity throughout the whole scanned micrograph was investigated further by using mercury porosimetry to analyse the porosity distribution before and after deformation. These results are shown in Figures 4.32 and 4.33

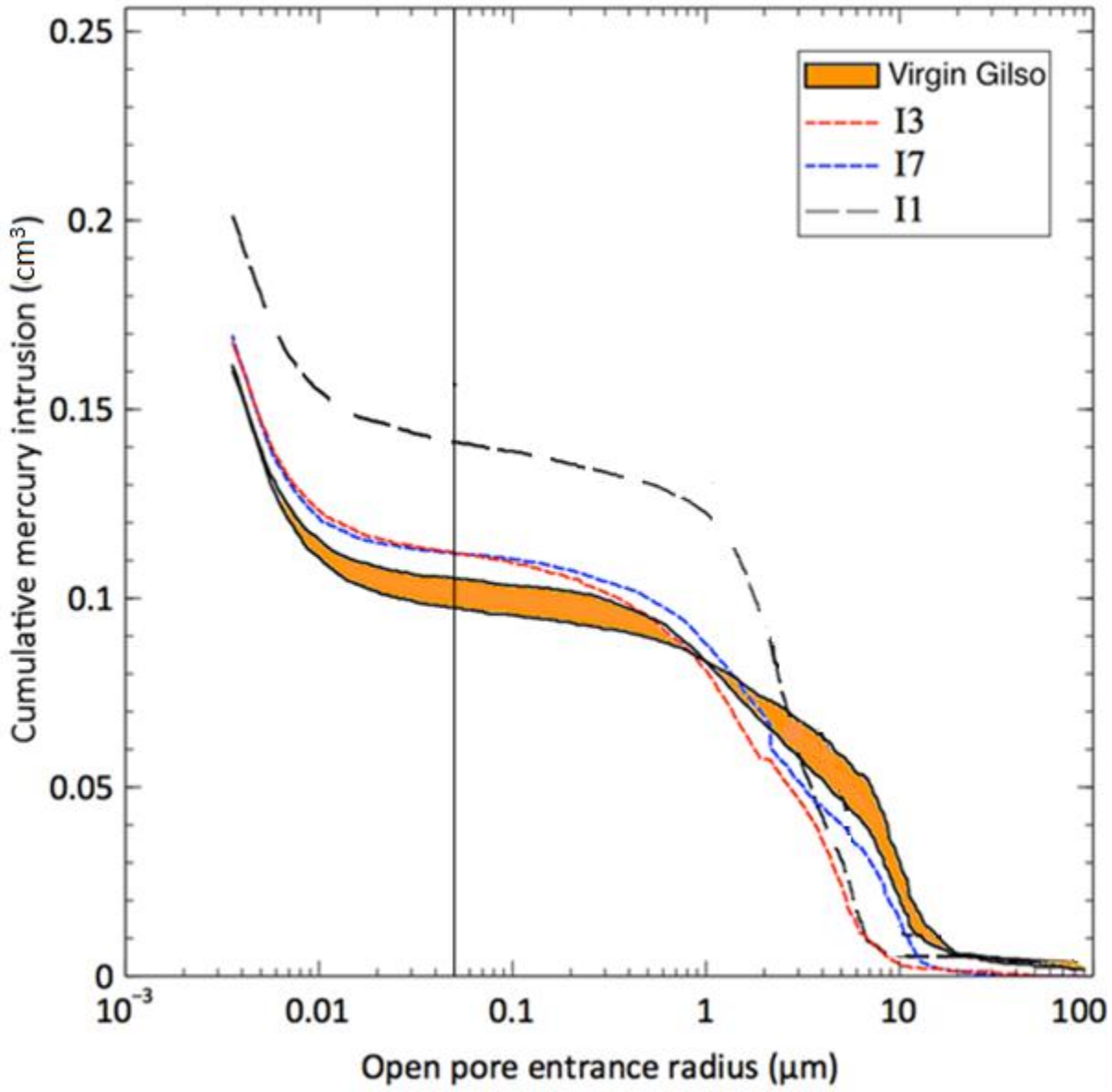

Figure 4.32 Pore size distribution of virgin and deformed Gilsocarbon graphites (I1 – hydrostatically loaded up to 200 MPa, I3 – hydrostatically loaded up to 200 MPa and differential stressed up to 36 kN, and I7- hydrostatically loaded up to 80 MPa)

In the Figure 4.32, the broken lines represent the deformed Gilsocarbon while the solid lines represent the virgin Gilsocarbon. There seems to be a general decrease in the porosity volume of pores radius 1 – 100 μm while increase in the volume of open pore radius <1 μm. The sample I3 was hydrostatically loaded up to 200 MPa and differential stressed up to 36 kN while sample I7 was loaded up to 80 MPa, the sample I3's volume of open pore entrance radius 1 - 100 μm seemed to be smaller than the sample I7's volume of open pore entrance radius 1-100 μm. In both cases, more open pore entrance radius <1 μm are produced compared with the virgin sample. Hydrostatic load up to 200 MPa seemed to have a microcrack formation effect on

Gilsocarbon microstructure compared with other loading mode i.e. axial deformation, which seemed to have closed more microcracks formed by the hydrostatic stress. This behaviour is strange because axial deformation rather than hydrostatic compaction was expected to induce a greater microcrack formation effect on the Gilsocarbon microstructure. It is suggested that in closing the large pores during hydrostatic loading, induced strain heterogeneity caused sites of high internal stress that opened up pores when the pressure was released. The axial deformation might have "healed" these sites of high internal stress causing them not to open as micropores when the stress was released.

4.4.2 Gilsocarbon dynamic Young's modulus and helium pycnometer results

It can be concluded that the higher the hydrostatic stress (200 MPa), the more microcracks that formed between the grains and the more closure of macropores resulted in decrease in DYM, by up to 11 %. In axial deformation, pore size ≥ 1 $\boldsymbol{\mu m}$ closed, therefore reduced the DYM by 11.5 %. These results are illustrated in the Table 4.3.

Table 4.3 Change in Gilsocarbon elastic properties at different loading mode (i.e hydrostatic loading, differential stress and dynamic loading)

Elastic properties	Virgin Gilso (GPa)	Low CP up to 80MPa	High CP up to 200MPa	CP of 200MPa and Axial deformation
E	12.4	-6 %	-11 %	-11.5 %
G	5.1	-2 %	-2 %	-6 %

Axial deformation created more shear effect in the Gilsocarbon microstructure due to sliding of the bassal planes on top of each other in the process of moving the crystal into the neighbour accomodative void. It is suggested that the bonds between the planes become weaker as the frictional forces increase resulting in lowering of the shear modulus.

The DYM and the shear modulus of Gilsocarbon (before and after deformation) for all different loading modes are shown in the Figure 4.33.The DYM value for the deformed samples seemed to be more reduced than the shear modulus as expected. The Gilsocarbon behaviour seemed to be independent of porosity compared with PGA (Figures 4.36 and 4.37), this shows that PGA microstructure is more heterogeneous.

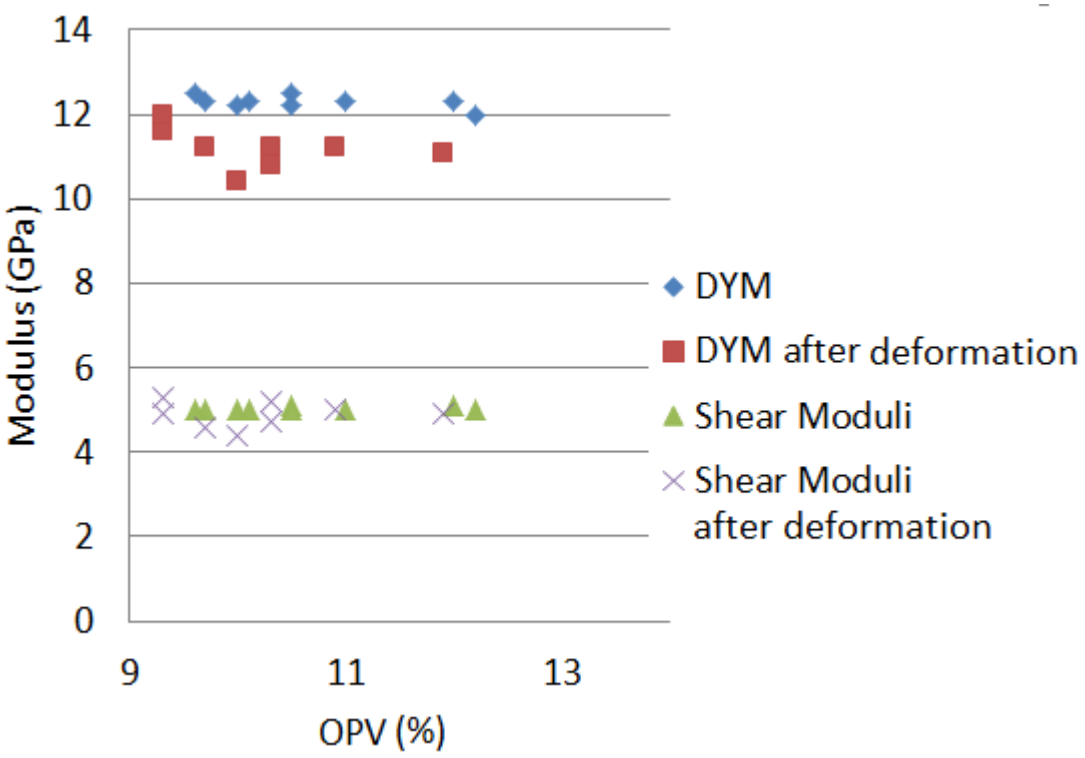

Figure 4.33 DYM and shear modulus of Gilsocarbon against the Open Pore Volume (OPV) before and after deformation at different loading modes (i.e. hydrostatic loading, differential stress and dynamic loading)

In the Figures 4.34 and 4.35, both Virgin and deformed PGA show porosity distribution range from macropores region to the micropores and mesopores regions. The microstructure of both deformed samples shows overall reduction in the volume of open pore radius 0.003 – 12 μm compared with the virgin sample. Unlike the Gilsocarbon, there was general reduction PGA-WG and PGA-AG macropores size < 10 μm. This might be due to higher total porosity in PGA than Gilsocarbon. There seems to be more deformation or collapse in the PGA graphite structure due to more accommodative void in the PGA microstructure compared with Gilsocarbon which is denser.

PGA-WG (J22) pore sizes generally decreased more than PGA-AG (J9) under the same loading condition (confining pressure up to 200 MPa), which suggested that more pores closed in the PGA-WG sample than PGA-AG. This explained the reason why PGA-AG (F5) sample appeared to be stiffer than PGA-WG (F1) sample in the Figure 4.14.

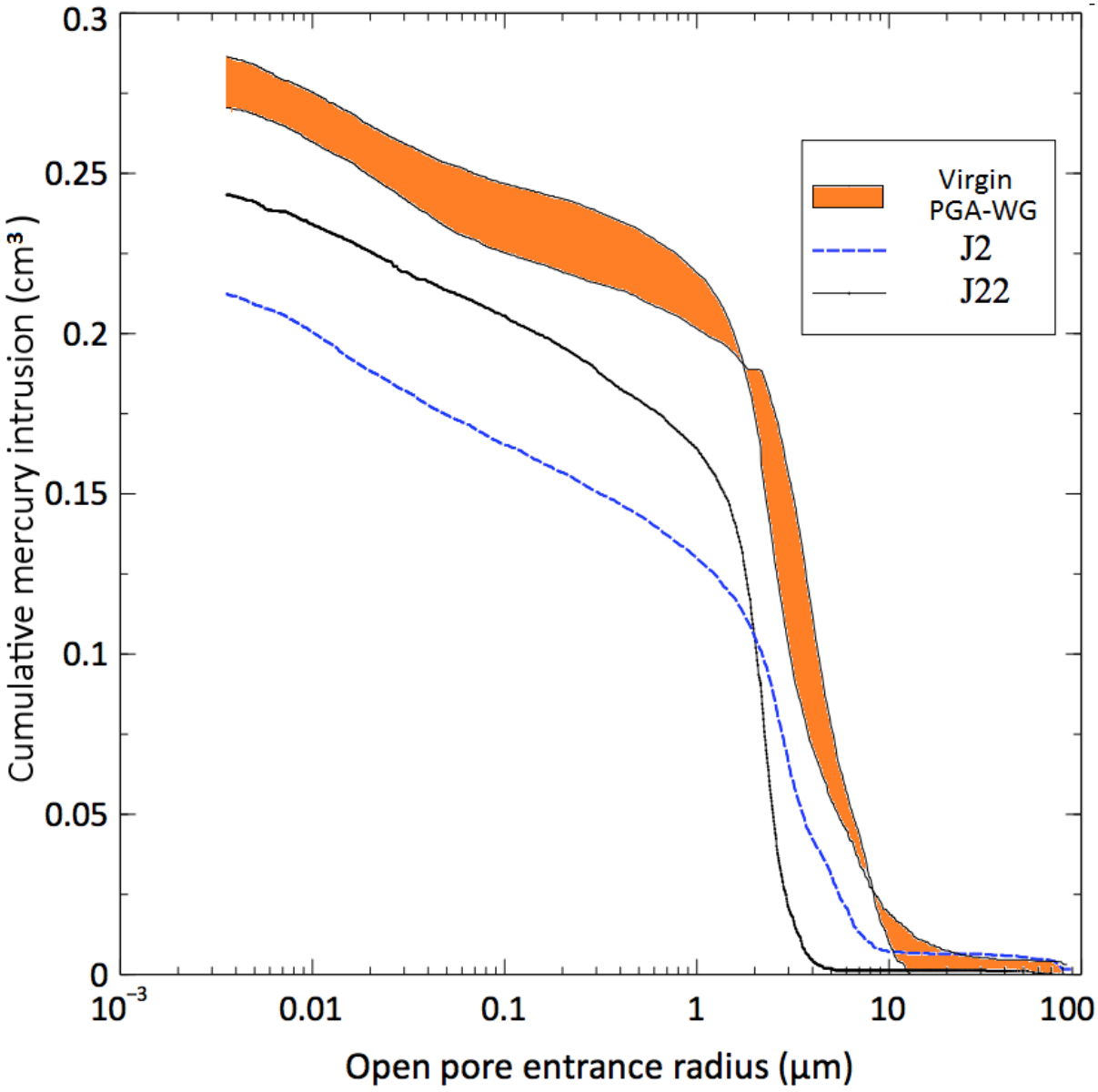

Figure 4.34 Pore size distribution of virgin and deformed PGA-WG graphites (J2 - hydrostatically loaded up to 200 MPa and differential stressed up to 57 MPa, J22 - hydrostatically loaded up to 200 MPa)

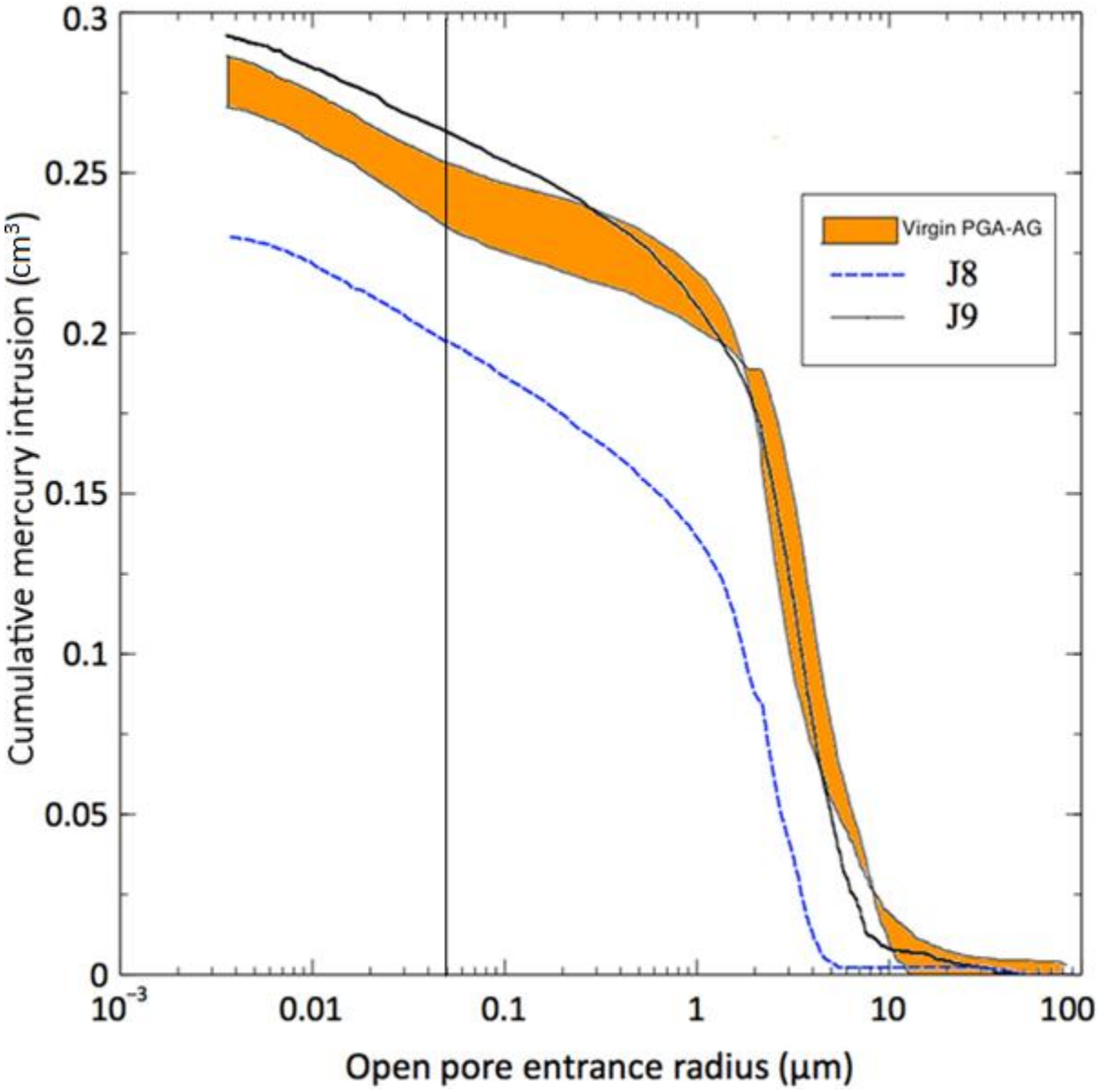

Figure 4.35 Pore size distribution of virgin and deformed PGA graphites (J8 - PGA-WG sample hydrostatically loaded up to 200 MPa and differential stressed up to 74 MPa, J9 - PGA-WG sample hydrostatically loaded up to 200 MPa)

4.4.3 PGA dynamic Young's modulus and helium pycnometer results

In Table 4.4, E and G represent the DYM and shear moduli parallel to the extrusion direction (PGA-WG) respectively while E* and G* represent the DYM and shear moduli perpendicular to the extrusion direction (PGA-AG) respectively. Both DYM and shear modulus of deformed PGA were ~ 4 times and ~27 times more reduced than the DYM and shear modulus of Gilsocarbon. This can be associated with the lower porosity in Gilsocarbon than PGA.

Table 4.4 Change in PGA elastic properties at different loading mode

Elastic properties	Virgin PGA (GPa)	High CP up to 200MPa	CP of 200MPa and Axial deformation
E	11.1	-43.1%	-43.2%
G	4.2	-40.5%	-40.5%
E*	5.9	-44.1	-54.2%
G*	3.3	-54.5%	-54.5%

In the Figures 4.36 and 4.37, the open porosity volume of PGA seemed to decrease after deformation as expected, likewise the DYM values. There was a vague trend of porosity decreasing after deformation of Gilsocarbon samples (Figure 4.33) compared with PGA samples (Figures 4.36 and 4.37). Unlike the Gilsocarbon, PGA showed more DYM reduction after deformation (as expected).

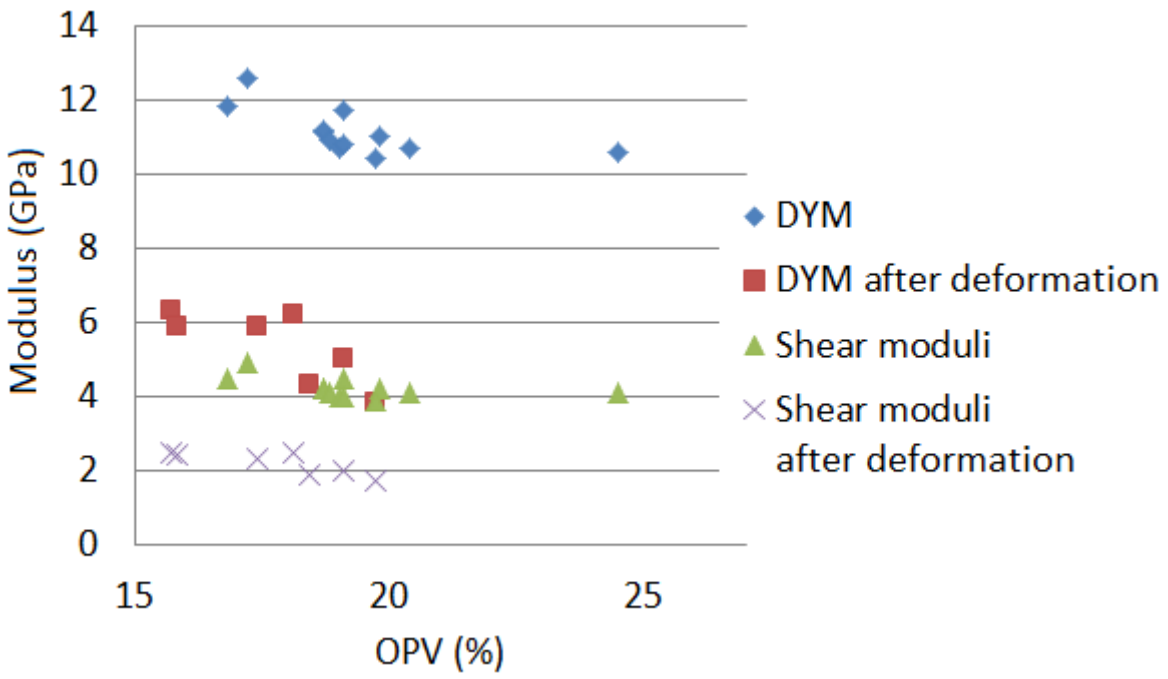

Figure 4.36 DYM and shear modulus of PGA-WG against the Open Pore Volume (OPV) before and after deformation at different loading mode

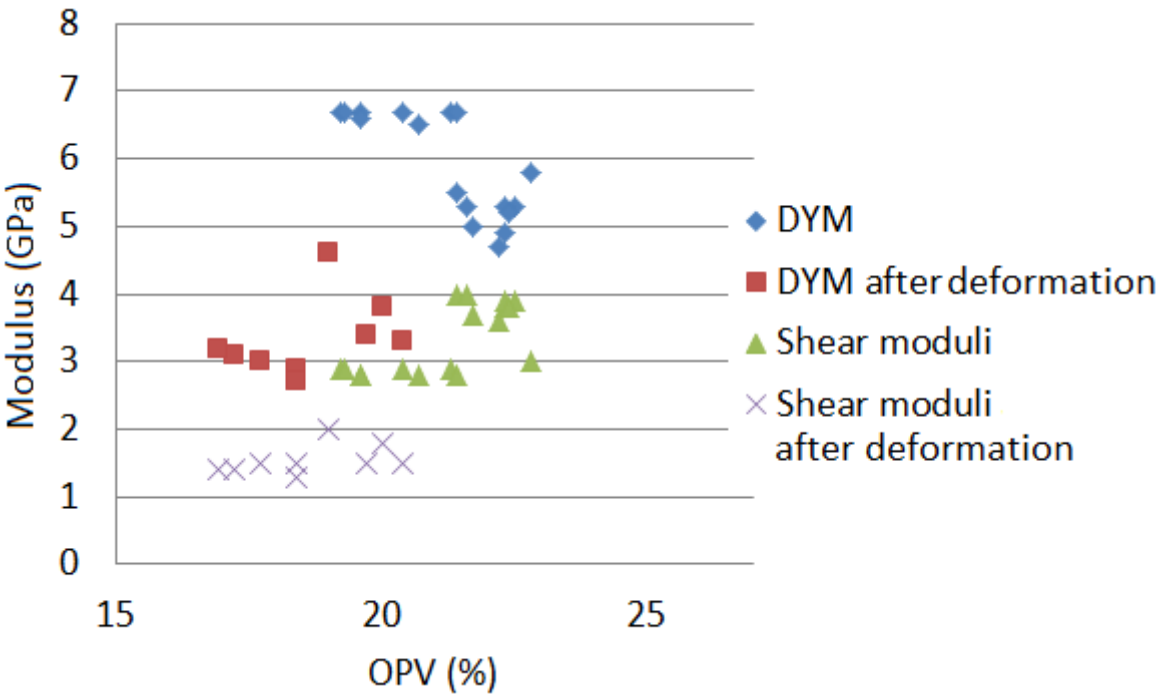

Figure 4.37 DYM and shear modulus of PGA-AG against the Open Pore Volume (OPV) before and after deformation at different loading mode

4.4.4 Pole figures for PGA

The contoured pole figure plot of virgin PGA was compared with the contoured plot of deformed sample. The plot is shown in Figure 4.38, only the 0001 plane was considered because

it was the only crystallographic plane that shows a strong preferred orientation. It was noted that a girdle formed across the pole figures in a virgin sample is distorted after hydrostatic loading up to 200 MPa. The initial strong orientation in the girdle becomes scattered and wider. It is suggested that the grains oriented parallel to the basal plane are distorted during loading due to basal sliding with the aid of surrounding spectrum of pores.

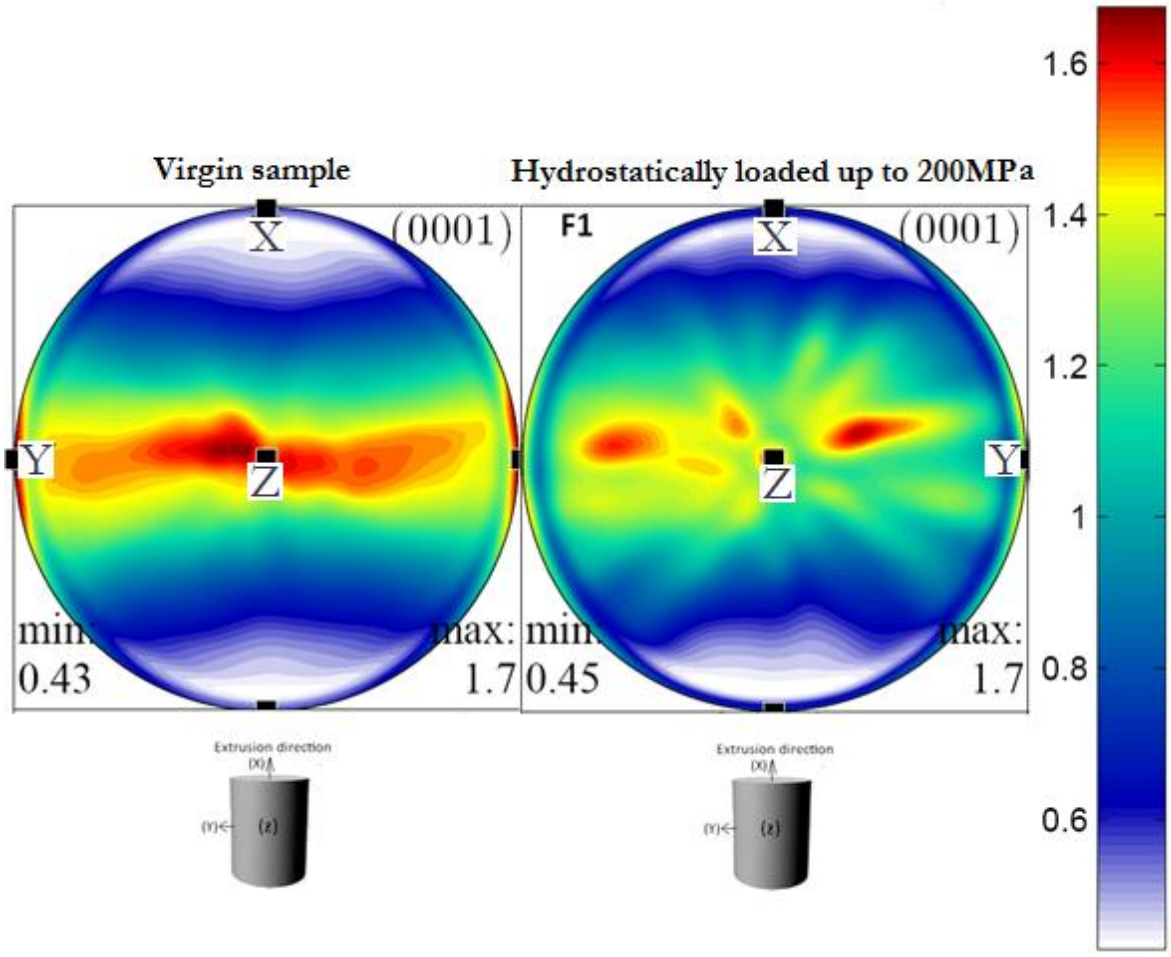

Figure 4.38 Pole to basal planes derived from the ODF calculated from the PGA experimental pole figures before and after deformation. Colour scale is in multiples of uniform distribution.

4.4.5 Discussion

There was a general decrease in both DYM and shear modulus of deformed samples by applying increasing hydrostatic stress. This behaviour was more pronounced in PGA than Gilsocarbon. The modulus value of PGA decreased by ~ 50 % regardless of being subjected to different loading mode (i.e. hydrostatic loading, differential stress and dynamic loading) unlike Gilsocarbon sample which a shows slight decrease by 8 – 10 % for the same modulus. It can be concluded that the decrease in the modulus of graphite by applying hydrostatic stress is mainly

due to crystalline re-orientation and microcrack formation occurring with an increase in stress. However the contribution of an increase in dislocation density as the stress increases cannot be ignored. The main mechanism of decrease in DYM by applying hydrostatic stress can be considered to be dependent on the orientation of the crystallites and of pores in the graphite relative to the direction of applied stress and the level of applied stress.

4.5 Conclusion

Studying the cause and nature of the changes to the porosity may help to provide a mechanistic understanding of corresponding changes in graphite's physical and mechanical properties. This is essential to assess the structural integrity of graphite components. In this work, hydrostatic deformation of unirradiated graphite under high pressure was analysed to understand the effect of porosity on both dynamic and static elasticity. The effect of these porosity changes on graphite bulk properties has been investigated using the helium and mercury porosimetery approach, and effective medium models.

The stress- strain relationship of polycrystalline graphite is known for its non-linearity and hysteresis loops during cyclic loading stressing. During axial loading, within the individual crystallites, the external stress can lead to a combination of (a) elastic deformation, (b) irreversible shear (or plastic) deformation, (c) relief of internal stresses, and (d) local stresses greater than the breaking strength which can cause microcracks. The first two processes cited above have been used to account for the general shape of the axial stress-strain curves.

In most of the experiments in this work, the deformation was closing porosity despite new porosity being generated during unloading. The axial stress-strain curve initially is linear with an elastic behaviour, the pre existing microcracks close during the initial loading of the sample, at this stage there is no circumferential strain within the sample. During unloading, a large hysteresis was formed. The stressed grains are relieved; the initially closed pores began to reopen. It is suggested that during this stage, the volume of pore re-opening superseded the volume of pores closing, the graphite sample volume almost fully recovered.

In axial compression tests, PGA-AG samples was less stiff than PGA-WG samples. In hydrostatic compaction tests, the PGA-WG sample deformed more because it has to undergo a less complicated shape change. This was because the symmetry of their anisotropy is parallel to the symmetry of its sample

For porous material (graphite samples), measurements have shown that it was possible to measure Young's modulus using longitudinal and shear velocities. The estimated values for

Young's modulus agree with the values estimated in previous work [115, 116]. Considering a density value of 1.765 g/cm^3, Young's modulus of virgin graphite in different directions in graphite samples varies from 5 to 12 GPa. At higher pressure, the densities of graphite samples were higher than 1.765 g/cm^3 (2.1 g/cm^3).

The average Young's modulus of virgin PGA-AG, PGA-WG, and Gilsocarbon were 5.9 GPa, 11.1 GPa and 12.4 GPa respectively, while previous work has reported Young moduli for PGA PGA-AG, PGA-WG and Gilsocarbon to be 5.4 GPa, 11.7 GPa and 10.85 GPa respectively without uncertainty estimates[18]. The modulus parallel to the extrusion direction was greater than perpendicular to the extrusion direction as shown in the Figure 4.3D. Preferential orientation of the porosity also contributes to the increase in modulus.

The increase in DYM of the samples with increasing pressure demonstrates the significant contribution of the internal pores and microcracks to the bulk elastic properties of the graphite and their anisotropy. The value of the shear modulus is less than the value of the dynamic Young's modulus for all materials as expected.

The mercury porosimetry results revealed that plastic deformability of the graphites by hydrostatic loading can be identified with changes in the pore size resulting from the closing and shrinking of the pores. It shows that there was more porosity closure in deformed PGA than deformed Gilsocarbon under the same loading mode, the volume of Gilsocarbon seems to increase or remain the same due to similar volume of microcracks closing and opening during deformation. There is a general porosity reduction in deformed PGA. It was quite a difficult task to study the changes in cracks less than 1 μm before and after deformation due to structural damage to the graphite after critical pressure exerted by mercury.

The distortion in graphite crystals after loading can be noted in the XRD pole figure contour plots. Wide range of porosity in the graphite microstructure and crystallograhic preferred orientation were suggested to be one of the reasons for an easy migration of crystallites during loading. There was very little permanent strain in Figure 4.38, therefore more significant change was not expected.

CHAPTER 5

5 Micromechanics modelling

Pore spaces are responsible for most of the differences in the mechanical and physical properties of graphite [5]. Many attempts have been made in the past to explain the elastic behaviour of porous materials [74, 76, 77, 119]. Since graphite contains a broad distribution of pore sizes (from sub-micron to few microns) with irregular shapes, it is more challenging to describe the elastic behaviour of its complex microstructure. However attempts have been made in this thesis to understand the effect of porosity change (closure and opening) on apparent bulk modulus (the slope of pressure-volumetric strain curves calculated as shown in chapter 4).

5.1.1 Elastic of Pore-free aggregate

As a starting point of reference, expected average elastic moduli can be calculated according to various averaging schemes for an isotropically-textured, pore free graphite aggregate. To do this, the graphite single crystal constants were obtained from Bosak [21], the elastic bulk moduli and shear moduli [Voigt Reuss Hill ($K_{VRH,}$ and G_{VRH}), Self-Consistent ($K_{SC,}$ and G_{SC}), Hashin Shtrikman positive and negative bound ($K_{HS+,}$ and G_{HS+} , K_{HS-} and G_{HS-})] was calculated using equations from Berryman [125, 126] as shown in the Table 5.1.

Table 5.1 Estimated elastic stiffness constants for pore-free, isotropically-textured polycrystalline aggregates of the hexagonal crystals of Graphites A, B [125] and Graphite C (Single crystal constants used in calculations are found in Bosak [21], estimated using equations from Toonder et al. [126] and Berryman [125]). All units are GPa

Moduli	Graphite A	Graphite B	Graphite C
K_R	35.8	35.8	36
K_V	286.3	286.3	281
K_{VRH}	161	161	150
K_{HS-}	36.2	42	
K_{HS+}	204.2	204.2	
K_{SC}	77.8	88	
G_R	0.65	9.2	11
G_V	217.9	219.4	240
G_{VRH}	109.3	114.3	118
G_{HS-}	1.21	14.8	
G_{HS+}	146.2	148.9	
G_{SC}	38.9	52.6	

The differences in moduli of Graphite A, B and C shown in Table 5.1 calculated according to a given averaging scheme are due to the different values of single crystal elastic constants reported. There is a huge difference between Voigt (286.3 GPa) and Reuss (36 GPa) averages for *K*, presumably on account of the anisotropy of the single crystals. The Reuss averages are much, closer to the experimental values extrapolated to zero porosity. Reuss averaging assumes constant stress in all grains, i.e. like a stack of plates normal to the applied load, whereas Voigt is constant strain between grains. Reuss averages exactly describes the effective moduli of a suspension of solid grains in a fluid, and also describes the moduli of shattered materials in which solid fragments are completely surrounded by the pore fluid [74]. It may be suggested that the freedoms given by the presence of porosity might make it easier for strain mismatches between grains to be accommodated. Therefore it may be suggested that the microstructure better supports a Reuss averaging scheme.

5.1.2 Modelling the influence of porosity

The effect of porosity on bulk modulus was considered by using models such as Voigt Reuss Hill (VRH), Hashin Shtrikman positive and negative bound (HS+ and HS-) and Koster and Toksoz (KT) for 2-phase aggregates, considering porosity as the second phase. The Reuss effective bulk modulus (36 GPa) was used as an effective modulus of graphite at zero porosity. Pores are then added to the models and the value of effective bulk moduli was extrapolated to zero porosity. The effect of porosity shapes i.e. needle, sphere, penny and disk shapes were also analysed. It is worth mentioning again that all these models considered assumed that the solid to be isotropic and linearly-elastic. Gilsocarbon experimental data was used to compare the effective medium models because graphite in it is near isotropic. PGA graphite was likewise compared with KT model (even thou PGA is more anisotropic).

5.1.3 Voigt Reuss Hill (VRH) and Hashin-Shtrikman (HS) bounds

In VRH and HS, the bulk modulus of pore-free material (graphite) was taken to be 36 GPa and the bulk modulus of void (air) to be 1.01×10^5 Pa. These were used to calculate the properties of the porous material over a range of porosities from 0 to 25 %. The results were compared with the Gilsocarbon experimental data (I3) where the porosity was closed by increasing the confining pressure. It can be seen in Figure 5.1 that experimentally-observed graphite behaviour corresponds well with the Reuss and HS- bounds. Although Gilsocarbon sample (I3) was hydrostatically loaded up to 200 MPa and then differential stressed up to 36 kN, only the data obtained from the hydrostatic compression up to 202 MPa (loading data without unloading) was

used in Figure 5.1. These models confirmed that the bulk modulus increased as the porosity decreased, as expected for porous materials. However this was not entirely true in the case of graphite, it has also been reported earlier in this work that during loading, microcracks also formed between the grains (i.e. in the Figure 4.26 in the result chapter)

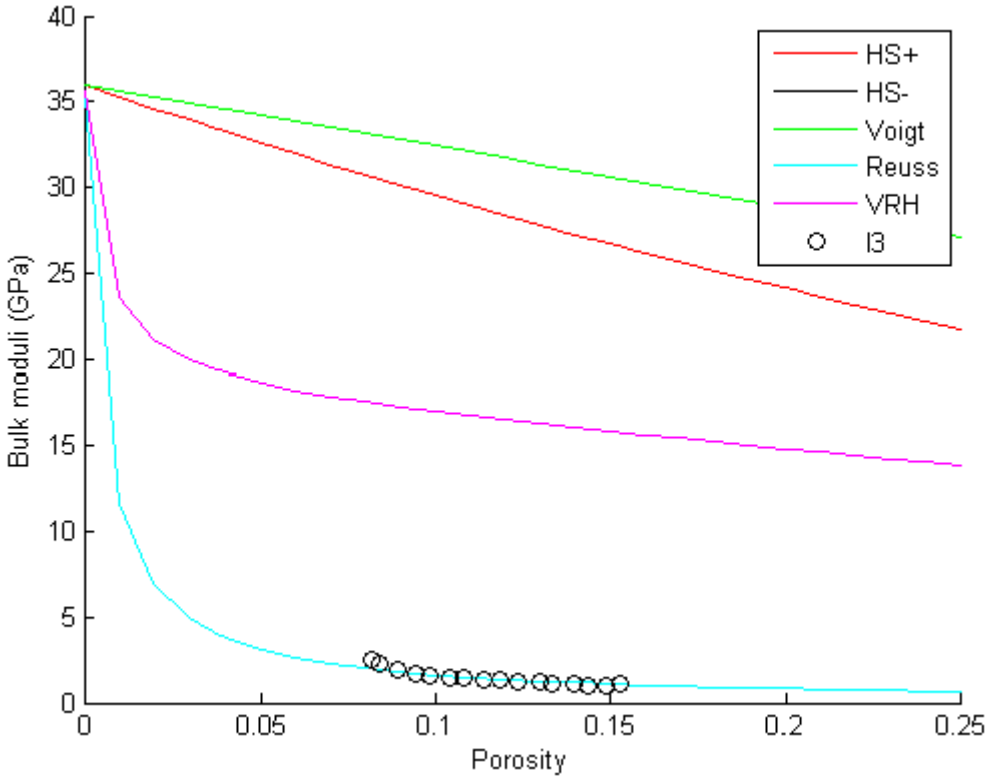

Figure 5.1 Bulk modulus against porosity for the Voigt, Reuss, HS- and HS+ averaging schemes compared with the experimental data for the Gilsocarbon sample (I3)–hydrostatically loaded up to 202 MPa (loading data only). The I3 experimental data conform closely to the predictions of Reuss and HS- averaging scheme.

5.2 Kuster and Toksoz model

The Kuster and Toksoz (K-T) formulation for effective moduli was used to calculate the effect of porosity on effective bulk modulus as shown in the Figures 5.2 and 5.3. The bulk modulus curve increases rapidly below 14 % and 25 % porosity closure in Figures 5.2 and 5.3 respectively. There was not enough pressure to close all the pores in the graphite sample, but it shows continuous increase in bulk modulus at lower porosity. Bulk modulus of non-porous Gilsocarbon can be calculated from the work of Berre [14, 120] to be 8.3 GPa, and this has

It was found that porosity in the form of penny-shaped cracks of aspect ratio 0.003, coupled with a zero-porosity bulk modulus of 8.3 GPa gave the best fit with the experimental data for

Gilsocarbon sample I3 for the porosity range 15 – 8 % (Figure 5.2). The value for zero porosity bulk modulus that has to be assumed is lower than any predicted from single-crystal elastic averaging schemes (Table 5.1), and this is a weakness of this approach.

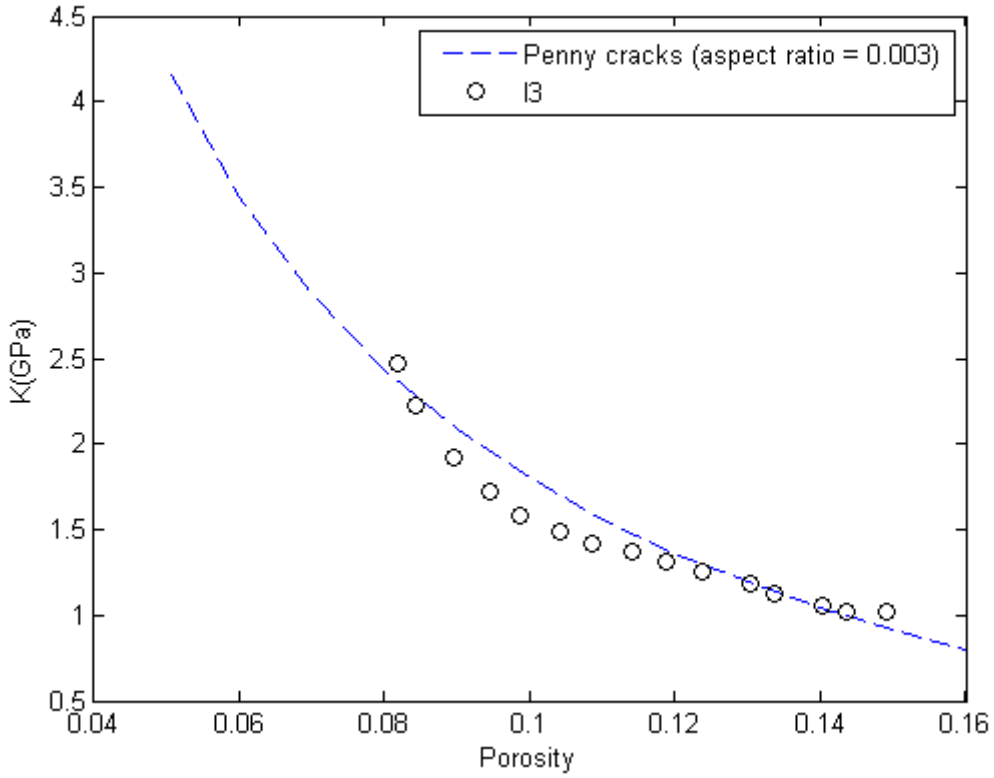

Figure 5.2 Bulk modulus against porosity of the KT model for the crack aspect ratio shown and a zero-porosity modulus of 8.3 GPa, compared with the experimental data for the Gilsocarbon sample (I3)– hydrostatically loaded up to 202 MPa (loading data only)

In Figure 5.3, the KT model slope of 50 % of penny cracks with aspect ratio 0.01 and 50 % sphere porosity was used to fit the PGA sample (J9) experiment data (seismic loading up to 207 MPa). The KT model slope is less steeper than the PGA data. The difference between the model and PGA sample (J9) can also be associated with the porosity interaction in the graphite. Based on the KT model shown in Figures 5.2 and 5.3, it may be suggested that there are more penny cracks with lower aspect ratio (0.003) in Gilsocarbon than PGA sample. The 50 % spherical porosity in Figure 5.3 suggested the presence of large pore size in PGA than Gilsocarbon.

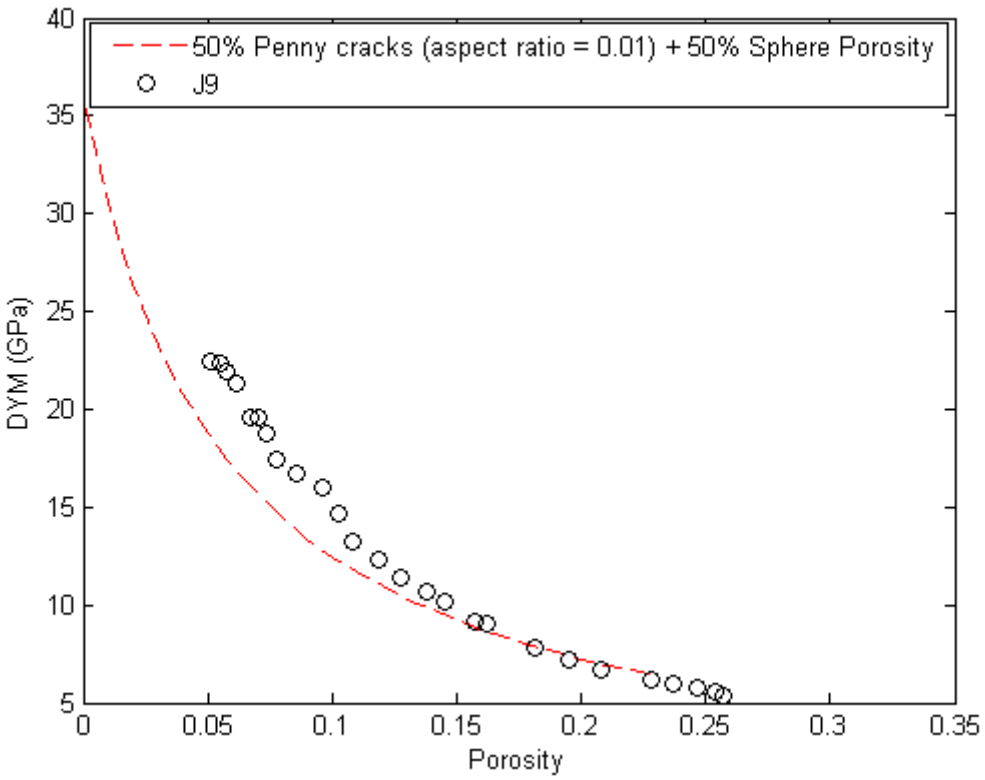

Figure 5.3 DYM against porosity of the KT model for the crack aspect ratio shown and sphere porosity compared with the experimental data for the DYM of PGA sample (J9) – seismic loaded up to 202 MPa (loading data only)

5.3 Conclusion

Models to estimate the mechanical properties of graphites over a wider range of porosity than was accessible from the experimental studies were attempted using effective medium (EM) models. Voigt, Reuss, Hill, Hashin-Shtrikman bounds and Kuster and Toksoz models have been used. None of the models can completely describe all the characteristics of the experimental data; this might be due to porosity interaction in the graphite during deformation. Since the model theories did not explicitly consider the interaction of pores within their medium, they are not completely reliable representatives of the complex change in graphite macrostructure. However, the Reuss averaging scheme for porous graphite, using a Reuss average bulk modulus from single crystal elastic moduli determinations, or the KT scheme for an assumed value of zero-porosity bulk modulus and an assumed crack porosity aspect ratio, provide good fits to the experimental data for Gilsocarbon, and therefore can be used as a satisfactory semi-empirical

basis for calculating effective moduli for porosities outside the experimental range of 8 to 15% porosity.

CHAPTER 6

6 Summary, conclusions and further work

The **aim** of this work was to use hydrostatic pressure to study possible synergies with the elastic behaviour of irradiated graphite Although the nuclear reactor environmental condition is harsh (e.g. high temperature), the effect of temperature on graphite was not investigated in this work. Thus the investigation of possible time-dependent behaviour which might rise as a result of thermally activated deformation processes could not be investigated. Time dependent behaviour could not be seen at room temperature. Hence this is a key area for future research.

Despite carrying out this study only at room temperature, we can recognize that since irradiation changes are primarily related to crystallite reorientation and opening and closure of porosity, these changes can be successfully simulated by hydrostatic compaction of graphite. In this study, modulus increases due to application of pressure have been shown to be related to measured microstructural changes. In the same way, modulus changes induced in graphite through irradiation can be linked to microstructural changes. We can therefore postulate that whether given microstructural changes are induced either by hydrostatic pressure or by irradiation, similar elastic property changes can be expected..

The elastic properties of graphite can change in a nuclear reactor because cumulative damage can lead to graphite shrinkage, potentially resulting in disengagement of individual components and loss of core geometry. Differential shrinkage in the graphite component can lead to the generation of internal stresses and component failure by cracking.

In the course of this study a range of experimental measurements of the effects of hydrostatic and non-hydrostatic loading on isotropic and anisotropic graphites was brought to bear, in order to link the effects to microstructural changes, and this represents the principal scientific contribution of the present research. These studies were:

- The porosity and pore-size distributions and the crystallite orientation in the graphite microstructure were characterized before and after deformation. It was confirmed that Gilsocarbon is near isotropic, as shown by the pole figure uniform intensity. The PGA pole figure showed a strong girdle of poles to basal planes, which confirmed its anisotropic nature. Deformed graphite showed increased scatter of orientations but the initial girdle texture remained.

- Through carrying out hydrostatic compaction experiments coupled with dynamic modulus measurement on nuclear graphite samples. The author was able to demonstrate quantitatively that the increase in Young's modulus is due to porosity closure.

- Application of effective medium models showed the importance of porosity evolution in the graphite during deformation. Graphite is extremely anisotropic, to the extent that the Voigt (isostress) and Reuss (isostrain) averages are so different that they are likely not to be meaningful in an anisotropic material. The question therefore arises "what kind of averaging scheme can be usefully applied?" so that elastic property changes can be linked to microstructural changes extrapolated outside the range of experimental measurements.

A range of elastic property averaging schemes was applied. The heart of this is zero porosity elastic behaviour, because that pins the curves shown in Figures 5.1 and 5.2. The Reuss averages (e.g. 36 GPa for the bulk modulus) were found to be much closer to the experimental values extrapolated qualitatively to zero porosity. Incorporating the effects of porosity using either the Reuss or Kuster/Toksoz averging schemes was shown to provide a useful semi-empirical basis for extrapolating the effects of porosity outside the range of experimental data.

Studying the cause and nature of the changes to the porosity has helped to provide a mechanistic understanding of corresponding changes in physical and mechanical properties of graphite. Thus observations of the microstructural changes caused to irradiated graphite components can be translated into corresponding effects on elastic properties using the approach developed in this thesis.

6.1 Potential future research directions are outlined below

- When graphite is irradiated, its Young's modulus first rises rapidly, then increases more slowly before falling off towards zero with increasing fast neutron fluence (time irradiated). This behaviour is thought to be associated with dislocation pinning, crack closure and finally grain boundary cracking, but no real evidence of this behaviour presently exists is in the literature. The author recommends that future work should involve the investigation of the change in porosity, in graphite irradiated to various levels of irradiation dose, by measuring pore volume change as a function of confining pressure between room temperature to 700°C, in order to study more directly the effects of irradiation and temperature on porosity change. This could be coupled with dynamic modulus measurement.

- In carrying out the mercury porosimeter measurements, it proved difficult to study the closure of cracks less than $1\mu m$ before and after deformation due to the graphite structural damage after critical pressure is reached during mercury porosimetry. Furthermore the use of the helium porosimeter in this work could only measure the total accessible pore volume. The pore size distribution could not be measured. It would be better to characterise the pore distribution using a Quantachrome gas porosimeter which is capable of measuring pore distribution in pores less than $1\mu m$ using a gas medium.

- XRD has low penetration power and small beam size compared with neutron diffraction techniques, and pore statistics can be achieved in coarse-grain materials. A complete pole figure cannot be measured by laboratory X-ray diffraction due to the strong defocusing effect and diffraction geometry as mentioned earlier in Chapter 3. Electron diffraction maybe a better candidate method; [but you can only do this in very thin specimens, do you really want to suggest this, except only for EBSD texture measurements?] the result from electron diffraction can be presented directly in orientation space without the additional mathematical calculations which are necessary in X-ray and neutron measurements. Possible errors occurring during mathematical treatments can be avoided using electron diffraction. However the author did not use a Scanning Electron Microscope (SEM) equipped with an Electron Backscatter Diffraction (EBSD) detector, because it was very difficult to polish the samples. Ion beam milling might be an option to polish the surface, although it takes a long time to do so given the area that would be required to include enough grains. Another option is chemical polishing but graphite is so unreactive it might be difficult to form a good polished surface.

- In-situ measurements (e.g. using high-energy synchrotron radiation) are capable of revealing microstructure and texture evolution in the sample being tested. This would avoid the uncertainty originating from the usage of many different samples. The mechanical properties and texture evolution are strongly dependent on the initial texture and microstructure. By interpreting the measured texture results together with the results of a numerical simulation of texture development, the anisotropic behaviour and the activity of the potential deformation modes in a graphite microstructure could be analysed as a function of initial texture and degree of deformation.

- Multi-scale modelling using finite element analysis would also be attempted. This might be used to model more directly the mechanistic behaviour of graphite non-linearity, by using tomography scans to create a realistic finite element model and using Simpleware

CAD software. It should be aimed to create models with realistic, but simplified, ideal pores which may interact. The apparent bulk modulus calculated in such away can be compared with experimental results.

- Studies of evolution of mechanical properties should be carried out at high temperatures, more closely to simulate the in-reactor condition, due to investigate thermally-activated deformation processes.

7 Appendix

Table 7.1 Summary of data reported in the text for Gilsocarbon graphites (K is the bulk modulus, whilst K after is the bulk moduli after deformation E is the dynamic moduli, whilst E after is the dynamic moduli after deformation, G is the shear moduli whilst G after is the shear moduli after deformation).

ID	Porosity	CPV	OPV	OPV after	porosity after	E (GPa)	G (Gpa)	E after (GPa)	G after (GPa)	V1	V2	K= E/3(1-2V)	K after (GPa)
I7	16.8	7.1	9.7	9.3	16.4	12.3	5	11.6	4.9	0.23	0.18	7.59	6.11
E1	19.6	9.1	10.5	10.3	19.4	12.5	5.1	11.21	5.18	0.23	0.08	7.59	4.47
E2	19.6	9.5	10.1		9.5	12.3	5			0.23		7.59	
I1	20.7	8.5	12.2	11.9	20.4	12	5	11.1	4.9	0.20	0.13	6.67	5.04
I4				9.7		12.4	5	11.2	4.6	0.24	0.22	7.95	6.61
I5				7		12.3	5	11.1	4.6	0.23	0.21	7.59	6.30
I6	16.9	7.3	9.6	9.3	16.6	12.5	5	12	5.3	0.25	0.13	8.33	5.44
I8	17.6	7.6	10	10	17.6	12.2	5	10.4	4.4	0.22	0.18	7.26	5.45
I10	19.1	7.1	12	9.7	16.8	12.3	5.1			0.21		6.97	
I2	19.6	8.6	11	10.9	19.5	12.3	5	11.2	5	0.23	0.12	7.59	4.91
I3	19.2	8.7	10.5	10.3	19	12.2	5	10.8	4.7	0.22	0.15	7.26	5.13

8 References

1. Greenstreet, W.L., et al., *The mechanical behavior of artificial graphites as portrayed by uniaxial tests.* Carbon, 1970. **8**(5): p. 649-663.
2. Jones A N, M.B.J., Marrow T J, *Microstructural Characterisation of Nuclear Grade Graphite using High Resolution Techniques*, in *7th International Nuclear Graphite Specialists Meeting (INGSM-8)*. 2007, Materials Performance Centre: Bakubung, South Africa.
3. Teresa Telesco, K.B., *Critical Technology Assessment: fine grain, high density graphite*, U.S.D.o. Commerce, Editor. 2010: Washington D.C.
4. Fazluddin, S., *Crack growth resistance in nuclear graphite*, in *Department of Materials*. 2002, University of Leeds: Leeds.
5. Kelly, B.T., *Physics of graphite* 1981, London: Applied Science Publishers.
6. Kelly, B.T., D. Jones, and A. James, *Irradiation damage to pile grade graphite at 450° C.* Journal of Nuclear Materials, 1962. **7**(3): p. 279-291.
7. Oku, T. and M. Eto, *Relation between static and dynamic Young's modulus of nuclear graphites and carbon.* Nuclear Engineering and Design, 1993. **143**(2–3): p. 239-243.
8. B. T. Kelly, W.H.M., A. M. Price, J. T. Bland *The mechanism of dimensional changes in the crystals of graphites and carbons under fast neutron irradiation* in *Philosophical Magazine*. 1966. p. 343- 356.
9. Price, R.J., *Strength of Irradiated graphite*, in *General atomic project 6400*, G.a. company, Editor. 1979, U.S department of energy: United State.
10. Kelly, B.T., *The structure and manufacture of nuclear grade graphite, Irradiation damege in graphite due to fast neutrons in fission and fussion systems*, IAEA, Editor. 2000: Austria.
11. Hall, G., et al. *Possibility for the microstructural modelling of the irradiation properties of graphites for future high temperature reactors*. in *3rd International Topical Meeting on High Temperature Reactor Technology*. 2006. Johannesburg, South Africa: Proceedings HTR2006.
12. Brocklehurst, J.E., Adam, R.W. , *Mechanical tests on graphite with simulated radiolytic oxidation gradients*, UKAEA, Editor. 1983: Warrington. p. 1-38.
13. Brocklehurst, J.E., *A method of simulating graphite property changes caused by radiolytic oxidation (for application to realistic tests on moderator bricks)*, UKAEA, Editor. 1980, Springfields Nuclear Power Development Laboratories: Preston. p. 1-21.
14. Berre, C., et al., *Numerical modelling of the effects of porosity changes on the mechanical properties of nuclear graphite.* Journal of Nuclear Materials, 2006. **352**(1-3): p. 1-5.
15. D.Buckthorpe, R.C., B. Van der Schaaf, B. Riou, H. Rantala, R. Moormann, F. Alonso, B-C. Friedrich, *Materials for High Temperature Reactor (HTR)*, in *16th Structural Mechanics in Reactor Technology (SMiRT 16)*. 2001, International & American Associations for Structural Mechanics in Reactor Technology Washington DC.
16. Pierson, H.O., *Handbook of Carbon, Graphite, Diamond and Fullerenes - Properties, Processing and Applications.* 1993: William Andrew Publishing/Noyes.
17. Francis, I.T., K.R. A Thoms, and A.F. A Rowcliffe, *Neutron irradiation experiments for fission and fusion reactor materials studies.* Journal of Neutron Research, 1994. **2**(2): p. 71- 83.
18. Marsden, B.J. *Graphite Technology Course*. 2002; Available from: http://pbadupws.nrc.gov/docs/ML0120/ML012080125.pdf.
19. Bernal, J.D., *The Structure of Graphite.* Proceedings of the Royal Society of London. Series A, Containing Papers of a Mathematical and Physical Character, 1924. **106**(740): p. 749-773.
20. Hall, G.N., *Microstructure modelling of Nuclear grade graphite*, in *MACE*. 2004, University of Manchester: Manchester. p. 352.

21. Bosak, A., et al., *Elasticity of single-crystalline graphite: Inelastic x-ray scattering study*. Physical Review B, 2007. **75**(15): p. 153408.
22. Kwiecinska, B. and H.I. Petersen, *Graphite, semi-graphite, natural coke, and natural char classification--ICCP system*. International Journal of Coal Geology, 2004. **57**(2): p. 99-116.
23. Reynolds, W.N., *Physical properties of graphite*. 1968, Amsterdam, New York Elsevier Pub. Co. .
24. Ebert, L.B., *Intercalation Compounds of Graphite*. Annual Review of Materials Science, 1976. **6**: p. 181-211.
25. Nightingale, R.E., *Nuclear graphite*. 1962, New York: Academic press.
26. Rand, S.J., *Significance of Tests for Petroleum Products (7th Edition): (MNL 1)*. 2003: ASTM International.
27. Robert, B., *NGNP Graphite Testing and Qualification Specimen Selection Strategy*. 2005. p. Medium: ED.
28. Ragan, S. and H. Marsh, *Review Science and technology of graphite manufacture*. J. Mat. Sc., (1983). **18**( ): p. 3161—3176.
29. Vreeling, J.A., O. Wouters, and J.G.v.d. Laan, *Graphite irradiation testing for HTR technology at the High Flux Reactor in Petten*. Journal of Nuclear Materials, 2008. **381**(1-2): p. 68-75.
30. Snead, L.L., T.D. Burchell, and Y. Katoh, *Swelling of nuclear graphite and high quality carbon fiber composite under very high irradiation temperature*. Journal of Nuclear Materials, 2008. **381**(1-2): p. 55-61.
31. Fazluddin, S., *Crack growth resistance in nuclear graphite*, in *School of Process, Environmental and Materials Engineering*. 2002, The University of Leeds: Leeds. p. 248.
32. Chi, S.-H., *Specimen size effects on the compressive strength and Weibull modulus of nuclear graphite of different coke particle size: IG-110 and NBG-18*. Journal of Nuclear Materials, (0).
33. Fedorchenko, B., I. I, Nenakhov, A. V, Beloivan, A. F., *Mechanical properties of composite materials based on polyfluoroethylene resin*. Strength of Materials, 1971. **3**(10): p. 1204- 1207.
34. Hall, G., B.J. Marsden, and S.L. Fok, *The microstructural modelling of nuclear grade graphite*. Journal of Nuclear Materials, 2006. **353**(1-2): p. 12-18.
35. Libin Sun, A.H., James Marrow, Alex SL Fok and Barry J Marsden, *AN EXPERIMENTAL STUDY ON THE POROSITY NETWORKS IN NUCLEAR GRAPHITE*, in *2nd International Topical Meeting on HIGH TEMPERATURE REACTOR TECHNOLOGY*. 2004: Beijing, CHINA.
36. Wen, K.Y., T.J. Marrow, and B.J. Marsden, *The microstructure of nuclear graphite binders*. Carbon, 2008. **46**(1): p. 62-71.
37. Zdravkov, B., et al., *Pore classification in the characterization of porous materials: A perspective*. Central European Journal of Chemistry, 2007. **5**(2): p. 385- 395.
38. J.F. Byrne, H.M., ed. *Porosity in Carbons*. first ed. Characterization and Applications, ed. W. Patrick. 1995, Halsted Press: London.
39. Neighbour, G.B., ed. *Management of ageing processes in graphite reactor cores*. 2007, The Royal Society of Chemistry: UK.
40. Tsang, D.K.L. and B.J. Marsden, *The development of a stress analysis code for nuclear graphite components in gas-cooled reactors*. Journal of Nuclear Materials, 2006. **350**(3): p. 208-220.
41. Sutton, A.L. and V.C. Howard, *The role of porosity in the accommodation of thermal expansion in graphite*. Journal of Nuclear Materials. **7**(1): p. 58-71.
42. Seldin, E.J., *Stress-strain properties of polycrystalline graphites in tension and compression at room temperature*. Carbon, 1966. **4**(2): p. 177-191.
43. Jenkins, G.M., *The stress-strain relationships of polycrystalline graphite under compression up to fracture*. Carbon, 1965. **3**(1): p. 93-94.
44. Jenkins, G.M., *Analysis of the stress-strain relationships in reactor grade graphite*. Br. J. Appl. Phys. 13 30.

45. Jenkins, G.M., *The effect of microporosity on the elastic modulus and yield curve of polycrystalline graphite.* Journal of Nuclear Materials, 1969. **29**(3): p. 322-328.
46. Spriggs, R.M., *Expression for Effect of Porosity on Elastic Modulus of Polycrystalline Refractory Materials, Particularly Aluminum Oxide.* Journal of the American Ceramic Society, 1961. **44**(12): p. 628-629.
47. Hasselman, D.P.H., *On the Porosity Dependence of the Elastic Moduli of Polycrystalline Refractory Materials.* Journal of the American Ceramic Society, 1962. **45**(9): p. 452-453.
48. Hashin, Z., *The Elastic Moduli of Heterogeneous Materials.* Journal of Applied Mechanics, 1962. **29**(1): p. 143-150.
49. Boey, S.Y. and D.J. Bacon, *Deformation of polycrystalline graphite under pressure.* Carbon, 1986. **24**(5): p. 557-564.
50. Brocklehurst, J.E., et al., *The effect of radiolytic oxidation on the physical properties of graphite.* J. Nucl. Mat., (1970). **35** p. 183—194.
51. Jenkins, G.M., *Fracture in reactor graphite.* Journal of Nuclear Materials, 1962. **5**(3): p. 280-286.
52. O. D, S., *Deformation Mechanisms in Polycrystalline Graphite.* Journal of the American Ceramic Society, 1967. **50**(10): p. 495.
53. Oku, T. and M. Eto, *The effect of compressive prestressing on the mechanical properties of some nuclear graphites.* Carbon, 1973. **11**(6): p. 639-647.
54. Paterson, M.S. and J.M. Edmond, *Deformation of graphite at high pressures.* Carbon, 1972. **10**(1): p. 29-34.
55. Kmetko, E.A., J.R. Morgan, and J.F. Andrew, *The compressibility of synthetic polycrystalline graphite and the effect of pore Structure accessibility.* Carbon, 1968. **6**(4): p. 571-572.
56. Yoda, S., I. Ioka, and M. Eto, *Deformation of graphites under hydrostatic states.* Journal of Nuclear Materials, 1984. **125**(1): p. 113-116.
57. Union Carbide, C., *The industrial graphite engineering handbook.* 1959, New York: Union Carbide.
58. Kelly, B.T., *Graphite--the most fascinating nuclear material.* Carbon, 1982. **20**(1): p. 3-11.
59. Narisawa, M., M. Adachi, and I. Souma, *High-temperature creep and resultant anisotropy in ultrasonic velocity in isotropic graphite.* Journal of Materials Science, 1994. **29**(3): p. 708-713.
60. Kelly, B.T., W.H. Martin, and P.T. Nettley, *Dimensional Changes in Polycrystalline Graphites under Fast-Neutron Irradiation.* Philosophical Transactions of the Royal Society of London. Series A, Mathematical and Physical Sciences, 1966. **260**(1109): p. 51-71.
61. Burchell, T.D. and L.L. Snead, *The effect of neutron irradiation damage on the properties of grade NBG-10 graphite.* Journal of Nuclear Materials, 2007. **371**(1-3): p. 18-27.
62. Marsden, B.J., S.-L. Fok, and H. Li, *Irradiation behaviour and structural analysis of HTR/VHTR graphite core component*, in *18th Internation Conference on Structural Mechanics in Reactor Technology (SMiRT 18)*. 2005, SMiRT: Beijing, China.
63. Gateau, *Measurement of the physical and mechanical properties of pressed Gilsocarbon graphite*, in *O.E.C.D. High temperature reactor project*, D.p. report, Editor. 1989: Paris.
64. Mason, I.B. and R.H. Knibbs, *The Young's modulus of carbon and graphite artefacts.* Carbon, 1967. **5**(5): p. 493-506.
65. Pickup, I.M., B. McEnaney, and R.G. Cooke, *Fracture processes in graphite and the effects of oxidation.* Carbon, 1986. **24**(5): p. 535-543.
66. Standring, J. and B.W. Ashton, *The effect of radiolytic oxidation by carbon dioxide on the porosity of graphite.* Carbon, 1965. **3**(2): p. 157-165.
67. Best, J.V., W.J. Stephen, and A.J. Wickham, *Radiolytic graphite oxidation.* Progress in Nuclear Energy, 1985. **16**(2): p. 127-178.
68. Kelly, B.T., et al., *The annealing of irradiation damage in graphite.* Journal of Nuclear Materials, 1966. **20**(2): p. 195-209.

69. Kelly, B.T., et al., *U.K.A.E.A. northern division studies of the radiolytic oxidation of graphite in carbon dioxide*. Carbon, 1983. **21**(4): p. 441-449.
70. Knudsen, F.P., *Dependence of Mechanical Strength of Brittle Polycrystalline Specimens on Porosity and Grain Size*. Journal of the American Ceramic Society, 1959. **42**(8): p. 376-387.
71. Engle, G.B., *Density and structural distributions in artificial graphites*. Carbon, 1970. **8**(4): p. 485-495.
72. Freise, E.J. and A. Kelly, *Twinning in Graphite*. Proceedings of the Royal Society of London. Series A, Mathematical and Physical Sciences, 1961. **264**(1317): p. 269-276.
73. Kuster, G. and M. Toksöz, *Velocity and attenuation of seismic waves in two phase media: Part II. Experimental results* GEOPHYSICS, 1974. **39**(5): p. 607-618.
74. Mavko, G., T. Mukerji, and J. Dvorkin, *The rock physics handbook: tools for seismic analysis in porous media*. 1998: Cambridge Univ. Press.
75. Hill, R., *The elastic behaviour of crystalline aggregate*. Proceedings of the Physical Society, 1952. **65**: p. 349.
76. Berryman, J.G., *Long-wavelength propagation in composite elastic media II. Ellipsoidal inclusions*. The Journal of the Acoustical Society of America, 1980a. **68**(6): p. 1809-1819.
77. Berryman, J.G., *Long-wavelength propagation in composite elastic media II. Ellipsoidal inclusions*. The Journal of the Acoustical Society of America, 1980b. **68**(6): p. 1820-1831.
78. Mavko, G., *Effective medium theories*, in *Effective medium models*, S.r.p. laboratory, Editor. 2009, Stanford university: California. p. 113-163.
79. Eto, M. and T. Oku, *Change in electrical resistivity of nuclear graphite during compression tests and a model for its deformation and fracture mechanism*. Journal of Nuclear Materials, 1974. **54**(2): p. 245-253.
80. Eto, M. and T. Oku, *The effect of pre-stressing and annealing on the young's modulus of some nuclear graphites*. Journal of Nuclear Materials, 1973. **46**(3): p. 315-323.
81. Yoda, S., M. Eto, and I. Ioka, *Effects of prehydrostatic loading on mechanical and physical properties of nuclear-grade graphites*. Journal of Nuclear Materials, 1984. **125**(1): p. 104-110.
82. Brocklehurst, J.E. and B.T. Kelly, *Analysis of the dimensional changes and structural changes in polycrystalline graphite under fast neutron irradiation*. Carbon, 1993. **31**(1): p. 155-178.
83. Pierre Ouagne, G.B.N., Brian McEnaney, *Influence of oxidation on toughness parameters for two nuclear grade graphites*. Journal of Physics D: Applied Physics, 2005. **38**: p. 1259-1264.
84. Fazluddin Shahed (2002) . PhD thesis, *Crack growth resistance in nuclear graphite*, in *Department of Materials*. 2002, University of Leeds: Leeds.
85. Svalbonas, V., T.C. Stilwell, and Z. Zudans, *Rules for design of nuclear graphite core components — Some considerations and approaches*. Nuclear Engineering and Design, 1978. **46**(2): p. 313-333.
86. P.Beghein, G.B., F.Hiltmann, M.Melin and B.du Mesnildot. *Nuclear Graphite NBG-17 and other solutions for the nuclear industry*. in *INGSM- 11*. 2010. Eastbourne, UK.
87. Cortie, M.B., *Calculation of Texture Volume Fractions by Integration and Gaussian Fitting*. Textures and Microstructures, 1997. **29**(3-4): p. 155-183.
88. L.Sun, et al. *An Experimental Study on The Porosity Networks In Nuclear Graphite*. in *Proceedings of the Conference on High Temperature Reactors*. 2004. Beijing, China: International Atomic Energy Agency.
89. Babout, L., et al., *The effect of thermal oxidation on polycrystalline graphite studied by X-ray tomography*. Carbon, 2005. **43**(4): p. 765-774.
90. John, C.R., *The Image Processing Handbook, Fifth Edition (Image Processing Handbook)*. 2006: CRC Press, Inc.
91. Kocks, U.F., C.N. Tomé, and H.R. Wenk, *Texture and Anisotropy: Preferred Orientations in Polycrystals and Their Effect on Materials Properties*. 2000: Cambridge University Press.
92. Bacon, G.E., *A method for determining the degree of orientation of graphite*. Journal of Applied Chemistry, 1956. **6**(11): p. 477-481.

93. Harold P. Klug, L.E.A., *X-Ray Diffraction Procedures: For Polycrystalline and Amorphous Materials*. 2nd ed. 1974, New York: J. Wiley.
94. Hammond, C., *The Basics of Crystallography and Diffraction*. 2001: Oxford University Press.
95. Bunge, H.J., *Texture analysis in materials science : mathemat. methods*. 1982, London u.a.: Butterworth.
96. Segmuller, A. and J. Angilello, *Automatic pole figure evaluation.* Journal of Applied Crystallography, 1969. **2**(2): p. 76-80.
97. Hielscher, R. and H. Schaeben, *A novel pole figure inversion method: specification of the MTEX algorithm.* Journal of Applied Crystallography, 2008. **41**(6): p. 1024-1037.
98. F. Bachmann, R.H., Helmut Schaeben, *Texture Analysis with MTEX- Free and open source software toolbox*. Solid state Phenomena, 2010. **160**: p. 63-68.
99. Krigbaum, W.R. and A.M.H. Vasek, *A Test of the Refinement Procedure for Determining the Crystallite Orientation Distribution: Polyethylene Terephthalate.* Texture, 1972. **1**(1): p. 9-16.
100. R.-J. Roe, W.R.K., *Description of crystallite orientation in polycrystalline material having fiber texture.* Journal of of Chemical Physics, 1964. **40**(9): p. 8.
101. R.-J. Roe, *Description of crystallite orientation in polycrystalline materials. III. General solution to pole figure inversion.* Journal of Applied Physics, 1965. **36**(6).
102. Matthies, S., G.W. Vinel, and K. Helming, *Standard distributions in texture analysis*. 1900, Berlin: Akademie-Verlag.
103. Keng, E.Y.H., *Air and Helium Pycnometer.* Powder Technology, 1969. **3**(3): p. 179-180.
104. Lowell, S., *Characterization of Porous Solids and Powders: Surface Area, Pore Size, and Density*. 2004: Kluwer Academic Publishers.
105. Ciftcioglu, M., D.M. Smith, and S.B. Ross, *Mercury porosimetry of ordered sphere compacts: Investigation of intrusion and extrusion pore size distributions.* Powder Technology, 1988. **55**(3): p. 193-205.
106. Dickinson, J.M. and J.W. Shore, *Observations concerning the determination of porosities in graphites.* Carbon, 1968. **6**(6): p. 937-941.
107. http://www.quantachrome.co.uk/en/Automatic_Pore_Size_Analyzers-Poremaster.asp.
108. Goodman, R.E., *Introduction to Rock Mechanics (2nd Edition)*, John Wiley & Sons.
109. Yoda, S., M. Eto, and T. Oku, *Change in dynamic young's modulus of nuclear-grade isotropic graphite during tensile and compressive stressing.* Journal of Nuclear Materials, 1983. **119**(2-3): p. 278-283.
110. Asmani, M., et al., *Influence of porosity on Young's modulus and Poisson's ratio in alumina ceramics.* Journal of the European Ceramic Society, 2001. **21**(8): p. 1081-1086.
111. Thrower, P.A., *The structure of reactor graphites and its relation to high temperature irradiation dimensional stability.* Carbon, 1971. **9**(3): p. 265-277.
112. Lokajicek, T., et al., *The determination of the elastic properties of an anisotropic polycrystalline graphite using neutron diffraction and ultrasonic measurements.* Carbon, 2011. **49**(4): p. 1374-1384.
113. James G, B., *Bounds and self-consistent estimates for elastic constants of random polycrystals with hexagonal, trigonal, and tetragonal symmetries.* Journal of the Mechanics and Physics of Solids, 2005. **53**(10): p. 2141-2173.
114. Williams, W.J., *Mercury porosimetry studies on PGA, AGL-mp and BAEL-GCMB Graphites.* 1976, Berkeley Nuclear Laboratories: Berkeley, Gloucestershire.
115. Vidal, J.M., Mays, T.J., *Mechanical properties and oxidation of nuclear graphites*. 1999, Department of Material Science and Engineering, University of Bath: Bath.
116. IAEA, *Characterization, treatment and conditioning of radioactive graphite from decommissioning of nuclear reactors*, in *Waste technology section*. 2006, IAEA: Vienna. p. 1-71.
117. Abrahamson, J., *The surface energies of graphite.* Carbon, 1973. **11**(4): p. 337-362.
118. Eto, M., T. Oku, and T. Konishi, *High temperature young's modulus of a fine-grained nuclear graphite oxidized or prestressed to various levels.* Carbon, 1991. **29**(1): p. 11-21.

119. Barsoum, M.W., et al., *Kink bands, nonlinear elasticity and nanoindentations in graphite.* Carbon, 2004. **42**(8–9): p. 1435-1445.
120. ChristopheBERRE, *Microstructural modelling of nuclear graphite using X-ray micro-tomography data*, in *School of Mechanical, Aerospace and Civil Engineering*. 2007, University of Manchester: Manchester. p. 223.
121. Pros, Z., et al., *Direct measurement of 3D elastic anisotropy on rocks from the Ivrea zone (Southern Alps, NW Italy).* Tectonophysics, 2003. **370**(1–4): p. 31-47.
122. Kern, H., et al., *The effect of oriented microcracks and crystallographic and shape preferred orientation on bulk elastic anisotropy of a foliated biotite gneiss from Outokumpu.* Tectonophysics, 2008. **457**(3–4): p. 143-149.
123. Blakslee, O.L., et al., *Elastic Constants of Compression‐Annealed Pyrolytic Graphite.* Journal of Applied Physics, 1970. **41**(8): p. 3373-3382.
124. Faulkner, D.R. and E.H. Rutter, *Comparisons of water and argon permeability in natural clay-bearing fault gouge under high pressure at 20°C.* Journal of Geophysical Research: Solid Earth, 2000. **105**(B7): p. 16415-16426.
125. Berryman, J.G., *Bounds and self-consistent estimates for elastic constants of random polycrystals with hexagonal, trigonal, and tetragonal symmetries.* Journal of the Mechanics and Physics of Solids, 2005. **53**(10): p. 2141-2173.
126. Den Toonder, J.M.J. and Toonder, *The relation between single crystal elasticity and the effective elastic behaviour of polycrystalline materials: theory, measurement and computation.* Modelling and Simulation in Materials Science and Engineering, 1999. **7**(6): p. 909.